



Universiteit
Leiden
The Netherlands

Electrocatalysis at Single Nanoparticles

Kleijn, S.E.F.

Citation

Kleijn, S. E. F. (2013, November 13). *Electrocatalysis at Single Nanoparticles*. Retrieved from <https://hdl.handle.net/1887/22192>

Version: Not Applicable (or Unknown)

License: [Leiden University Non-exclusive license](#)

Downloaded from: <https://hdl.handle.net/1887/22192>

Note: To cite this publication please use the final published version (if applicable).

Cover Page



Universiteit Leiden



The handle <http://hdl.handle.net/1887/22192> holds various files of this Leiden University dissertation

Author: Kleijn, Steven

Title: Electrocatalysis at single nanoparticles

Issue Date: 2013-11-13

Electrocatalysis at Single Nanoparticles

Proefschrift

ter verkrijging van
de graad van Doctor aan de Universiteit Leiden,
op gezag van Rector Magnificus Prof.mr. C.J.J.M. Stolker
volgens besluit van het College voor Promoties
te verdedigen op woensdag 13 november 2013
klokke 13:45

door

Steven Everard Filippus Kleijn

geboren te Amsterdam in 1985

Promotiecomissie:

Promotor: Prof. dr. M.T.M. Koper

Co-promotor: Dr. A.I. Yanson

overige leden: Prof. dr. J. Brouwer
Prof. dr. S.L. Lemay
Prof. dr. B.E. Nieuwenhuys
Prof. dr. T.J. Oosterkamp
Prof. dr. P.R. Unwin
Prof. dr. T. Wandlowski

Printed by Off-Page

Cover design by Erwin Kho – www.zerbamine.nl

ISBN: 978-94-6182-369-4

Table of Contents

1	Introduction	1
1.1	On Catalysis	1
1.2	From surface science to nanoparticle studies	3
1.3	Nanoparticles; the contents of this thesis	6
	Bibliography	9
2	Electrochemistry of Nanoparticles	11
2.1	Introduction	12
2.1.1	Important reactions	14
2.2	Preparation and characterization of nanoparticulate electrocatalysts	17
2.2.1	Single-step nanoparticle formation and immobilization	19
2.2.2	Immobilization of metal ions followed by reduction	20
2.2.3	Synthesis of metal nanoparticles followed by immobilization	21
2.2.4	Cleaning	24
2.2.5	Characterization	26
2.3	Model approaches to real catalysts	30
2.3.1	Influence of mass-transport	30
2.3.2	High throughput electrocatalyst screening	34
2.3.3	Stability of nanoparticulate catalysts	35
2.4	Electrochemistry at preferentially shaped nanoparticles	37
2.5	Measurements of individual metal nanoparticles	41
2.5.1	Techniques and Methods	42
2.5.2	Immobilized nanoparticle measurements	43
2.5.3	Nanoparticle landings	47
2.5.4	Measurements at the single nanoparticle-level within nanoparticle ensembles	54
2.6	Conclusions and Outlook	58
	Bibliography	60
3	Electrochemical characterization of nano-sized gold electrodes fabricated by nano-lithography	73
3.1	Introduction	74
3.2	Experimental	75
3.2.1	Chip Design	75
3.2.2	Fabrication	75
3.2.3	Materials	76
3.2.4	Electrochemistry	76
3.2.5	Numerical Calculations	77
3.3	Results	77
3.3.1	SEM	77
3.3.2	Blank Cyclic Voltammetry	78
3.3.3	Surface area determination	80
3.4	Conclusion	84

Bibliography	85
4 Influence of hydrazine-induced aggregation on the electrochemical detection of platinum nanoparticles	87
4.1 Introduction	88
4.2 Experimental	91
4.2.1 Materials	91
4.2.2 Lithographical fabrication of microelectrodes	91
4.2.3 Electrochemical Measurements	92
4.2.4 Nanoparticle Synthesis	92
4.3 Results	93
4.3.1 Influence of Hydrazine Concentration	102
4.4 Discussion	105
4.5 Conclusions	108
Bibliography	110
5 Landing and Catalytic Characterization of Individual Nanoparticles on Electrode Surfaces	113
5.1 Introduction	114
5.2 Experimental	116
5.2.1 Setup	116
5.2.2 Gold nanoparticle synthesis	117
5.3 Results	118
5.4 Conclusion	124
Bibliography	125
Appendix A: Fabrication protocol	127
Bibliography	132
Appendix B:	
Additional experiments for chapter 4	133
Summary	139
Samenvatting	143
List of publications	147
Curriculum Vitae	149

1

Introduction

1.1 On Catalysis

Catalysis is vital to life on earth, and has been applied by mankind for ages; the leavening of bread requires yeast, as does the fermentation of beer and wine. Medieval chemists, or alchemists, knew how to fabricate a considerable catalog of substances, but they almost always required significant heating; they were baffled by the mysterious *vis vitalis* of organisms that performed chemical conversions at room temperature. In the nineteenth century, it was found that enzymes aid in these chemical conversions and that they can perform their catalysis even outside of living cells.

The discovery of the enzymatic concept was preceded by the discovery of the phenomenon of catalysis¹, in the eighteenth century, when it was realized that otherwise stable gases reacted in the presence of specific metals. These experiments were performed by Joseph Priestley and later by Martinus van Marum, who reported the decomposition of ethanol vapours in the presence of various metals. The discovery of this phenomenon was quickly followed by its application, initially by sir Humphrey Davy as a lamp for English coal miners containing a platinum wire that would light up in the presence of flammable mine gas,[1] and later as the first lighter (a platinum catalyzed hydrogen flame) by Döbereiner.[2]

¹A wide range of substances, from enzymes, via soluble metal-organic complexes, to semiconductors are known to act as catalysts for chemical reactions. This thesis will however focus on the ability of pure metals to perform catalysis.

While the exact nature of these interactions was still poorly understood, the catalytic effect was already named in an early stage by Berzelius, who wrote a scientific review at the end of each year. He summarized the recent findings in catalytic experiments as follows: "It is, then, proved that several simple or compound bodies, soluble and insoluble, have the property of exercising on other bodies an action very different from chemical affinity. By means of this action they produce, in these bodies, decompositions of their elements and different recombinations of these same elements to which they remain indifferent." It was Berzelius who named this 'action' catalysis, but since he described it as a particular force (even using the term *vis occulta*) he did not contribute to the elucidation of the debate regarding the nature of the catalytic effect. Nevertheless, we still define a catalyst today as a substance that increases the rate of a chemical reaction, without being consumed in its process.

It follows from the above that catalytic research has always gone hand-in-hand with industrial application. At the present time, catalysis is an important industrial process that is employed from the conversion of crude oil into fuels to the detoxification of smoke-stack exhaust fumes. In fact, it is estimated that catalysts are used in 85-90% of the processes that generate bulk chemicals and materials.[3] Expressed in monetary terms, in 2012 the market for 'catalysis' alone is estimated at 20 billion dollars, a tiny amount considering its total output in the form of the petrochemical industry, which leans largely on catalyst enhanced productivity and weighs in at a staggering 2300 billion euros.[4] This implies that small gains in catalytic activity will lead to very large economic benefits. A subsection of the catalytic industry is electrochemical catalysis or electrocatalysis, in which case the catalyst increases the rate of a reaction that involves charge transfer. Electrocatalytic processes either supply electricity, or they require electricity for their functioning. Some electrocatalytic processes are operated on a very large industrial scale, such as the chlorine gas production, aluminium production and metal plating, and corrosion protection. In the production of chlorine gas (a very important bulk chemical) current is passed through two metal electrodes immersed in brine, yielding chlorine gas at the positive pole and hydrogen gas at the negative pole. The local production of chlorine gas by itself accounts for up to two percent of the Dutch electricity consumption.

Catalysts can be used to convert reactants into products, but they can also be used to convert fuels into energy more efficiently than conventional combustion. Recently, the potential to apply catalysts for energy uses has gained significant attention for several reasons. This is first of all due to rising fossil fuel prices, since catalytic conversion could make very efficient use of renewable hydrogen as a fuel. A second reason is

the increased demand for decentralized energy production as a balance to the recent increase in renewable energy, especially large fractions of which are solar and wind power that generate electricity intermittently.[5] Thirdly, increased use of hydrogen as a fuel would help abate the emission of carbon dioxide, which is recognized as a greenhouse gas. Catalytic fuel conversion could be combined with localized fuel generation providing large scale energy storage to reduce fluctuations in energy generation. An example of a catalytic fuel converter is the hydrogen fuel cell, which is the opposite of water electrolyzer cell. Two conductive poles are connected via an electronic circuit and a charge conducting electrolyte. Hydrogen is catalytically oxidized on one pole (the anode) sending protons through the membrane to the other pole (the cathode) where they recombine with the electrons transferred through the circuit in the oxygen reduction reaction (ORR). The electrons can do work in the circuit, meaning the fuel cell generates electricity.

The large-scale application of fuel cells is presently hindered by their cost, since expensive materials (at present mainly platinum) are necessary both for the catalysts performing the conversion of the fuel as well as for the sophisticated membranes that must conduct protons whilst remaining impenetrable to fuel. To reduce the amount of scarce metals in a fuel cell, their catalytic efficiency must be maximized. The major source of inefficiency is the oxygen reduction reaction at the fuel cell cathode. Over the last decades, research into increasing the efficiency of the catalyst by many groups worldwide has led to significant cost reduction.[6] To appreciate and discuss details on the state of the art of fuel cell catalysis, it is necessary to take a jump back in time.

1.2 From surface science to nanoparticle studies

Fundamental studies of the reactions that occur in fuel cells go back at least 200 years. The eminent Michael Faraday was working closely with Humphrey Davy and had reproduced the experiments of Döbereiner personally. In 1834, he reported that the catalytic reaction could only occur at the metal surface, since the (catalytic) oxidation of hydrogen on a Pt plate was greatly diminished by fouled surfaces,[7] however throughout the nineteenth century there was a debate on the exact nature of these catalytic interactions.[8] Irvin Langmuir, some 80 years later, expanded on the understanding of reactions at surfaces with more quantitative studies on the nature of adsorbing and dissociating gas molecules.[9] Studies on the nature of the interaction between molecules and metal surfaces benefited greatly from technological development, specifically the generation of ever higher vacuums and the controlled manufacture of single crystalline

metals of very high purity, polished to mono-atomically flat surfaces. These developments enabled very clean, model measurements, performed using a variety of probe techniques.[10]

It was found from these studies that catalytic reactions are highly sensitive to the local arrangement of metal atoms in the surface. A metal surface is a truncation of an infinite crystalline lattice, and the orientation of the plane intersecting that lattice determines the two-dimensional arrangement of the atoms in the surface. A crystal that is cut on all sides is shown in Figure 1.1, revealing the different atomic configurations. Upon cleaving the lattice, the atoms in the surface lose the electronic interaction with the layer previously above them, changing the local electronic properties of the surface atoms. With respect to the bulk structure, the atoms in the surface become under-coordinated. The coordination of the metal atoms is further reduced, when the amount of neighbouring atoms in the plane goes down, the degree of which is dependent on the truncation plane of the crystal. The possible planes of truncation are indicated by the so-called Miller index notation (hkl), and are orthogonal to the vector on the axes of the lattice element (the unit cell, that is propagated infinitely in three dimensions to form the crystal) indicated by the Miller index numbers. For the face-centered cubic crystal structure of most metals, three elementary truncations form the basal planes and these are referred to as (111), (110) and (100) surfaces. The (111) surface is the most stable surface with the highest coordination, while the (110) surface has the lowest coordination.[11] When the crystal is truncated at an angle that does not perfectly correspond to a basal plane, a staircase-like surface is revealed that follows the angle of the cut. Such surfaces thus include steps – which separate longer terraces in a basal plane orientation – that are also under-coordinated.

These single crystal surfaces started to be applied to electrochemical measurements as well, with important work done by Clavilier.[12, 13] Surface sensitivity in electrocatalytic reactions was also revealed, with very clear dependence on the surface structure for the oxidation of carbon monoxide on Pt electrodes.[14] It was found that Pt (111) surfaces have the lowest activity for the CO oxidation, and that the introduction of steps leads to a significant increase in the reactivity. The steps can have either a (110) or a (100) orientation, and both step sites are more active than the (111) plane for the CO oxidation.[15] It was suggested that the oxygen species required for CO oxidation adsorbs preferably at the step sites and that the reaction between CO molecules and oxygen atoms occurs only there.[16]

The model studies that followed from the work of Faraday and Langmuir have resulted in a tremendous increase in insight. They were however always complimented

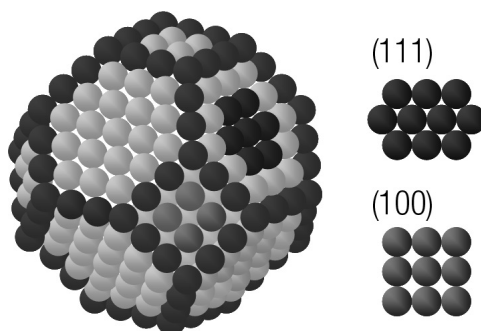


Figure 1.1: A cubo-octahedral nanoparticle; the triangular and diamond faces are the (111) and (100) orientation respectively, while the edges are highlighted for clarity.

by applied catalytic studies in which libraries of materials were screened for catalytic activity. Such techniques have been very successful in industrial practice, and it was in this way that the catalyst for ammonium synthesis in the famous Haber-Bosch process was developed. Industrial catalysts are prepared with a very high surface area to weight ratio, in order to reduce the cost incurred by metallic ‘dead weight’, especially relevant when considering the scarcity of some of the metals used in applied catalysis. The increase in surface area is achieved by using fine metal particles that are called nanoparticles when they reach a diameter smaller than 100 nm. Presently, the fields of model surface science-type measurements and catalytic screening measurements are converging as model surface reactions are being analyzed under reaction conditions[17, 18] and nanoparticle ensembles can be followed using in-situ techniques[19] and high resolution electron microscopy.[20]

It has been observed that the catalytic activity of nanoparticles is related to their size and shape, which is attributed to the change in atomic configuration of a nanoparticle of ever-decreasing size.[14] A nanoparticle is in its most stable shape when the contribution of low energy basal planes (the (111) and (100) planes in the case of Pt) to the surface is maximized. Therefore, particles tend to take a cubo-octahedral shape of which the fractions of (100), (111) as well as edge sites can be calculated for any NP radius, as shown in Figure 1.1.[21] In this way, results obtained on single crystal model surfaces can be correlated with those obtained for nanoparticles of increasing radius. For the CO oxidation reaction one would expect, from the behaviour observed on single-crystal electrodes, an increase in activity for smaller particles containing a large fraction of edge sites. On the contrary it was found that small particles have a lower activity for the CO oxidation than large particles.[22] As particles increase, the basal planes start to show defects and these sites have been suggested to be most

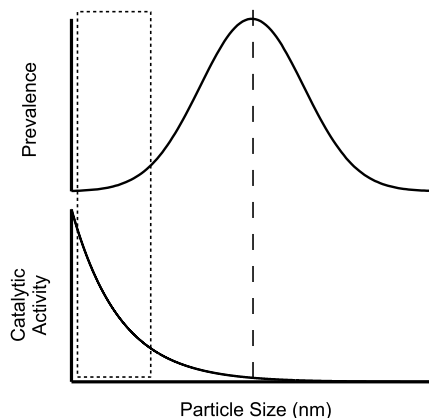


Figure 1.2: Schematic; when the catalytic activity of nanoparticles does not depend linearly on their size, no accurate size dependence can be obtained from ensemble measurements using the mean NP size.

active.[23] This indicates that the nature of particle edges and step sites on extended surfaces is quite different.

1.3 Nanoparticles; the contents of this thesis

The particle size effect for the CO oxidation has been found by studying large ensembles of NPs, placed on planar electrodes or porous carbon supports. The catalytic activity measured in this way is related to the average particle size obtained through e.g. transmission electron microscopy (TEM) measurement of a NP sample. The NP size is usually distributed normally around a mean value, which is taken as the average size when reporting the catalytic measurements. Nevertheless, as indicated in Figure 1.2, the NPs at the ends of the distribution may have very much altered reactivity, certainly in reactions that have a non-linear dependence on the particle size, as has been reported for the CO oxidation. Moreover, since not all particles of equal size must also have an equal shape, the translation between activity and size may not be so straightforward. It is therefore interesting to specifically study the activity of individual particles, preferably if they have well-defined shapes and sizes.

An additional topic related to the study of applied fuel cell catalysts, is the influence of the interaction between particles on the catalytic activity. Since NPs consume reactant from the electrolyte around them, they locally induce a concentration gradient that extends a certain length into the electrolyte. The typical distance influenced by

the concentration gradient is called the diffusion length, and it may be large enough to perturb mass transport towards an adjacent particle, thereby reducing the flux of reactant arriving at two interacting nanoparticles. The study of individual particles and well controlled ensembles of nanoparticles has received a considerable amount of reports in the very recent literature, to be discussed in greater detail in the second chapter of this thesis.

Experimental results obtained for the study of individual nanoparticles and the interaction between discrete amounts of particles are also included in this thesis. These are separated in two distinct methods of studying single catalyst NPs, as depicted in Figure 1.3. One way to monitor the signal from a single particle is to create a very tiny 'landing platform' of an electrode, which has as its only function to conduct electrons to or from the catalyst particle, without generating a large signal of its own. This means that such an electrode must be small enough to prevent the generation of significant current and the material that it is made out of should be catalytically inert, that is, unable to catalyze the same reaction as the catalyst particle under study. The maximum size of the electrode is determined by its background current, and is on the micrometer scale.

Reaching such electrode surface areas using conventional mechanical electrode preparation is increasingly difficult; therefore the microscopic electrodes used in this thesis are fabricated using (nano-)lithography. The characterization of lithographically fabricated electrodes is discussed in chapter 3, while details of the fabrication process can be found in appendix A. In this chapter it is shown that by using lithographical fabrication, very small nanoelectrodes can be made reproducibly and that they can be reliably characterized using both electrochemical measurements and scanning electron microscopy. After a confined area is successfully designated to be used for electrocatalytic measurement, NPs should be immobilized on the electrode surface. A very controlled way of depositing NPs on an electrode surface is to inject NPs into the electrolyte and monitoring electrochemical signal due to their arrival at the electrode. For example, one can observe the step-wise extinction of a redox current running at an electrode being covered by the cumulative landing of insulating particles.[24] A particularly powerful way of detecting the arrival of catalyst particles is through their electrocatalytic conversion of a substrate in solution that is not converted at the support electrode. This method was pioneered in the research group of A.J. Bard, by showing the detection of individual Pt NPs on a carbon ultramicroelectrode (UME) that was held at the potential of the hydrogen evolution reaction on Pt. Consequently, a step-wise increase in the cathodic current was observed at the electrode.[25] In chapter 4 a sim-

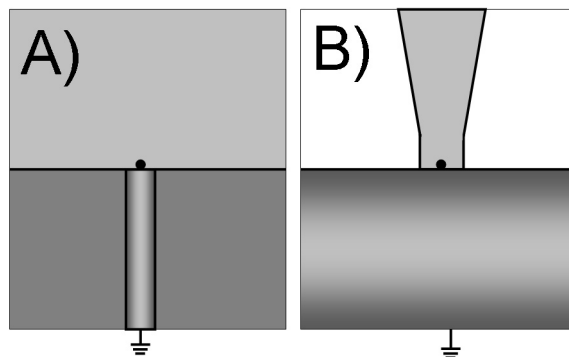


Figure 1.3: Two ways to study the activity of a single catalyst particle electrochemically: A) using a small electrode submerged in a quasi-infinite volume of electrolyte or, B) a quasi-infinite planar electrode with a confining electrolyte.

ilar experiment is used to detect the arrival of individual Pt NPs at a lithographically fabricated Au UME. We discuss in this chapter the necessity for careful characterization of the electrode after detecting the arrival of NPs. Specifically, complications for this detection mechanism regarding the aggregation of Pt NPs in solution by the electrocatalytic substrate are discussed.

An alternative manner to measure an individual catalyst particle on a very small electrode area is to confine the amount of electrolyte in contact with its surface, as shown in panel B) of figure 1.3. Such conditions are met if a very tiny electrolyte droplet is placed onto a surface. When an electrolyte-filled pipet with a very narrow taper (so that its tip is one micron across or smaller) contacts an electrode surface with the meniscus formed at its end, the electrolyte boundaries on the surface are microscopic. Reference electrodes can then be introduced inside the pipet so that electrochemical measurements can be performed against (a section of) the electrode. Using pipette tips contacting TEM substrates allowed the characterization of individual particles both electrochemically and microscopically as shown in chapter 5. Importantly, cyclic voltammograms measured at a single Au NP, which was also analyzed using TEM, are reported.

Bibliography

- [1] Davy, H. *Philos. Trans. R. Soc. Lond.* 1817, 107, 77–85.
- [2] Kauffman, G. B. *Platinum Met. Rev.* 1999, 43(3), 122.
- [3] Chorkendorff, I.; Niemantsverdriet, J. *Concepts of Modern Catalysis and Kinetics*; Wiley-VCH: Weinheim, 2003.
- [4] CEFIC, T. E. C. I. C. Facts and figures 2011, the european chemical industry in a worldwide perspective Technical report, CEFIC, The European Chemical Industry Council, 2011.
- [5] EWEA. Wind in power: 2012 european statistics Technical report, EWEA, 2013.
- [6] Debe, M. K. *Nature* 2012, 486(7401), 43–51.
- [7] Faraday, M. *Philos. Trans. R. Soc. Lond.* 1834, 124, 55–76.
- [8] Robertson, A. *Platinum Met. Rev.* 1975, 19(2), 64.
- [9] Langmuir, I. *J. Am. Chem. Soc.* 1915, 37(5), 1139–1167.
- [10] Somorjai, G. A. *J. Phys. Chem. B* 2002, 106(36), 9201–9213.
- [11] Kittel, C. *Introduction to solid state physics*; John Wiley and Sons: Hoboken, 8 ed., 2004.
- [12] Clavilier, J.; Faure, R.; Guinet, G.; Durand, R. *J. Electroanal. Chem. Interfac. Electrochem.* 1979, 107(1), 205–209.
- [13] Lipkowski, J.; Ross, P. *Electrocatalysis*; Wiley-VCH: New York, 1998.
- [14] Koper, M. T. M. *Nanoscale* 2011, 3(5), 2054–2073.
- [15] Vidal-Iglesias, F. J.; Solla-Gullón, J.; Campiña, J. M.; Herrero, E.; Aldaz, A.; Feliu, J. M. *Electrochim. Acta* 2009, 54(19), 4459–4466.
- [16] Lebedeva, N. P.; Koper, M. T. M.; Herrero, E.; Feliu, J. M.; van Santen, R. A. *J. Electroanal. Chem.* 2000, 487(1), 37–44.
- [17] Yanson, Y.; Frenken, J. W. M.; Rost, M. J. *Phys. Chem. Chem. Phys.* 2012, 13(35), 16095–16103.
- [18] Hendriksen, B. L. M.; Ackermann, M. D.; van Rijn, R.; Stoltz, D.; Popa, I.; Balmes, O.; Resta, A.; Wermeille, D.; Felici, R.; Ferrer, S.; Frenken, J. W. M. *Nat Chem* 2010, 2(9), 730–734.
- [19] Buurmans, I. L. C.; Ruiz-Martínez, J.; Knowles, W. V.; van der Beek, D.; Bergwerff, J. A.; Vogt, E. T. C.; Weckhuysen, B. M. *Nat Chem* 2011, 3(11), 862–867.
- [20] Kisielowski, C.; Ramasse, Q. M.; Hansen, L. P.; Brorson, M.; Carlsson, A.; Molenbroek, A. M.; Topsøe, H.; Helveg, S. *Angewandte Chemie International Edition* 2010, 49(15), 2708–2710.
- [21] Van Hardeveld, R.; Hartog, F. *Surf. Sci.* 1969, 15(2), 189–230.
- [22] Maillard, F.; Pronkin, S.; Savinova, E. *Fuel Cell Catalysis: A Surface Science Approach, e.d M.T.M.Koper*; Wiley: Hoboken, 2009.
- [23] Arenz, M.; Mayrhofer, K. J. J.; Stamenkovic, V.; Blizanac, B. B.; Tomoyuki, T.; Ross, P. N.; Markovic, N. M. *J. Am. Chem. Soc.* 2005, 127(18), 6819–6829.
- [24] Quinn, B. M.; van 't Ho, P. G.; Lemay, S. G. *J. Am. Chem. Soc.* 2004, 126(27), 8360–8361.
- [25] Xiao, X.; Bard, A. J. *J. Am. Chem. Soc.* 2007, 129(31), 9610.

2

Electrochemistry of Nanoparticles

Metal nanoparticles (NPs) find widespread application as a result of their unique physical and chemical properties. Among many applications, NPs have generated considerable interest in catalysis and electrocatalysis, where they provide a high surface area to mass ratio, and can be tailored to promote particular reaction pathways. The activity of NPs can be analyzed especially well using electrochemistry, which probes interfacial chemistry directly. In this review, we discuss key issues related to the electrochemistry of NPs. We highlight model studies that demonstrate exceptional control of NP shape and size, or mass transport conditions, that can provide key insights into the behavior of ensembles of NPs. Particular focus is on the challenge of ultimately measuring reactions at individual NPs, and relating the response to NP structure, which is leading to imaginative experiments that impact electrochemistry generally as well as broader surface and colloid science.

2.1 Introduction

Metal nanoparticles (NPs) have received a great deal of attention owing to their fascinating physical and chemical properties which can differ significantly from those of the bulk material. Interesting aspects of NPs include size- and shape-dependent interatomic bond distances,[1, 2] melting points,[1, 3] chemical reactivity,[4–6] and optical and electronic properties.[1, 7, 8] Furthermore, the small size of NPs has allowed nanoscale electrochemical processes to be probed, such as electric double layer effects on interfacial electron transfer reactions.[9–12] NPs find many technical applications, such as in catalysis,[5, 13, 14] sensors,[15–17] and spectroscopy (such as surface enhanced Raman spectroscopy),[17–19] as optical filters,[20] and in biomedical applications.[21–23]

Based on the application in hand, NPs are selected to achieve a particular function, from properties that emerge from both the constituent materials of the NP and its size. Significant research effort has thus aimed for a definitive understanding of shape and size effects on NP properties. In this context, electrochemical techniques are especially interesting, particularly when electrochemical characteristics can be related directly to other properties of the NP. The challenge of ultimately measuring the electrochemical behavior of individual NPs is leading to imaginative experiments that impact electrochemistry generally, as well as broader surface and colloid science, as we highlight in this chapter.

One of the largest applications of NPs is in electrocatalysis, the field of catalysis concerned with reactions that involve charge transfer at the interface between a solid catalyst and an electrolyte.[13] This area is key to the development of fuel cells and batteries, electrolyzers and electrosynthetic methods, as well as electrochemical sensing systems. The commercial viability of such devices requires the optimization of catalyst materials, not only to promote efficient use, but also to enhance selectivity towards a particular pathway.

The reduction of particle size to decrease catalyst cost and improve usage does not necessarily lead to an optimal catalytic performance, as catalytic activity does not always scale linearly with the NP surface area. Ultrasmall NPs may become non-metal-like[24] and be more prone to poisoning,[25] and reaction pathways may depend strongly on NP size.[26] This is because the interaction energies between reactant molecules and metal surface atoms depend strongly on the local arrangement of the metal atoms in the surface, as evident in model (single-crystal) experiments[5, 27] and computational studies.[28] Moreover, the mass transport rates of reactants, products and

intermediates depend significantly on NP size and coverage on an electrode support. This makes the investigation of NP electrochemistry and electrocatalysis non-trivial, and, without proper controls may lead to ambiguities when comparing data from different types of experiments, as we discuss herein (Section 2.3).

In fuel cell applications, metal NP catalysts are supported on conductive carbon substrates and employed in membrane-electrode assemblies (MEAs; Fig 2.1a). These real catalysts have been studied in model environments to evaluate their performance as a function of composition (Fig 2.1b).[29] However, fuel cell assemblies are complicated systems suffering from e.g. fuel crossover across the membrane, non-electrochemical contributions to the cell-voltage and an unknown and variable catalyst utilization factor.[30] Since these measurements leave the performance of individual NPs poorly understood, they are often complemented with studies on model catalysts. Model catalysts have tended to consist either of well-defined macroscopic metal electrodes, or well-characterized dispersions of metal NPs on catalytically inert electrodes. However, there are several recent developments that have allowed the focus of the research to shift towards the study of individual NPs (Fig 2.1c), and such approaches may ultimately provide the missing link between macroscopic electrodes and NP assemblies via single NP activity measurements, as we highlight in this chapter.

The use of NPs or nanoscale electrodes (NSEs) in electrochemistry has been the subject of various recent reviews, focusing on electroanalysis,[15] NSEs and nanopores, [31–33] or NP synthesis.[34, 35] In this chapter, we focus primarily on electrocatalysis at the level of individual NPs, assessing recently developed methodology, including: advances in NP synthesis that allows the rational design of shape-controlled (faceted) NPs; novel electrochemical scanning probe methodologies that allow the study of single NPs; and recent developments in single NP detection. To put these and other studies into perspective we discuss and advocate procedures for reproducible and meaningful experiments. Thus, we identify best practice in both highly defined nanoparticulate electrocatalysis and single NP electrochemistry.

The structure of this review is as follows. First, we briefly outline a number of important and commonly studied reactions in electrocatalysis that are referred to throughout the review, highlighting the present status and outstanding issues. We then discuss common NP synthesis methods and protocols for setting up reproducible measurements of electrocatalysis. This is followed by an assessment of recent results from electrocatalytic measurements on ensembles of NPs where there is a high degree of control over particle shape or mass-transport conditions. These model studies in many ways represent the recently established start-of-the-art. Finally, we give detailed

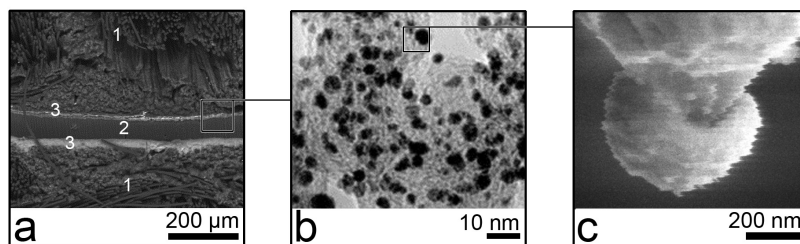


Figure 2.1: Different measurements on electrocatalysts: (a) a real catalyst in application environment,[36] as revealed by a cross section of a complete membrane-electrode assembly (fibrous carbon cloth gas-diffusion layers (1) sandwich a membrane (2) that has both anode and cathode catalyst layers (3) deposited on its sides, appearing as bright gray) (©2004, Elsevier); (b) a commercial Pt on C catalyst as used in studies of model environments.[37] (©2005, Elsevier) (c) an individual, model Pt NP in a model environment. [38] (©2003, American Chemical Society)

attention to emerging frontier techniques that are able to target single NPs, and in the best cases relate structure and activity at a single NP. The chapter concludes by summarizing the main issues and by providing an outlook for the further development of this important field.

2.1.1 Important reactions

Fuel cell reactions are among the most studied electrocatalytic reactions, and we will frequently make reference to them. It is thus useful to give some background on selected reactions, to indicate critical issues involved in respect of electrocatalysis, and the relationship of activity to NP properties.

Oxygen reduction reaction (ORR)

The electroreduction of oxygen is critical to the efficiency of (hydrogen) fuel cells[39] and metal-air batteries.[40, 41] The thermodynamic equilibrium potential for the ORR is 1.23 V versus the reversible hydrogen electrode (RHE), but even on the most active catalyst materials (Pt group metals) significant current is only measured at potentials less than 0.9 V.[42] Recent theoretical studies have provided new insights into the origins of the slow ORR kinetics;[28, 43] the binding energy of the several oxygen-containing intermediates with the electrode surface is key, and platinum surfaces appear to provide interaction energies close to the theoretical optimum.

The full reduction of oxygen to water entails the transfer of four electrons in steps that are depicted schematically in Figure 2.2. The present view is that the predom-

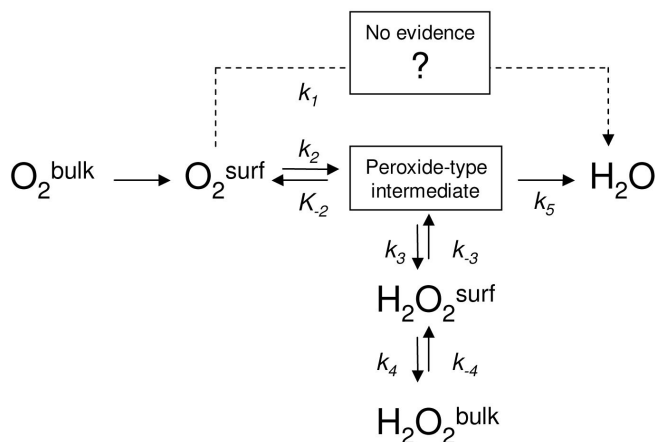


Figure 2.2: A proposed mechanism for the oxygen reduction reaction (ORR).

ant mechanism involves an adsorbed hydrogen peroxide-type intermediate that may convert to and desorb as H_2O_2 , before undergoing further reduction. This reduces the effective cathodic current, contaminates the surroundings of the catalyst, and corrodes the polymer membrane present in fuel cells; the formation of hydrogen peroxide is therefore triply undesired. Because on Pt surfaces the oxygen-oxygen bond can be broken, with relatively little interference of the formation of an irreversible oxide, Pt is the best monometallic electrode material for the ORR. In contrast, on very noble metals such as Au, the ORR does not proceed appreciably beyond the reduction to hydrogen peroxide. Transition metals, on the other hand, are prone to form stable oxides, leaving the dissociated oxygen immobilized.[43]

The structure sensitivity of the ORR on Pt has been investigated through the use of single-crystal electrodes. In sulfuric and phosphoric acid solutions, the structural sensitivity of the ORR mirrors the relative adsorption strength of the electrolyte anions, which adsorb strongest on the (111) surface that concomitantly shows the lowest ORR activity.[44] In perchloric acid solutions, anion adsorption does not occur, and the ORR activity is significantly increased.[44] A detailed study of single crystals with varying terrace length has shown that ORR activity increases with increasing step density (i.e. decreasing terrace width), with infinite (111) terraces having the lowest activity,[45] but the absolute difference in activity between different crystal structures is much less pronounced than in sulfuric acid. Although studies of this type provide valuable fundamental information, the projection of these findings to predict NP shape and size

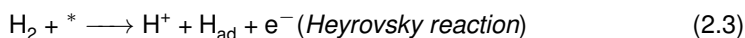
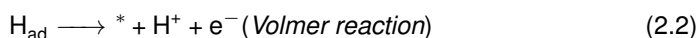
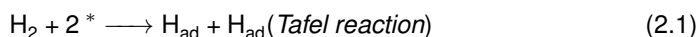
effects in the ORR is not straightforward.

In terms of NP studies, a prevalent view has been that the ORR activity decreases with decreasing NP size,[5, 30] which has been rationalized by the suggestion that the main contribution to the ORR comes from the fraction of extended terraces on NPs, which is increased at larger NPs.[46] However, this view opposes the experimental findings on single crystals outlined above,[45] highlighting the difficulty of translating information between NP studies and macroscale measurements for the ORR. Watanabe et al. have argued that apparent NP size effects on ORR activity can be impacted by experimental design, and, particularly, diminished mass-transport to individual NPs in an ensemble as the particle loading increases.[47] With high NP loadings on a support, recent findings indicate that hydrogen peroxide generated at the NP may re-adsorb on neighboring NPs in close proximity and thereby improve the overall ORR yield.[48]

The influence of both NP size and diffusion effects on the ORR are an important topic of debate, and we will discuss herein recent efforts to study this reaction at individual NPs (Section 2.5), as well as at NP ensembles under conditions of well-controlled mass transport (Section 2.3).

Hydrogen evolution reaction / hydrogen oxidation reaction

The hydrogen oxidation reaction (HOR) is the fuel consuming reaction in fuel cells and the hydrogen evolution reaction (HER) is the cathodic reaction in electrolyzers used to produce hydrogen. Both reactions are characterized by extremely fast kinetics on platinum electrodes[49] and almost perfect reversibility (particularly compared to the complete lack of reversibility of the oxygen reduction and evolution reaction). While the best catalyst for both reactions, Pt, has been known for centuries, materials research to improve HER/HOR focuses on reducing or removing altogether the Pt content, or on modifying Pt to increase resilience towards carbon monoxide,[50–52] a common feedstock contaminant in H₂ produced by steam reforming of hydrocarbons, that is used for fuel cells. The following steps describe the HOR:[30]



where * indicates a vacant site at the catalyst surface. Definitive determinations of the mechanism and NP size dependence have remained elusive due to the complica-

tions posed by the fast kinetics of the HOR.

The counterpart HER reaction is not hindered by mass-transport in the high-proton concentrations of acidic electrolytes relevant for electrolyzers. On the macroscale, the Pt (110) surface is the most active,[44] while HER activity has been observed to increase with decreasing particle size,[53, 54] as discussed in more detail in Section 2.5.1. On Pt, it is well established that the HER follows a Volmer-Tafel mechanism.[30]

Hydrazine oxidation

Hydrazine (N_2H_4) is a potent fuel that can be oxidized to form molecular nitrogen and water in a four-electron reaction. The reaction proceeds very rapidly via successive deprotonation steps that leave the N-N bond intact.[55, 56] On Au there is an overpotential of almost 500 mV with respect to Pt,[56] but for both metals, once the onset potential is reached, a mass-transport limited situation is readily established with further increasing potential. Carbon electrode materials are essentially completely inactive towards hydrazine oxidation. Due to this strong dependence of the onset potential on the type of electrode material, as well as the fast reaction kinetics, hydrazine oxidation has proven very suitable to distinguish between different electrode materials, making it a good redox probe for NP collision experiments that are discussed in Section 2.5.2.

2.2 Preparation and characterization of nanoparticulate electrocatalysts

A key aspect to the study and employment of NPs as electrocatalysts is the preparation and characterization of nanoparticulate electrodes, which often consists of NPs dispersed on a (typically non-electrocatalytic) support material. In such electrodes, the NP support plays a number of roles. First and foremost, from a practical point of view, the support electrode acts as a conductive bridge, contacting the NPs to an external electronic circuit. Second, the support acts to disperse the NPs, to limit agglomeration and maintain the high surface-to-volume ratio desired. Finally, the interaction between the support material and the NPs can be employed to modify the electrocatalytic activity of the NPs.[57] For example, Hayden et al. showed that titania-supported Au NPs have higher activity for the electrochemical oxidation of CO than carbon-supported Au NPs,[57] while titania-supported Pt NPs are less active for CO oxidation[58] and oxygen reduction[59] than carbon-supported Pt NPs. Although the occurrence of such support effects is well-known in gas-phase heterogeneous

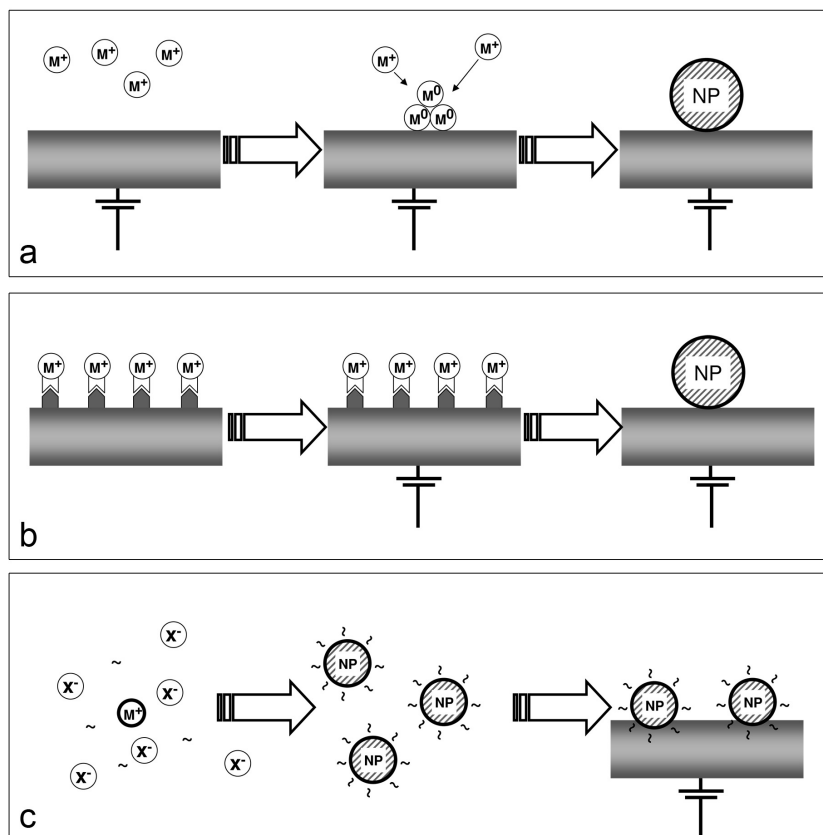


Figure 2.3: Three general approaches to fabricate a nanoparticulate electrode: (a) simultaneous NP formation and immobilization; (b) immobilization of metal ions followed by reduction; (c) synthesis of metal NPs followed by their immobilization.

catalysis,[60–63] the interplay between the support material and NP activity is significantly less understood in electrocatalysis.

The most common support materials are various types of carbon[64–68] as the electrodes used in fuel cells are typically carbon-based. In addition, carbon is cheap and relatively inert towards many electrocatalytic (bond-breaking and bond-making) processes. For fundamental studies, gold has found considerable use as it can be cleaned and characterized easily, and provides a stable surface.[69, 70] Titania has also received attention as a model in studies of support effects,[57, 59] while doped tin oxides are typically employed as support materials for applications where optically transparent electrodes are desirable.[71–73]

While there are numerous methods to prepare and immobilize NPs on conductive

supports, they broadly fall into three categories (Figure 2.3): a) simultaneous (single-step) NP formation and immobilization; b) immobilization of metal ions followed by their reduction to metal NPs; c) synthesis of metal NPs followed by their immobilization on the surface of the support electrode.

2.2.1 Single-step nanoparticle formation and immobilization

In this approach, the formation and immobilization of NPs on a support electrode takes place simultaneously in a single-step. Examples of this approach are: the electrodeposition of NPs from a solution containing the metal ion, either onto the bare support electrode,[74–82] or onto the support electrode modified with a polymer film;[78, 83–86] electroless deposition;[77, 87, 88] and vacuum evaporation.[89–93] Electrodeposition is by far the most popular of these methods, as it makes use of electrochemical equipment, ensures an electrical contact between the NP and substrate and provides many tunable parameters, such as the deposition potential or current, time, temperature and electrolyte composition,[74, 75, 94] to adjust the size-, shape- and spatial distribution of the electrodeposited NPs. The coupling of electrodeposition experiments with other characterization techniques, such as *ex situ*[95–97] and *in situ* TEM,[98, 99] and small-angle X-ray scattering (SAXS)[100] has provided valuable insights into the early stage of NP formation which may ultimately lead to improved electrodeposition protocols.

The main drawback of electrodeposition at present is that it typically leads to NP deposits with a wide size distribution,[74] for three reasons. First, new NP nuclei (small clusters of atoms) may form during the entire duration of the electrodeposition process (progressive nucleation).[74, 76] This leads to a wide distribution in growth times for individual NPs, and, consequently, in NP sizes. Second, during growth, depletion layers of neighboring NPs can start to overlap, causing these NPs to grow more slowly compared to those which are diffusionally isolated.[101] Consequently, the size of a single NP correlates with the local number density of NPs. As the number of nearby NPs will vary from one NP to the next in a random ensemble, this leads to a broadening of the size distribution during NP growth.[101] Third, (surface mediated) Ostwald ripening can occur, whereby large NPs grow at the expense the small NPs due the size-dependence of the free energy of stabilization of a NP.[102, 103]

To circumvent the size dispersion due to the progressive formation of new nuclei, efforts have been made to separate in time the formation of nuclei, and the growth of those nuclei. This control is typically achieved by forming nuclei with a short (< 10 ms) potential pulse at high overpotential with respect to the reduction potential

of the metal ions in solution, followed by a long growth pulse (up to minutes) at low overpotential, where no new nuclei are formed and all growth occurs on pre-formed nuclei.[71, 74, 75, 77, 104–109] Slow NP growth at low overpotential also diminishes concentration polarization near the substrate, so that local NP coverage has less effect on the extent of growth of individual NPs. This double potential pulse approach has been successfully employed to electrodeposit reasonably monodisperse NP arrays of various metals.[71, 74, 75, 77, 104–109]

An alternative method to minimize depletion effects is to incorporate a local source of convection within the depletion layer. An easy way to achieve this is to drive a gas-evolving reaction (in practice through the co-evolution of hydrogen from protons), in parallel with the electrodeposition reaction, so that the formation and release of gas bubbles drives convective mixing near the growing NP.[110, 111] While H₂ co-evolution leads to the size distribution narrowing,[110] the resulting NPs are typically nanocrystalline and fractal in nature.[110, 111] Finally, the deposition of NPs in a periodic array, ensures that mass transport to each NP is similar.[112] However, this method is rarely employed, as it involves extensive pretreatment of the substrate electrode to create a periodic array of nucleation sites.

2.2.2 Immobilization of metal ions followed by reduction

In this two-step procedure, metal ions are immobilized on the electrode surface before being reduced (either chemically or electrochemically) to form NPs directly attached to the surface. The spatial distribution and average size of the resulting NPs are determined by the amount of metal precursor, which can be controlled by adjusting the density of metal ion immobilization sites. By limiting the amount of immobilized ions, the preparation of small NPs is facilitated.

A key challenge of this approach is the controlled introduction of functional groups that coordinate to the desired metal precursor on the electrode surface. One option is to immobilize ions within a polyelectrolyte film deposited onto the substrate electrode,[113–118] leading to the encapsulation of NPs within the polyelectrolyte film. While this encapsulation provides a steric barrier to particle agglomeration, the resulting NPs may be less catalytically active than bare NPs.[113] An alternative method to functionalize the support electrode is diazonium coupling,[119–123] which can be performed on many electrode surfaces (metal, semiconductor, carbon), but is most commonly employed on carbon electrodes (such as highly oriented pyrolytic graphite (HOPG),[107] and carbon nanotubes[124–126]).

2.2.3 Synthesis of metal nanoparticles followed by immobilization

Optimal control of NP size and shape can be achieved by separating NP formation from the immobilization step, by synthesizing NPs in solution and then attaching the NPs to the support electrode. NPs in solution are most often prepared by colloidal synthesis, an empirical method which offers excellent shape and size control, and requires simple equipment. A rich body of literature has developed since the seminal work by Turkevich,[127] followed up by Brust, Bethell, Schiffrin and co-workers.[128] The principle of colloidal synthesis is straightforward and, in general terms, three components are required for the synthesis: a metal precursor (metal salt) which provides the metal ions, a reducing agent (such as H_2 , BH_4^- or citrate) which reduces the metal ions to metal atoms to form NPs, and a stabilizing agent (such as citrate or various polymers) which limits the size and prevents the NPs from agglomerating. Solutions of the three chemicals are mixed together, causing formation of metal nuclei, which grow by the addition of atoms.[129] The equilibrium shape of a NP, as predicted by the Wulff theorem, is a polyhedron and, at a larger radius, a sphere.[130] The final morphology of the particle can be altered by controlling the kinetics of the growth, for example, by adding surfactants that bind preferentially to specific surface facets, thereby slowing their growth rate.[131, 132] Controlling the conditions allows the tailored synthesis of shape-selected NPs, with specific surface facets exposed, which is beneficial to the catalysis of selected reactions, as described further in Section 2.4.[35, 131–133]

The colloidal synthesis of dendrimer encapsulated NPs is an interesting approach that brings additional control options.[67, 134–140] Dendrimers are hyperbranched, highly regular macromolecules, consisting of a central core from which branched (monomer) units extend.[141, 142] In this approach, metal ions are trapped at functional groups within the well-defined dendrimers before being reduced to the corresponding metal NP. Conceptually, this is similar to the ion-immobilization/reduction approach described above, with the main difference being that the dendrimer is in solution-phase rather than tethered on the electrode surface. Dendrimers are attractive for NP synthesis for a number of reasons. (1) The dendrimer templates can be synthesized with a high degree of control by defining the number of generations (number of 'layers' of monomer units) in the dendrimer synthesis, and the number of ion-anchoring functional groups can thus be controlled. This allows NPs to be synthesized from less than 1 nm to up to 4-5 nm by the number ion-anchoring groups, with a relatively narrow size distribution.[67, 134–140] (2) The NPs are encapsulated within the dendrimers, which serve as stabilizing agents to prevent agglomeration. (3) The open dendrimer struc-

ture and the fact that NP stabilization is mainly due to steric effects leaves a significant fraction of the NP surface available for catalytic reactions. (4) The dendrimer branches can be functionalized to act as selective gates to the NPs. (5) The terminal groups on the exterior of the dendrimer branches can be modified to control the solubility of the dendrimer encapsulated NP or to tether it to electrode surfaces.[143]

An alternative, novel method of NP fabrication has been recently reported under the name 'cathodic corrosion'. In this electrochemical method, Yanson et al. demonstrated that NPs of various metals (including Pt, Au, Cu, Ag, Ni, Rh, Si, Nb, and Ru) and metal alloys (PtRu, PtIr, PtNi, AuCo, AuCu, and FeCo) can be formed from pristine metal wires by simply applying very negative potential of ca. -5 or -10 V to the metal in an aqueous electrolyte containing a strong non-reducible cation, hence the name 'cathodic corrosion'. [144, 145] Application of an alternating voltage aids in dispersing the NPs but is not essential to their formation. Furthermore, it was shown that by tuning the electrolyte concentration and the electrical current, the shape and size of NPs could be controlled.[146, 147] A major advantage of this method is that it offers a similar degree of shape and size control as the colloidal synthesis of NPs, but does not require a stabilizing agent or other additives during the synthesis, leaving the NPs clean. Furthermore, this method is versatile, as it allows the fabrication of NPs of almost any metal and metal alloy.

In order to employ synthesized NPs for electrochemical studies, one needs to immobilize them on the surface. Furthermore, some stabilizing agents on the NP surface may need to be removed to avoid interference with the NP reactivity. The most common method to attach solution-dispersed NPs to support electrodes is by simple drop-casting: an aliquot of a NP-containing solution is placed on the support electrode, and the solvent is left to evaporate, leaving the NPs behind. While straightforward, drop-casting often leads to inhomogeneous deposition with severe particle aggregation, particularly around the edges of the drops, similar to the 'coffee-ring effect'. [148–150] Furthermore, the NPs are only weakly adhered to the surface through van der Waals forces, and NP detachment can be a significant problem.

An alternative way to tether NPs is to functionalize the support to provide specific anchoring sites for the NPs. This can be done by introducing a layer of functional groups onto the surface of the support electrode, through diazonium grafting (see previous Section), or by functionalization with a self-assembled monolayer (SAM), which is terminated with a functional group that binds strongly to the NPs.[151–168] The formation of SAMs on surfaces is a broad research field that has been reviewed extensively.[169–173] SAMs are spontaneously formed monomolecular layers consist-

ing of a head group that interacts with the surface, a molecular chain of variable length, and a terminating functional group. In the context of this review, three main classes of SAMs should be considered, namely alkanethiols[162–168] and alkyl isocyanides[161] for (coinage) metal surfaces (such as gold electrodes), and alkoxysilanes for metal oxide surface (such as silica or doped tin oxide electrodes).[151–160]

To link to the NPs, the SAMs need to be terminated with a functional group that provides an anchoring site for the NPs. Typically, this functional group is a thiol[151, 158, 160, 162–164, 174], amino[151–156, 158, 167, 168] or isocyanide[151, 161] group, as these have a high affinity for metal NPs through the formation of covalent metal-sulfur or metal-nitrogen bonds, thereby displacing the stabilizing agent present on the NPs. An alternative method of tethering NPs is to imbue a charge, typically by depositing a charged polymer (polyelectrolyte) on the support surface with a charge opposite to that of the NPs, thereby binding the NPs electrostatically.[157, 165, 166, 175] By tethering the NPs to the surface through a linker molecule, a more uniform surface distribution with minimal agglomeration can be obtained,[157, 175] as the binding sites to the NPs are regularly arranged in a quasi-two-dimensional plane.

When using the tethered NPs as electrocatalysts, it is imperative that electron transfer (ET) can occur across the SAM between the NP and the underlying substrate. Classically, in the absence of NPs, ET across an insulating layer is determined by the probability of electron tunnelling through the layer. This probability is proportional to $\exp(-\beta d)$, where β is the tunneling decay constant ($\beta \sim 1 \text{ \AA}^{-1}$ for saturated hydrocarbon bridges)[165–167, 176–179] and d is the thickness of the insulating layer. Practically, this exponential decay means that hydrocarbon SAMs (such as alkanethiols) with chains longer than about 10 carbons would essentially completely block ET between species in solution and the electrode surface, and no Faradaic electrochemistry from the redox species in solution would be observed, as has been amply demonstrated.[157, 158, 165–167, 174, 180, 181] Interestingly, the adsorption of NPs on top of the SAM opens up a pathway for ET across the SAM, which was found to be as efficient as in absence of a SAM.[157, 158, 165–167, 174, 180, 181] The groups of Fermín[165, 166, 182] and Gooding,[167, 174, 180] have shown in a series of systematic studies that NP-mediated ET appears to be relatively distance-independent (i.e. $\beta \sim 0$) for typical SAM layers and, furthermore, that ET between the redox species and the NP is the rate-limiting step (rather than ET across the layer).

These findings have been rationalized in a theoretical description of NP-mediated ET by Chazalviel and Allongue.[183] This theory considers ET between: (1) a redox couple and a metal electrode (represented by the exchange current density J_0); and

(2) a metal NP and a metal electrode (represented by the exchange current density J_1) (Figure 2.4a). Typically, J_1 is about twelve orders of magnitude larger than J_0 , unless a NP is particularly small.[183] The introduction of an insulating layer, such as a SAM on the electrode, causes a decrease in the ET rate proportional to $\exp(-\beta d)$ (see above). Typically, J_1 is sufficiently large that even $J_1 \exp(-\beta d)$ is still much larger than J_0 , and adsorption of NPs thus opens up an effective ET pathway across the SAM. An important consequence of this model is that NP-mediated ET is unimpeded by the presence of a SAM as long as the NP is relatively large compared to the thickness of the layer (Figure 2.4b), a prediction which has been validated experimentally by Gooding et al. (Figure 2.4c).[180]

Importantly, the Chazalviel-Allongue theory[183] demonstrates that for NPs tethered to an electrode surface through a SAM, ET across the SAM is only impeded in the case where the NPs are very small (and very monodisperse, as a few NPs above the critical size could already provide an efficient ET pathway), or the SAM is rather thick. Otherwise, NP tethering is an efficient way to immobilize NPs on a support electrode with minimal NP aggregation or desorption, which can also be applied to study electrocatalytic processes.[157]

2.2.4 Cleaning

When a nanoparticulate catalyst is prepared using surfactant-free techniques such as vacuum deposition, electrodeposition, electroless deposition or cathodic corrosion, additional cleaning steps are often not required. Colloidal NPs, however, necessarily have a layer of surfactant molecules on their surface. Since this surfactant film could inhibit the adsorption of reactants in catalytic reactions,[184] it needs to be removed as part of the catalyst preparation.

Solla-Gullón et al. demonstrated the use of CO adsorption at surfactant-coated Pt NPs as a method for NP cleaning.[185] Since CO adsorbs preferentially on Pt, the surfactant is displaced by a monolayer of CO, which can then be stripped off the surface electrocatalytically in a subsequent oxidative potential sweep. The cleanliness of the surface can then be assessed through electrochemical characterization of the nanoparticles, as discussed below. While CO gas should be handled with caution, this method is very successful at cleaning NP surfaces and can be applied to all metals that adsorb CO strongly; for example for the cleaning of Pt[185] and Pd NPs.[186]

An alternative cleaning method was reported by Rodriguez and Koper,[187] showing that the surface of Pt NPs capped with polyvinylpyrrolidone (PVP) can also be cleaned with a diluted sulfuric acid solution containing H_2O_2 , leaving a clean Pt sur-

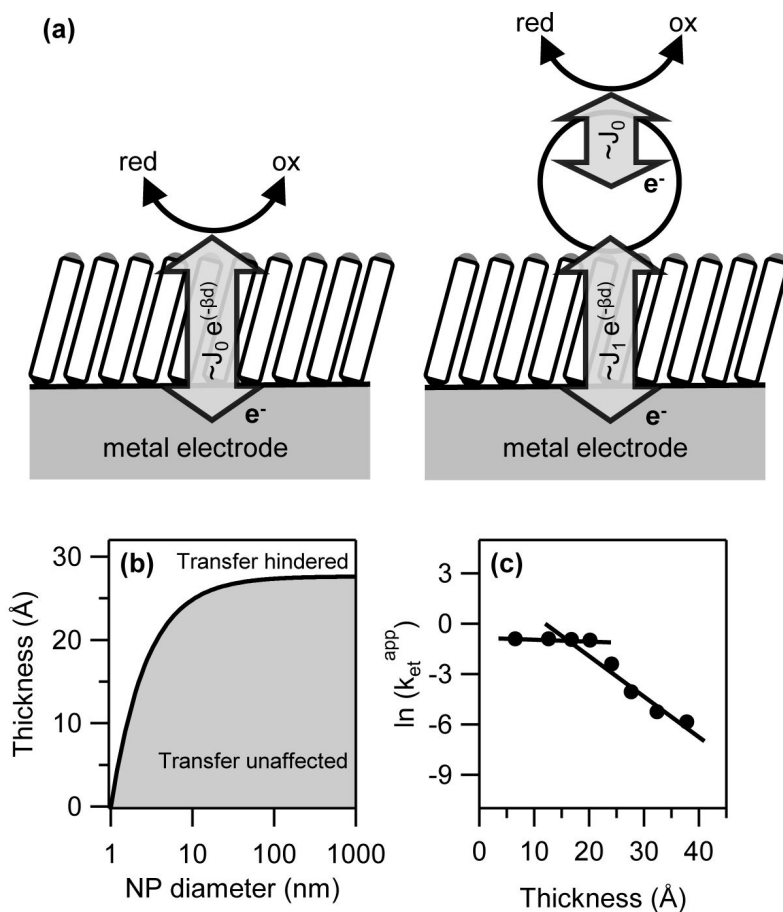


Figure 2.4: a) Schematic comparison of electron transfer between a redox couple and a support electrode across a SAM (left) and nanoparticle-mediated electron transfer (right) Adapted from reference [183]. ©2011, American Chemical Society. (b) Theoretical prediction of the critical thickness of an insulating layer (between a collector electrode and a metal NP) which leads to a change in the voltammogram of a reversible system in solution as compared to a bare metal electrode (adapted from ref [183].) (c) Variation in the apparent electron transfer kinetic constant for the one-electron reduction of $\text{Ru}(\text{NH}_3)_6^{3+}$ to $\text{Ru}(\text{NH}_3)_6^{2+}$ on 27 nm AuNPs with the thickness of an insulating poly(ethylenediamine) layer. Adapted from reference [180]. ©2012, American Chemical Society

face (as characterized electrochemically). Importantly, it was found that this method leaves the superficial order of the NPs intact. It was suggested that the decomposition of hydrogen peroxide on the Pt surface creates oxygen gas bubbles at the NP surface that physically displace the PVP molecules.

The Alicante group of Feliu have also studied the effect on NP surface structure of cleaning catalyst layers using a UV/ozone treatment,[188] as this was reported by Somorjai et al. to increase the catalytic activity of colloidal particles in gas phase catalysis.[189] Through voltammetric analysis, it was found that ozone treatment actually severely perturbs the original surface structure of the NPs, in a way similar to the changes in surface structure resulting from electrochemical oxygen adsorption.

2.2.5 Characterization

After surface adsorbates have been removed from NPs, it is important to determine the NP shape and size and the total NP surface area exposed to the electrolyte. These characteristics can be determined by a combination of techniques that can be roughly divided into electrochemical and non-electrochemical methods.

Electrochemical Characterization

A very accurate way to determine both the exposed surface area and the dominant surface structure of noble metal electrodes is through the study of adsorbed monolayers of atomic or molecular fragments. Examples are the underpotential adsorption and desorption of hydrogen on Pt surfaces (H_{UPD}) and the formation of oxide monolayers.[190, 191] The amount of surface atoms exposed to the electrolyte, or the electrochemically active surface area,[192] can be determined from the charge passed during the adsorption or desorption of a monolayer. Moreover, the voltammetric signature for monolayer formation or monolayer 'stripping' can be very sensitive to the surface structure, as has been shown for hydrogen adsorption/desorption on Pt single crystal electrodes.[190] When applied to nanoparticulate electrodes, an average NP shape can be deduced, from the relative amounts of surface facets measured using such techniques (Figure 2.5).

The analysis of Pt NP shape and surface structure through electrochemical characterization has been extensively developed by the Alicante group.[70, 193] To identify the ratio of the various exposed surface facets on shape-selected Pt NPs, site-specific irreversible adsorption of adatoms was employed. Specifically, it was shown that bismuth and tellurium adsorb selectively on (111) terraces of more than 3 atoms width,

while germanium adsorbs selectively on (100) terrace sites. After adsorption, these adatoms can be stripped, revealing quantitatively the amount of adsorption, and hence values for the amount of each surface. By this method, the relative fractions of (111) and (100) sites were determined for NPs of various shapes, and found to be in agreement with the analysis of the shape of NPs obtained by TEM measurements.[70] Recently, the group reported a detailed characterization of the surface domains on Pt NPs by careful measurement of the hydrogen adsorption and desorption region, as well as the oxidation of CO, in sulfuric acid, perchloric acid and sodium hydroxide electrolytes.[193]

There are fewer reports on the electrochemical characterization of NPs of metals other than Pt, although some methods are noteworthy. The voltammetry of Pd in sulfuric acid also exhibits electrochemical signals corresponding to the adsorption and desorption of monolayers of oxide and hydrogen, that can be used for structure-sensitive determination, and this has been used to characterize Pd NPs.[186] The Alicante group reported the electrochemical determination of the surface structure of Au NPs via the underpotential deposition (UPD) of Pb.[194] The voltammetric signal of Pb UPD is surface sensitive and shows contributions from the three Au basal planes. Nanoparticulate Ru electrodes can be characterized using CO stripping and Cu UPD.[195] In general, CO stripping can be used to determine the electrochemically active surface area of a range of metal NPs.[196–199]

Non-electrochemical characterization

The size and/or shape of NPs may be evaluated through several techniques. Atomic force microscopy (AFM) and X-ray diffraction (XRD) are relatively easily used to estimate NP size. AFM is a scanning probe technique that is highly sensitive to height changes out of the plane.[200] However, its lateral sensitivity is not sufficient to detect the shape of (small) NPs, but the height change with respect to the plane can be taken as the diameter of a NP.[200]

The width of diffraction peaks in XRD is related to the size of the average crystallite in the sample under study, and in the case of (small) NPs it can be assumed that each NP consists of a single crystallite and the NP diameter can then be found via the well-known Scherrer equation.[201] It should be noted that the Scherrer equation depends on the crystallite shape (e.g. spherical or cubic), so that high precision size measurements can only be made by XRD when another microscopic technique is used to determine the NP shape.[201] Since the Scherrer equation yields the average crystallite size, XRD is not a good means to estimate the dispersion of NP sizes.

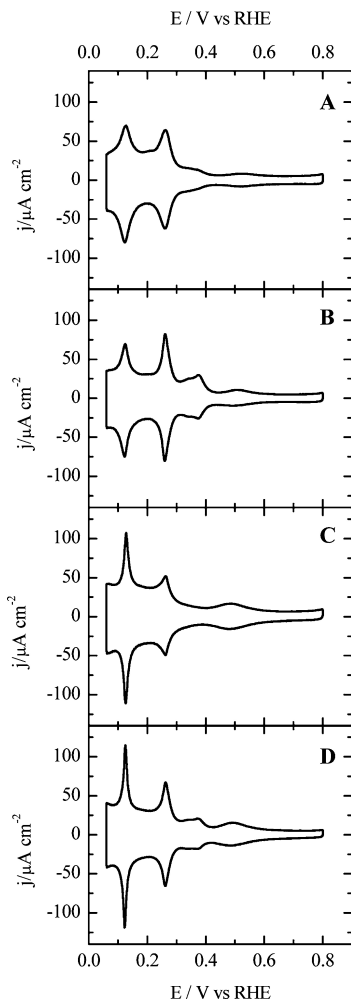


Figure 2.5: Cyclic voltammograms corresponding to (a) spherical (polyoriented), (b) cubic (rich in (100)-type sites), (c) octahedral and tetrahedral (rich in (111)-type sites), and (d) truncated octahedral and tetrahedral (rich in (111)-type and (100)-type sites) Pt NPs in 0.5 M H_2SO_4 (50 mV s^{-1}). Voltammetric features related to different types of sites: peak at 0.125 V for (110)-type sites, peak at 0.27 V containing contributions from (100) step sites on (111) terraces and sites close to steps on the (100) terrace, broad peak at 0.35 – 0.37 V for (100) terraces, and a broad peak at 0.5 V related to (111) terraces. Adapted from reference [193]. ©2012, American Chemical Society

Furthermore, a number of optical methods can be used for NPs with a large photon scattering cross-section for rapid size determination, such as dynamic light scattering (DLS)[202] and NP-tracking analysis (NTA).[203] In DLS, a laser beam is shone through a dilute solution of colloidal NPs, and the light transmission is measured as a function of time. The NPs in solution act as point scatterers. As the NPs move in solution due to Brownian motion, the interparticle distance changes, giving rise to either constructive or destructive interference of the scattered light by surrounding NPs, which causes fluctuations in the transmission. The timescale of these fluctuations can then be correlated with the timescale of the movement of the NPs, from which the diffusion coefficient, and, through equation 2.6 (Section 2.5.2), NP size can be extracted. It should be kept in mind that this analysis is complex, especially for a polydisperse sample. Like DLS, NTA exploits the fact that NPs in solution acts as point scatterers.[203] However, rather than inferring the motion of NPs from the overall intensity of the transmitted light through a NP solution, NTA follows the Brownian motion of NPs directly in real-time. This is done by mounting the cell containing a solution of NPs onto an optical microscope, equipped with a high speed CCD camera, which allows the visualization of the position of individual scatterers (NPs) when a laser beam is passed through the sample. By following the position of many NPs separately over time (typically less than a minute), the average distance moved by individual NPs is calculated, and the size of each individual NP is derived to construct a size distribution.

Importantly, both DLS and NTA rely on measuring the intensity of scattered light, which for NPs much smaller than the wavelength of the incident light can be described by Raleigh scattering.[204] The scattering cross-section is dependent on the refractive index of the material and very strongly dependent on NP size, which limits the applicability of light-scattering based techniques to the characterization of relatively large NPs (> 10 nm) of highly refractive materials, such as gold, silver, and, to a lesser extent, other metals.[204]

Finally, UV-visible absorption spectroscopy can be employed for the size determination of NPs of metals for which the wavelength of absorbed light depends strongly on the particle size. In practice this method is mostly limited to Au and Ag NPs.[205, 206]

To judge the particle size with certainty and visualize the average particle shapes obtained in the synthesis, transmission electron microscopy (TEM) measurements are required. No other measurement technique gives the accuracy level of TEM, which, in modern, high-resolution versions, even allows for the determination of the exposed crystal surface facets per particle.[207] Interestingly, the use of high-resolution TEM combined with electron tomography can accurately image single NPs as well as NP

clusters and has helped in elucidating the growth mechanism of electrodeposited NPs.[96]

2.3 Model approaches to real catalysts

As has been pointed out in the Introduction, it is extremely difficult to extract even the intrinsic (average) activity of NPs from measurements on real catalysts (Figure 2.1a). In this section we discuss approaches that have been developed to mimic the mass transport conditions of fuel cell electrodes and studied the influence of mass transport on catalyst performance in model systems. In the best situations, such experiments use NPs of very well defined size, and/or inter-particle distance. Moreover, the use of flow cells offers a high degree of control over the mass transport of reactants to arrays of NPs. This type of measurements thus allows the accurate evaluation of important catalyst parameters such as the effect of particle size or of catalyst loading on rates and reaction pathways.

2.3.1 Influence of mass-transport

The nature of mass transport towards a nanoparticulate electrode is schematically indicated in Figure 2.6. When the support material is inert, a radial concentration gradient forms from the NPs performing the electrocatalytic reaction creating 'diffusion spheres'. The distance from the electrode where the concentration is 90% of the bulk concentration (or, technically, 90% of the bulk concentration minus the surface concentration) can be considered as the thickness of the diffusion sphere. Overlap between the diffusion spheres leads to the formation of a continuous diffusion layer, and the electrode effectively acts as a planar electrode (Figure 2.6a).

Catalyst NPs in real devices experience rather complex mass transport regimes, critically depending on the interparticle distance, which in turn depends on both the NP size and loading. As the inter-NP distance decreases, there is increasing diffusional overlap between adjacent particles in terms of both reactant diffusion and intermediate/product transport (Figure 2.6b). One particular impact on catalysis that has been seen in the ORR is that the diffusion-limited flux of oxygen to individual NPs in an array decreases and thus the apparent catalytic activity of each NP.[47] The loading of NPs, and the impact on mass transport, is thus an important factor that needs to be accounted for when trying to compare intrinsic NP activities in different studies.

Behm and Kasemo and co-workers have suggested that, for the ORR, overlapping diffusion spheres may also enhance overall catalytic activity.[48] The mechanism of

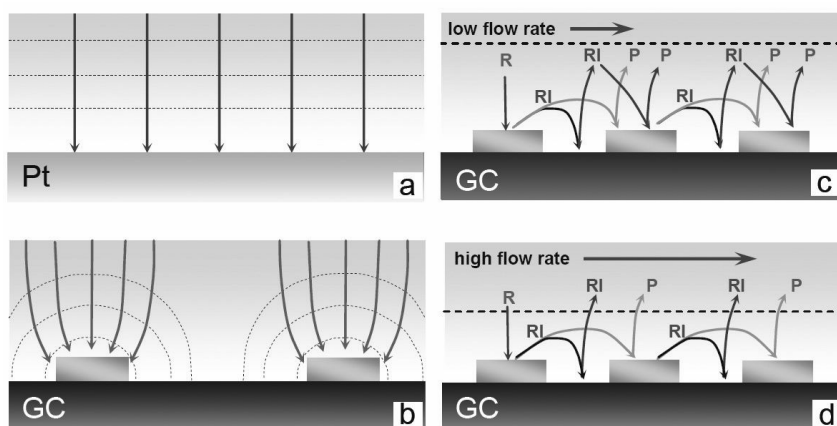


Figure 2.6: Mass transport towards electrodes: diffusion towards an infinite planar electrode is linear (a), while well-separated NPs show radial diffusion spheres (b). As the inter-NP distance is decreased, the diffusion spheres start to overlap. In (c) and (d), the influence of flow rate on mass transport to a NP array is illustrated: at low flow-rate, the diffusion layer is large and there is a chance for reaction intermediates (RI) generated at a NP to re-adsorb on adjacent NPs (c). When the flow-rate is increased, the diffusion layer effectively becomes thinner and RIs are less likely to re-adsorb, escaping from the NP ensemble (d). Adapted from ref [208]. ©2010, The Electrochemical Society.

ORR can proceed via hydrogen peroxide as an (adsorbed) intermediate (reaction k_3 in Figure 2.2) and this species may desorb from the catalyst surface instead of reacting to water, leaving the oxygen reduction incomplete. This aspect of the ORR is also considered below for measurements on individual Pt NPs (Section 2.5.1). In an ensemble, if NPs are in close proximity, there is an increased chance that hydrogen peroxide produced on one NP re-adsorbs on an adjacent NP, and is reduced further to water, as illustrated in Figure 2.6 (c) and (d).[48] The chance that a reaction intermediate will re-adsorb depends on the degree of overlap of the diffusion zones of adjacent NPs. This diffusion sphere overlap can be predicted numerically[209, 210] and also visualized using fluorescence confocal microscopy.[211]

It is apparent from the foregoing that studying the dependence of NP loading and inter-particle distance for highly organized NP arrays is hugely beneficial towards uncovering any subtle influences of NP loading on electrocatalysis. Behm and Kasemo et al. used lithographical techniques to fabricate an array of ~ 100 nm Pt disks on a carbon electrode, that was deployed as a working electrode in a flow cell system, similar to the one shown in Figure 2.7.[212] The effect of mass transport rate could be investigated by: (i) varying the flow-rate of electrolyte over an ensemble of Pt nanodisks (Figure 2.6 c, d) and (ii) varying the radii and inter-particle distance (Figure 2.6b). Increasing the flow-rate (decreasing the diffusion layer thickness) or the inter-particle distance serves to diminish diffusional coupling between neighboring NPs and thus reduces the chance of re-adsorption of RIs.[213] In this setup, a Pt electrode downstream of the Pt NP array was used to quantify the amount of hydrogen peroxide produced.[48] As the NP density was increased and/or the flow-rate was reduced (i.e. the mass transport rate was reduced), the amount of hydrogen peroxide detected downstream diminished. The same effect was also demonstrated for other reactions that feature soluble intermediates, such as the methanol oxidation reaction.[214]

The flow cell in Figure 2.7 was used by Dumitrescu and Crooks to study the effect of flow rate on ensembles of well-defined dendrimer-encapsulated Pt NPs supported on microband electrodes.[215, 216] A key attribute to this type of cell is that the hydrodynamics are very well defined and transport can be varied and controlled over a wide range.[213] Two working electrodes, each decorated with dendrimer-encapsulated Pt NPs, were placed adjacent to each other and perpendicular to the direction of electrolyte flow. The downstream electrode served as a 'collector' electrode, and was held at a potential to oxidize hydrogen peroxide, while cyclic voltammetry was used to measure the ORR on the upstream 'generator' electrode. It was found that even at elevated flow rates, the hydrogen peroxide yield (i.e. the fraction of H_2O_2 formed relative to the

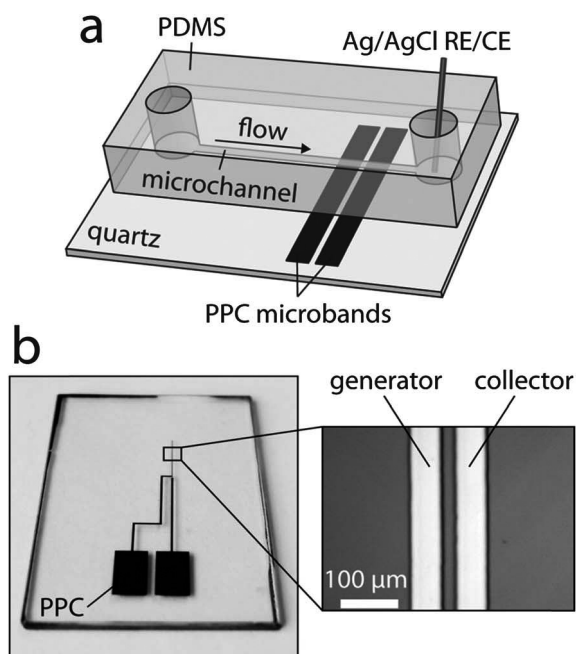


Figure 2.7: Electrolyte in a microchannel in PDMS (polydimethylsiloxane) flows across two pyrolyzed photoresist carbon (PPC) microband electrodes covered with dendrimer-encapsulated Pt NPs; the band closest to the flow source is the generator electrode, performing the ORR and any residual products can be collected at the downstream collector electrode. RE: reference electrode; CE: counter electrode. Adapted from [215]. ©2012, Royal Society of Chemistry.

total amount of O_2 consumed) remained constant.[216]

A constant H_2O_2 yield with the flow-rate was also observed by Behm et al. for extended polycrystalline Pt surfaces (see Figure 5c in reference [48]) consistent with the results of Dumitrescu and Crooks.[216] It should be noted that the dendrimer encapsulated NPs were assumed to form a close-packed monolayer, which may be considered as a planar Pt electrode (Figure 2.6a). This indicates that the relative hydrogen peroxide yield during ORR does not increase with increased flow-rate (mass transport) over high-density planar Pt electrodes, but it does increase at increasing inter-particle distance (i.e. lower catalyst loading).

2.3.2 High throughput electrocatalyst screening

Variations in the electrocatalytic activity for different NP sizes or NP loadings within an array, can be screened particularly effectively using a scanning electrochemical microscope (SECM), a powerful technique for mapping the local reactivity.[217, 218] A reactivity map is made while laterally scanning an ultramicroelectrode (UME; electrode with a critical dimension smaller than the diffusion layer thickness) in close proximity to a larger electrode surface under study. Depending on the nature of the electrochemical reaction, the current is measured at the UME or at the substrate electrode. For instance, the change in the ORR reactivity of an array of microdots containing Pd NPs with increasing Co content was mapped by generating oxygen at the scanning UME and measuring the ORR current of the electrode supporting the array.[219]

Many reports have appeared in recent literature, which have applied SECM to assess a range of different material combinations for fuel cell reactions,[220–223] as has been summarized in the recent reviews.[218, 224] While these studies identify appropriate protocols for measuring ORR activity, a careful study of catalyst activity as a function of catalyst loading (inter-NP distance) and NP size by SECM has not yet been performed. In light of the flow cell studies described above, and others, such screening studies could be very interesting, considering the debate concerning the impact of NP size and loading on electrocatalytic activity that is ongoing (see Section 2.3.1). The use of SECM to investigate electrocatalytic activity as a function of NP shape will be discussed in more detail in Section 2.4. It should also be noted that an interesting aspect of SECM is that the substrate does not need to be a biased electrode. One can use the tip UME to generate a reversible electron donor or electron acceptor that couples to an electrocatalytic reaction enabling studies of electrocatalytic NPs on an inert (insulating support). This approach is thus valuable as a means for studying support effects on ET at NPs. The approach has been used to study the HER

at well-defined arrays of NPs in different environments.[225, 226]

A particularly interesting method of model electrocatalyst screening has been reported by the group of Hayden.[227] To deposit a range of different particle sizes in an array, a masked substrate was used in an ultrahigh vacuum physical vapor deposition (PVD) chamber. Using a PVD source, thin films of single metals or metal alloys (by simultaneously using multiple sources) could be deposited, and by imposing a shutter to partially shadow the source, a range of deposition rates was obtained at different locations on the substrate.[228] Interestingly, if the deposited films were sufficiently thin, they formed nanoparticulate islands rather than a planar film. In this way an array of different NP sizes could be easily generated, since the film thickness varied over the length of the substrate.[229] For these investigations, the substrate was an array of 100 planar microelectrodes (0.8 mm^2) of ternary alloys (such as PdPtAu and TeGeSb) that were individually addressable, each with a different, but well-defined composition.

This approach was applied to the ORR at Pt NPs. For NP sizes from 7 nm to 1 nm the specific activity was shown to decrease sharply.[227] However, it should be noted that with the PVD technique used, the distance between NPs decreased as the particle NP size was increased. Following on from some of the studies discussed above, the difficulty of controlling the inter-particle distance and the mean NP size independently, then makes it difficult to draw definitive conclusions about NP activity.

2.3.3 Stability of nanoparticulate catalysts

In terms of the application of NP catalysts, stability is of paramount importance, as well as the activity and selectivity. Ideally, one would want to study structural changes of real catalysts during operation in a model environment, but in situ structural characterization is challenging. While comparison of the electrochemical surface area before and after a measurement gives some insight into gross structural changes of a catalyst, this is not sufficient to judge unambiguously the mechanism of catalyst degradation and aggregation.

An alternative approach is to measure the structural changes of NPs after 'accelerated aging tests'. Mayrhofer et al. recently reviewed reports of performing such an analysis by a technique called identical location – transmission electron microscopy (IL-TEM) that entailed depositing commercial Pt/C NPs on a TEM grid and subsequently using the grid as an electrode.[230] After an electrochemical aging step performed for several hours, the electrode could be inspected with TEM again. Various types of degradation were identified, namely NP detachment, dissolution and growth. In one case, substantial loss of Pt NPs from the carbon support was observed, which

was attributed to detachment rather than dissolution.[230] For other catalysts however, Pt dissolution was observed, particularly for alloyed NPs such as PtCo NPs. An effect of NP dissolution can be the growth of adjacent NPs, through the Ostwald ripening mechanism,[102, 103] but this has not been observed in IL-TEM measurements, presumably due to the large diffusion distance for Pt ions at the low catalyst loading employed in IL-TEM measurements. While an increase in apparent NP size was found in IL-TEM, this was mainly attributed to agglomeration. Since these effects were often found to occur simultaneously (even on individual carbon support particles) no generally dominant degradation effect could be determined for the Pt NPs. However, the oxidative shrinking of the carbon catalyst support at elevated temperatures and potentials followed by consequent Pt NP migration, was found to be a dominant degradation pathway.

These local results could be extrapolated by measuring the loss of electrochemically active Pt surface area, determined through carbon monoxide stripping voltammetry.[231] However, since the loss of electrochemical surface area can occur via either NP detachment, dissolution, aggregation, or corrosion of the carbon support, electrochemical measurements alone cannot be used to evaluate the exact nature of the catalyst degradation.

Similar degradation measurements were performed in the group of Muller, in which structural information from scanning transmission electron microscopy (STEM) measurements was combined with elemental information through electron energy loss spectroscopy (EELS).[232, 233] After subjecting commercial PtCo alloy NPs to heat treatment, acid leaching, and 30,000 potential cycles in a PEM fuel cell setup, it was reported that NPs grew in a synergetic combination of coalescence and Ostwald ripening. Using EELS, the Co and Pt content could be traced inside individual NPs, revealing that the average PtCo core size did not change, while the Pt skin grew significantly as a result of potential cycling, especially at coalesced particles.[232]

Muller and Abruña et al. used the same setup for an IL-TEM measurement, in which electron tomography was also applied.[233] In this case, the particles were voltammetrically cycled on a carbon-covered Au TEM grid that served as a working electrode in a three-electrode cell, for 30,000 scans between 0.6 and 1.0 V vs RHE. The cyclic voltammograms (CVs) showed a loss in the electrochemically active surface area of ~20% (which was also verified using CO stripping) and a concomitant decrease in the ORR activity. Using STEM, the main cause for the surface area loss could be attributed to NP coalescence, which could be accurately followed using tomography imaging, with no significant change in the PtCo core size. Finally, no obvious degradation

of the carbon support or significant Ostwald ripening of the catalytic NPs was observed in these controlled experiments,[233] in contrast to findings in MEA environments, in which both carbon degradation and NP dissolution has been observed.[234, 235] The authors attributed this contrast to the improved potential control of the three-electrode configuration, limiting the relative mild upper potential limit to 1.0 V, whereas in an MEA the potential can spike up to 1.4 V due to fuel starvation.[235]

2.4 Electrochemistry at preferentially shaped nanoparticles

As highlighted above, the electrochemical performance of metal NPs is typically determined from studies on ensembles of a large number of NPs. However, the inherent dispersion in NP sizes and shapes means that reactivity trends that arise from such studies only reflect the average electrocatalytic behavior of the entire ensemble. Indeed, the overall reactivity of an ensemble may well be dominated by a small fraction of the NPs. These (often poorly reproducible) variations in the dispersion of NP shapes and sizes can make it difficult to compare the findings between different studies. For example, as briefly discussed earlier (Section 2.1.1), contradicting particle size dependencies have been reported for the ORR, as a consequence of difficulties of separating out NP size, shape, coverage, and mass transport effects. In this section, we will discuss an approach to minimize these variations, while still employing large NP ensembles to perform macroscopic measurements, namely the use of NPs with a well-defined (preferential) shape.

Two seminal papers on the preparation of NPs with a preferential shape, through colloidal synthetic methods, were published in 1996, by El-Sayed et al.[236, 237] By tuning the ratio of the Pt precursor and the capping agent (sodium polyacrylate) during the synthesis, mixtures of NPs were obtained with predominantly tetrahedral, cubic, icosahedral or cubo-octahedral shapes (Figure 2.8). This formation of metastable structures (as opposed to the thermodynamically preferred truncated octahedron shape of a metal NP with a face centered cubic (fcc) lattice) is a result of the anisotropic growth of NPs caused by the preferential adsorption of capping agents and/or other shape-directing agents (such as metal ions) on certain facets during growth, inhibiting the growth of those facets.[238] There have been many subsequent reports, adapting the colloidal synthetic method to fine-tune the shape of metal NPs of various materials; advances in the colloidal synthesis of shape-controlled particles have been extensively reviewed. [131, 239–244]

The first electrochemical study of shape-controlled NPs was published by the Alicante group in 2004.[69] The authors employed Pt NPs with preferential {100} surfaces ('cubic' NPs) to study the oxidation of ammonia.[69] From studies using macroscopic single-crystal electrodes, this reaction is known to be very sensitive to the structure of the surface, with the reaction taking place almost exclusively at Pt(100) sites, and proceeding faster on larger (100) domains.[245] Cubic Pt NPs were found to display a four times higher specific activity than spherical Pt NPs. This result mirrored that found macroscopically, suggesting that single crystal electrodes could be used to predict structural effects in NPs in this case.

There have been numerous subsequent electrocatalytic studies on 'cubic' (predominantly {100} facets, figure 2.8a),[193, 246–255] 'hexagonal' and 'octahedral' (predominantly {111} facets, figure 2.8b)[247, 254] and 'tetrahedral-octahedral' or 'cubo-octahedral' ({111} and {100} facets)[247, 252] NPs of various (fcc) metals for a variety of reactions.[244] Usually, such studies find that the reactivity of preferentially shaped NPs is in qualitative agreement with findings from corresponding single-crystal electrode studies, i.e. 'cubic' NPs show a (typically about 3–10 times) higher specific activity than non-preferentially shaped NPs for reactions that favor (100)-type sites.[193, 247–255]

A notable exception to this finding, in which single-crystal reactivity could not be extrapolated to predict the reactivity of preferentially-shaped NPs, was reported by O'Mullane, Bhargava, et al.[254]. The authors compared the reactivity of spherical (rich in {111} facets), cubic (rich in {100} facets) and prismatic (nominally terminated by {111} facets, but rich in defects) Ag NPs for a number of reactions with preferences for different surface sites (oxide formation and stripping, lead underpotential deposition and stripping, hydrazine oxidation, hydrogen peroxide reduction and formaldehyde oxidation), and found that prismatic NPs were the most active for all these reactions. This finding was explained by the high amount of defects in the prismatic NPs, illustrating that, to study structural effects on the level of a NP, characterizing the amount of defects sites is just as important as tuning the morphology of a NP to expose selected facets.

While colloidal synthesis has proven successful as a means of generating preferentially-shaped NPs terminated by basal plane facets, fundamental studies on macroscopic single crystals have shown that many (electro)catalytic reactions favor low-coordination sites, such as steps, kinks and defects.[5, 44] Therefore, to optimize the reactivity of NPs for such reactions, shape-controlled NPs enclosed by high-index facets would be desirable. The colloidal synthesis of such NPs is not straightforward due

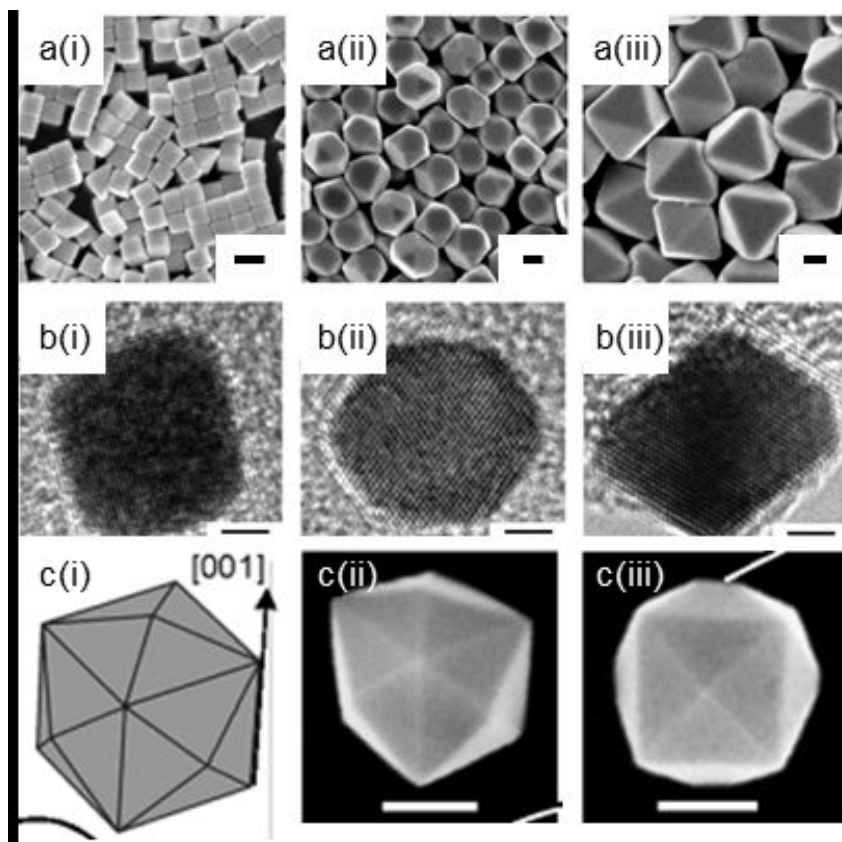


Figure 2.8: Examples of preferentially shaped NPs. (a) SEM images of (i) cubic (bound by $\{100\}$ facets), (ii) cuboctahedral (bound by $\{111\}$ and $\{100\}$ facets) and (iii) octahedral (bound by $\{111\}$ facets) Ag NPs. Scale bar = 100 nm. (b) High resolution TEM images of a (i) cubic (bound by $\{100\}$ facets), (ii) cuboctahedral (bound by $\{111\}$ and $\{100\}$ facets) and (iii) octahedral (bound by $\{111\}$ facets) Pt NPs. Scale bar = 2 nm. (c) (i) Geometric model and (ii-iii) SEM images of a tetrahexahedral Pt NP (bound by 24 high-index $\{hk0\}$ facets, such as 730). Scale bar = 100 nm. (a,b) Adapted from reference [243], ©2011, Wiley-VCH. (c) Adapted from reference [94]. ©2007, American Association for the Advancement of Science.[94].

to the high surface energy of high-index facets, causing them to be eliminated quickly during crystal growth.[256] This problem was overcome by Sun, Wang, et al. who have developed an electrochemical method to prepare NPs terminated by high-index facets.[94, 257]. In this method, 'large' Pt spheres (ca. 750 nm) were electrodeposited on a glassy carbon electrode. Characterization of these spheres revealed that they consisted of small NPs (of a few nanometers). Subjecting these spheres to a square-wave potential treatment (typically 10 Hz, upper and lower potential ~ 1.20 V and ~ -0.20 V vs the saturated calomel electrode, respectively) in an ascorbic acid-containing solution for 10 – 60 minutes caused them to disaggregate into the constituent NPs on the electrode surface, which then underwent dissolution-reprecipitation cycles to form tetrahedral NPs of 20 – 220 nm size, bound by 24 {hk0} facets (Figure 2.8c).[94, 257–262] NPs of other preferential shapes, such as concave hexoctahedral (enclosed by {hkl} facets),[263] trapezohedral ({hkk} facets),[262, 263] and nanorods (various {hk0} or {hkk} facets)[263, 264] and metals (Pt,[94, 263, 265] Pd,[260, 263, 264] Fe,[266] PdPt,[259] and PtRh[262]) have similarly been produced by adjusting the synthetic conditions.[256]

NPs prepared by this method have been employed for a variety of electrocatalytic reactions which are known to be promoted by defects and other low-coordination sites (ethanol oxidation on Pt[94, 261, 263] or Pd[260, 263, 264], formic acid oxidation[94] and nitric oxide reduction on Pt,[265] and nitrite reduction on Fe[266]). These particles were typically found to have up to four times higher specific activities than commercially available catalysts, although it should be born in mind that commercial catalyst are optimized for mass activity (see below) and stability rather than specific activity. A further enhancement in specific activity has been demonstrated by modifying the high-index facets of preferentially shaped NPs with a second metal beneficial for a specific reaction, such as Pd for formic acid oxidation[259] or Rh for ethanol oxidation.[262] This can be done either by preparing bimetallic particles during the synthetic procedure, such as PtPd[259] and PtRh[262], or by surface decoration of preformed (Pt) NPs with ad-atoms, such as Bi,[267] Au[268] or Ru.[269]

While the use of tailored, preferentially-shaped NPs (either enclosed by basal planes or by high index facets) is a seemingly straightforward approach to boost the catalytic activity for some reactions, such NPs are quite large (typically > 10 nm for basal plane-faceted NPs and 20-150 nm for high index NPs) compared to commercial catalysts (2-4 nm). Commercial catalysts thus have much better mass activity (current per gram of NP), which is relevant for technological applications, as this ultimately determines the cost of the catalyst material. Ideally, it would be desirable to decrease

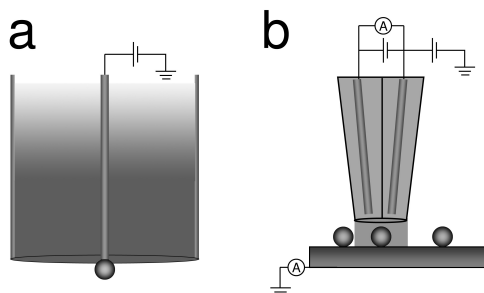


Figure 2.9: Two approaches to study electrochemical reaction at a single NP. (a) A single NP is tethered to a NSE. (quasi reference electrode not shown) (b) The response of a single NP within an ensemble is isolated for investigation. In this example, this is achieved with a scanning electrochemical cell microscopy (SECCM) set-up, discussed in detail in Section 2.5.3.

the size of the preferentially shaped NPs to the 2 – 4 nm regime while maintaining the shape to increase the mass activity, but the synthesis of such NPs is challenging.[258] Furthermore, smaller NPs of this type are relatively unstable due to lower stabilization from the bulk material, and adsorption and reaction of species during electrocatalysis may cause small NPs to change their shape and lose the enhanced activity.

To address the issue of stability of preferentially shaped NPs, Sun et al. have performed a series of molecular dynamics simulations on Pt NPs with various shapes of ca. 5 nm diameter.[270–272] Not surprisingly, it was found that truncated octahedrons showed the highest thermal stability, maintaining their shape up to > 1000 K, whereas preferentially shaped NPs (both basal plane NPs and high index NPs), start to change their overall shape at ~700 K. While this thermal stability seems sufficient for the employment of preferentially shaped NPs in low-temperature electrocatalytic system, the issue of electrochemical stability remains to be investigated. Especially during extended use or repeated start-stop cycles in real applications, the crystalline surface may not be preserved due to oxidation-reduction cycles.[273, 274]

2.5 Measurements of individual metal nanoparticles

The ideal model system is a single NP of well-defined shape and size, studied in an electrochemical cell under potentiostatic control. In this section, we will discuss frontier techniques which have opened up this possibility. Broadly, there are two approaches to study the electroactivity of a single NP (Figure 2.9).

2.5.1 Techniques and Methods

Significant progress has been made on the use of NSEs, which has allowed the measurement of electrochemical processes at electrodes with dimensions down to nanometer dimensions and often with (sub-)pA currents.[32, 275] Fabrication methods for such electrodes were initially based on the encapsulation of sharp (etched) wires, akin to scanning tunneling microscopy (STM) tips, with just the end exposed by sealing in a resist,[276, 277] or by heat sealing in glass.[275, 276, 278, 279] Although very small electrodes can be routinely produced in this fashion, electrodes must be characterized individually before use by a range of techniques in order to determine the actual electrode surface area. Lithographical techniques allow more freedom in the choice of electrode material. Optical lithography was initially employed for the fabrication of UME arrays[280, 281] and electron beam lithography has subsequently been employed to prepare individual NSEs.[282–286]

Alternatively, rather than decreasing the area of an encapsulated electrode material, the contact area of a macroscopic electrode with the electrolyte can be confined to effectively create a NSE. In scanning electrochemical cell microscopy (SECCM),[111, 287–297] an electrolyte droplet at the end of a double-barreled theta capillary, which has been drawn to a very sharp tip, contacts a macroscopic electrode surface. Conventional electrochemical measurements can be made between the exposed electrode surface and (quasi-)reference electrodes contained in the barrels. Furthermore, this configuration also allows two-dimensional maps of localized electrode reactivity to be obtained, as discussed in detail in Section 2.5.3. This technique improves on related microdroplet techniques in terms of the spatial resolution attainable and information content of experimental data.[298–302]

Ideally, to characterize the electrocatalytic activity of metal NPs, one should aim to probe them individually, to determine the impact of particle size and shape on catalytic performance directly and unambiguously. However, the direct characterization of the surface of a single NP is extremely challenging. For example, noble metal electrodes are often characterized by measuring the formation and stripping of an oxide monolayer (see Section 2.2.5), with a charge of approximately $400 \mu\text{C cm}^{-2}$. [192] For NPs with radii of 10 nm and smaller, this corresponds to ca. 10^{-15} C or less. Measuring such small charges requires very high accuracy current amplifiers with a fast response time, which is a fundamentally difficult combination, although promising results have been reported for state-of-the-art integrated amplifier-electrode systems.[303, 304] On the other hand, diffusive processes, such as outer-sphere reactions and some electrocatalytic processes (e.g. hydrogen evolution and oxidation, hydrazine oxidation,

oxygen reduction) are more readily measurable, as will be shown below. The limiting current at an isolated catalyst NP (with diffusion as the sole mass transport mode) is manifested in a steady state current (I_{ss}):[305]

$$I_{ss} = nFAkTC = nFA\chi DC \quad (2.4)$$

where F is the Faraday constant, n the number of electrons transferred during the reaction, C the bulk concentration of the reactant, A the surface area of the particle, and kT the mass transport coefficient, which is the product of a geometry factor (χ) specific to the NP arrangement, and the diffusion coefficient of the reactant species (D). χ is $\ln(2)/r$ for a sphere on an infinite plane,[306] $1/r$ for a perfect (hemi-)sphere, and $4/\pi r$ for an inlaid disk, where r is the radius of the (effective) electrode (NP).[305] Taking the four electron ORR in an oxygen-saturated aqueous solution (ca. room temperature) as an example ($C \approx 1$ mM, $D = 1.8 \times 10^5 \text{ cm}^2 \text{ s}^{-1}$), a 5 nm radius spherical particle on a plane gives a steady-state current of ~ 15 pA, which is well within the capabilities of commercial current amplifiers.

2.5.2 Immobilized nanoparticle measurements

An obvious method to measure the electrocatalytic activity of an individual NP, is to immobilize it onto a nanoscale support electrode, ensuring that the NP response can be measured, with a low electrochemical background current. This approach is exemplified by the work of Kucernak et al.,[38, 49, 307, 308] who electrodeposited a single Pt NP on (the end of) a carbon nanofiber (Figure 2.10), a support showing negligible Faradaic activity over a wide range of potentials.[307] The nanofiber was first sealed in a layer of electrophoretic paint with only the apex left uncoated, to minimize the conductive area. Subsequently, Pt was electrodeposited using potential pulses of well-defined duration, with the pulse length correlating to the final particle radius.[38] In this way, the influence of NP radius was investigated for the kinetics of the ORR and HOR.[49, 308] For the ORR (in 0.1 M H_2SO_4), an effective number of electrons, n_{eff} , of 3.5 was found in the diffusion-limited regime for NPs smaller than 100 nm. This number was inferred from the diffusion-limited current using equation (2.4), for which χ was determined using the HOR ($n=2$) on the NP electrode, and D obtained from UME measurements.

The effective number of electrons transferred per O_2 molecule depends on the relative yields of hydrogen peroxide (2 electrons per O_2 molecule) and water (4 electrons per O_2 molecule). A transfer of only 3.5 electrons per oxygen molecule implies that 25

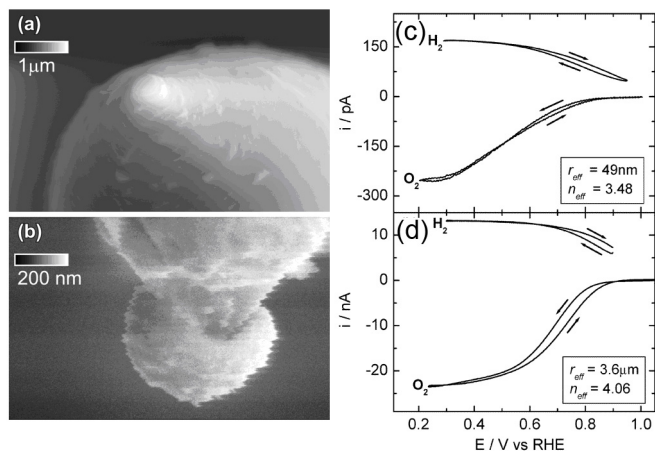


Figure 2.10: A Pt NP electrodeposited at the apex of a carbon tip (a,b). The kinetics of ORR and HOR are a function of the radius of the particle as evidenced for two different radii (c and d). Adapted from references [38] (©2003, American Chemical Society) and [308] (©2004, American Chemical Society).

% of the oxygen is converted to hydrogen peroxide without reacting further to water (see Figure 2.2, Section 2.1.1). For particles smaller than 100 nm the mass transport ($kT > 2 \text{ cm s}^{-1}$) is so fast that some of the H_2O_2 produced escapes the electrode vicinity and is transported into the bulk electrolyte. These findings are consistent with the proposed mechanism on the role of mass transport in NP ensembles outlined in Section 2.3, at least qualitatively. It should be noted that these measurements were conducted without detection of hydrogen peroxide, which would have underpinned the mechanistic interpretation of the data.

The extremely fast mass transport to and from individual NPs allows the study of reaction mechanisms in potential regimes where the current is normally dominated by diffusion limitation (e.g. in rotating disk electrode measurements). Thus, for particles smaller than 50 nm ($kT > 4 \text{ cm s}^{-1}$), no clear mass-transport limited current was observed. It was reasoned that at these high mass-transport conditions, significant kinetic limitations pushed the ORR into the potential domain where hydrogen adsorbs on the Pt surface (H_{UPD}).

In the HOR, the high mass transport conditions of the experiment allowed the observation of an extra current plateau in the H_{UPD} . Fitting the CVs by a kinetic model, the Tafel-Volmer mechanism was found to be the dominant mechanism rather than the Heyrovsky-Volmer mechanism, as discussed in the Introduction (Section 2.1.1).[49]

Individually electrodeposited particles were also used in a study by Bard et al.,[309] where a carbon fiber, biased at the Pt electrodeposition potential was covered with a film of electrophoretic paint containing pinholes. As the fiber was gradually immersed into a solution containing Pt(II) ions, a cascade of reduction transients was measured as a function of the tip immersion depth, indicating Pt deposition at the pinholes. Subsequently, slow immersion into a fresh electrolyte containing Fe_3^+ (enhanced reduction kinetics on Pt with respect to C) showed discrete increases in the reduction current as the freshly generated Pt NPs gradually came into contact with the solution, so that the contributions of the different particles were separated in time and space.

Poor control over NP shape is a major disadvantage (Section 2.2.1) of using electrodeposition to immobilize a particle on an electrode, and particle stability on the support has been reported to be problematic.[309] To circumvent these problems, single colloidal NPs with fine-tuned shape and size can be attached to a NSE with radius equal to or smaller than the NP size from a dilute colloidal solution.[154, 168, 310] However, it is not trivial to produce, handle and characterize NSEs with radii below 10 nm,[311–314] and there is a restriction on the choice of electrode materials.[315]

Zhang and co-workers immobilized a single Au NP on an oxidized Pt NSE through a silane linker terminated with an amino group. An individual NP was found to adhere to the modified electrode (in TEM analysis), when it was immersed in a solution containing NPs.[154] Similarly, Sun et al. reported the attachment of a single Pt NP on a Au NSE through an alkanethiol linker.[168, 312] In another experiment, the surface of a Pt NSE was not modified, but cycled voltammetrically in a solution containing Au colloid. When a reduction current was observed in the CV this was interpreted as the arrival of a single Au NP.[310] Electrochemical analysis of these individual probes included the deposition of Cu monolayers[154] and the measurement of Au blank CVs in sulfuric acid.[154, 310] Both of these methods can be employed to determine the electrochemically active surface area of an electrode,[192] but as mentioned earlier, such surface electrode measurements are challenging, and in these particular studies the surface area was significantly overestimated compared to ex situ electron microscopy measurements. The authors tentatively rationalized this by suggesting that the bulk Au atoms were also oxidized in addition to the surface atoms, leading to Au reduction charges higher than expected.[310] Unexpectedly, ORR measurements revealed a lower overpotential for Au NPs compared to the bare Pt disk UME, but a much smaller diffusion-limited current, suggesting that the Au NP was not participating fully in the reaction.[154] Regardless of these inconsistencies, these experiments indicate the possibility of immobilizing single catalyst NPs and studying their reactivity and we

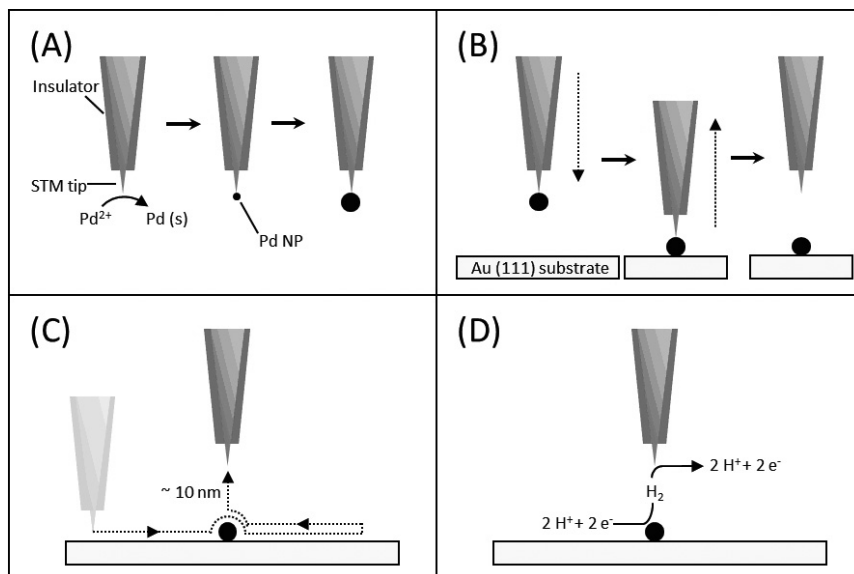


Figure 2.11: Schematic representation of the single NP experiment by Stimming et al.[54] Through electrodeposition, a Pd NP is formed at the tip of an STM probe (a), which is then deposited onto an Au surface (b). The surface-immobilized NP is imaged with the tip (c) and the tip is then moved back 10 nm and used in 'collector-mode' (i.e. as an SECM tip) to detect H_2 produced by electrocatalysis at the NP (d). Adapted from reference [218]. ©2012, Cambridge University Press.

anticipate much further development in this field.

Rather than immobilizing the NP on a very small electrode, one might choose to deposit particles at a known location on a macroscopic electrode using the high spatial resolution afforded by scanning probe techniques, such as scanning tunneling microscopy (STM), as shown in Figure 2.11. Once the NP is on the macroscopic electrode and located by the STM tip, it is biased to promote an electrochemical process of interest, and the probe tip (moved back by $\sim 10 \text{ nm}$) then serves as a collector electrode to detect any generated products in an SECM-type configuration. In this way, the HER kinetics at a single Pd particle was studied by applying different potential pulses to the substrate and measuring the collector current.[54] The reaction rates were found to decrease with increasing NP height (total amount of Pd layers). In fact, NPs consisting of less than 5 Pd layers were found to be orders of magnitude more reactive than those with more layers. This effect was modeled using density functional theory calculations, and it was interpreted as arising from the strain induced on the Pd NP due to the lattice mismatch with the underlying Au(111) substrate. The strain increases the average

Pd-Pd distance, on which the HER reactivity is primarily dependant.[316] While this method presents an elegant way to study size effects on electrocatalysis at a single NP, the interpretation of the experimental results is not straightforward and has led to considerable discussion.[317] Nonetheless, this type of measurement demonstrates the insights offered by SECM-type measurements using ultras small probes.

2.5.3 Nanoparticle landings

It is not necessary to pre-immobilize NPs on an electrode as in the approach described in Section 2.5.1; their arrival at electrodes from a (dilute) colloidal solution may also be detected electrochemically. When an electrocatalytically inert UME is immersed into a solution containing both a reactant and a catalyst NP, on which that reactant can be turned over, a current signal is measured whenever a NP is polarized by colliding with the UME. This approach can be traced to the studies of Heyrovsky et al. who showed that the reduction of polydisperse ceramic semiconductor NP colloids contributed to the cyclic voltammetry of a Hg drop electrode by a summation of cathodic steps that had an onset potential dependent on the particle size.[318–321] In a later study on the interaction between metallic NP colloids and an Hg electrode, it was found that the cathodic waves measured consisted of discrete contributions from the reduction of the oxidized NPs arriving at the electrode.[322] It has also been demonstrated that the faradaic current at an UME performing a redox reaction decreased in discrete steps upon the addition of insulator microparticles. Optical microscopy indicated that the blocking of the electrode by these particles was the cause for the diminished current.[323, 324]

The first detection of NPs through electrocatalytic amplification (Figure 2.12) was demonstrated by the Bard group, using a carbon UME with Pt NPs in solution, held at a potential at which hydrogen evolution would occur on Pt but not on carbon. Current spikes were detected with a frequency that could be roughly correlated with the expected diffusional flux of NPs toward the electrode surface (*vide infra*).[306] This type of experiment has since been reproduced by several research groups for a number of combinations of the electrode material, the NP material and the reactant molecule, as well as variations in the experimental set-up and coupling with other techniques (see Table 1). Broadly speaking, two distinct types of reactivity have been observed: a cumulative cascade of current steps ('a staircase') and a series of transiently decaying current jumps ('spikes'). A current staircase is expected for the landing of NPs on an electrode that catalyze a reaction continuously. Current spikes are observed when NPs continuously arrive at a surface, but their reactivity is finite.

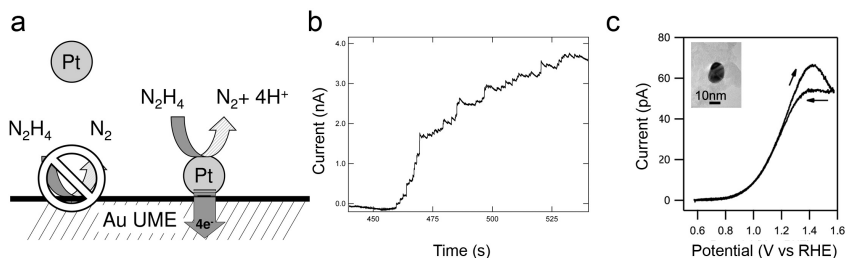


Figure 2.12: An inert UME is in a solution containing an electrocatalytic reactant and catalyst NPs; as NPs impact the surface they convert the reactant and a current is measured (a). If the NPs stick to the surface, the current contribution is continuous, resulting in a staircase-type current-time plot (b), as at an Au UME in presence of Pt NPs in a hydrazine-containing solution. (c) Cyclic voltammogram (200 mV s^{-1}) for the oxidation of 2 mM hydrazine at a single Au NP (shown in inset) on a TEM grid electrode. Adapted from references [327] (©2013, American Chemical Society) and [293] (©2012, American Chemical Society.)

Electrocatalytic current step heights measured when NPs land on an electrode can provide an insight into the particle size, through equation (2.4). This is well-illustrated by several studies of the oxidation of hydrazine at Pt NPs landing on Au UMEs, [293, 325–328] where the landing frequency and current step height distributions were in reasonable agreement with the concentration and size distribution of the NPs as determined by other methods, such as TEM. [325] However, it should be noted that the size of NPs can only be determined accurately from diffusion-limited reactions if the diffusion coefficient of the reactant molecule is known or can be determined with a high degree of certainty. This may appear to be a trivial and obvious point, but is particularly troublesome for hydrazine, a popular reactant for this type of experiment for which the reported diffusion coefficients show a significant spread, ranging from $\sim 10^{-8}$ to $\sim 10^{-3} \text{ cm}^2 \text{ s}^{-1}$, with typical values between $0.6 - 2.0 \times 10^{-5} \text{ cm}^2 \text{ s}^{-1}$. [55, 56, 329–332] This has a corresponding impact on the use of amperometry to determine NP size, considering that the limiting current depends linearly on the diffusion coefficient (equation 2.4).

To confirm that Pt NPs catalyze the hydrazine oxidation, Bard et al. studied the effect of treating the particles or the UME with self-assembled monolayers (SAMs). [326] When an UME was treated with an alkanethiol with a chain length up to 12 methylene units, landings of as prepared (citrate-capped) Pt NPs could still be detected, but the magnitude of the current step per landing decreased with increasing chain length. The authors suggested this to be due to the suppression of electron tunneling from the

NP through the SAM to the UME,[326] although this would appear to be contradict to the Chazalviel-Allongue model (see Section 2.2.3).[183] Conversely, if the NPs were capped with an alkanethiol SAM, the ability to detect their landing was significantly reduced when the carbon-chain length was increased; even for the shortest chain length of three carbons a much lower landing frequency was detected. Capping the NPs with other stabilizing molecules typically used in NP synthesis, such as polyvinylpyridine (PVP) and cetyltrimethylammonium bromide (CTAB) resulted in a similar loss in the ability to detect collisions. These findings were rationalized as follows: hydrazine oxidation requires certain catalytic surface sites on the NP, which are blocked by strong capping agents, whereas ET from the NP to the UME is governed by electron tunneling (and is thus relatively insensitive to the nature of the capping agent)[326] Aside from proving the proposed mechanism of detection of NP landing, this method could also be used to evaluate charge-transfer between a NP and electrode through organic molecule SAMs.

The inability to detect NPs after changing the NP capping is one reason why the majority of successful NP landing experiments makes use of citrate-capped NPs. The interaction between citrate and the NP metal surface is such that the surface reactivity is not hindered significantly, while electrostatic repulsion between NPs in solution limits aggregation. The adsorption strength of citrate on Au surfaces is comparable to that of anions such as sulfate,[333, 334] which is known to diminish, but not block, catalytic reactivity,[44] while organic molecules such as PVP and CTAB have a stronger surface interaction and tend to inhibit catalytic activity more significantly.[184]

Rather than using conventional glass-sealed UMEs, Kleijn et al. employed lithography to fabricate Au UMEs as the support electrode for NP landings.[327] They found that the landing frequency for Pt NPs (using hydrazine or hydrogen as the reactant) was much lower than expected and that the distribution of current step magnitudes from a series of landings showed significant tailing at higher current values.[327] Both the lower landing frequency and the observation of larger currents could indicate a reduced effective NP concentration, which was attributed to the aggregation of NPs in solution. Aggregated NPs were observed by scanning electron microscopy (SEM) on the support electrode after a landing experiment. However, when NPs were landed in absence of hydrazine or hydrogen, no aggregates were detected on the UME, demonstrating that NPs in solution can aggregate by interaction with the reactants added for NP detection. It was proposed that the weakly bound citrate molecules were displaced by the hydrazine or hydrogen and that the diminished electrostatic repulsion resulted in aggregated NPs.

An alternative platform to prepare an electrode for NP landing experiments is by using SECCM, as recently introduced by Unwin and co-workers.[293] A SECCM probe, containing an electrolyte solution with Au NP colloids, was moved slowly towards the working electrode until the meniscus at the end of the pipette made contact with the conductive substrate, thereby forming a nanoscopic electrochemical cell to perform NP landing experiments. Compared to the landing experiment describe above, that employ preformed UMEs, this approach offers a several key advantages. First, a wide range of materials can be used for the support electrode, as no traditional UME manufacture is required. Second, the cell can be made and broken at will on a millisecond time-scale at specified locations. Finally, ultras-small electrode areas can readily be achieved by employing pipettes with smaller diameters, offering a significant decrease in background current.

The high sensitivity of this approach was demonstrated by measuring Au NP landing experiments on highly oriented pyrolytic graphite, a carbon support with very low background currents for which it is unfeasible to prepare a UME or NSE by conventional methods. The landing of Au NPs was detected throughout various potentials for the ORR and HER processes, including potentials at which the magnitude of the individual current steps was less than 1 pA. The versatility in the choice of substrate was further emphasized by landing Au NPs onto the carbon foil of a TEM grid which was connected as a working electrode, using the oxidation of hydrazine as a probe reaction. After the first current step (indicating the arrival of a single NP at the TEM grid), the tip was retracted and the grid was characterized by TEM, allowing a correlation to be made between the current magnitude of the landing step and the NP size. An estimation of NP sizes from the current responses, using equation 2.4 provided values that were in good agreement with the actual NP sizes.[306] Additionally, a cyclic voltammogram of hydrazine oxidation on a single gold nanoparticle could be measured, as shown in Figure 2.12c. This approach has considerable promise for structure-reactivity measurements at the single NP level.

Bard and co-workers have diversified combinations of NP metals and electrocatalytic reactants that can be studied by NP landing. Thus, Au NPs were detected through the oxidation of borohydride, which can be suppressed on Pt UMEs that have been pre-oxidized. These collision measurements showed spiked responses, suggesting that the NPs either desorbed from the electrode surface or stayed in place, but became deactivated.[335] Similar results were found for the detection of iridium oxide (IrO_x) NPs using the OER; since IrO_x is more active than Pt for the OER, current spikes could be observed at a potential just below the onset of OER current on Pt

UMEs.[336] To gain additional insight into the current decay transient observed for IrO_x NPs, the landing detection was performed in an SECM configuration where a macroscopic surface (2 mm diameter Pt disk) and a Pt SECM tip (5 μm radius) were held in close proximity (i.e. 50 μm separation) and biased at the same potential (0.8 V vs Ag/AgCl).[337] NP landings were monitored at the SECM tip while the macroscopic disk acted as a NP sink (shielding experiment). The landing frequency of IrO_x NPs was seen to decrease as a function of time, due to NP adsorption at the macroscopic electrode. It was thus deduced that the current-time transient for the OER at IrO_x NPs was due to irreversible sticking and subsequent deactivation rather than to an intermittent contact between the NP and the collector UME.

The Compton group[338] has adopted the NP landing methodology to measure the size distribution and concentration of NPs in solution, through a method coined 'anodic particle coulometry' (APC).[339] When a NP contacts a glassy carbon UME that is held at a potential to promote electrodisolution of the metallic NP to its constituent ions, an anodic current-time transient is measured. By measuring the charge transferred in the transient, the amount of atoms per NP can be determined, and the original particle size distribution can be derived if the average particle shape is known.

landing frequency (in 10 ⁴ s ⁻¹ pM ⁻¹ cm ⁻²)	Reaction	Response type	NP material / size	UME material / radius	Reference
8.0	HER	Spike	Pt / 4 nm	C / 4 μm	[306]
2.4 – 4.0	HZ Ox	Staircase	Pt / 4 nm	Au / 5 μm	[325]
1.3 – 0.71	NaBH ₄ Ox	Spike	Au / 14 nm	PtO / 5 μm	[335]
8.9	OER	Spike	IrO _x / 28 nm	Pt / 5 μm	[336]
0.0071	HZ Ox	Staircase	Pt / 4 nm	Au [†] / 2000 μm ²	[327]
4.0	Red Ox	Staircase	Au / 20 nm	C [†] / 0.5 μm	[293]
3.9	Ag NP Ox	Spike	Ag / 20-50 nm	C / 11 μm	[338]
2.4	Th UPD	Spike	Ag / 45 nm	C / 11 μm	[340]
3.2	Cd deposition	Spike	Ag / 45 nm	C / 11 μm	[341]
4.1	Ag NP Ox	Spike	Ag/14,29,45nm	C / 11 μm	[342]
5.2	H ₂ O ₂ Red.	Spike	Ag / 14 nm	C / 5 μm	[343]
2.6	NTP Ox	Spike	Ag / 45 nm	C / 11 μm	[344]
0.33 – 0.49	HZ Ox	Spike	Pt / 4, 12, 22nm	Hg@Pt/12.5μm	[328]
0.25	HZ Ox [#]	Spike	Pt / 16 nm	Au 5 μm	[345]

Table 2.1: Comparison of landing frequencies of NPs measured in different reports. Measurements were made at disk-shaped UMES, except where [†]a rectangular, lithographical electrode was used and [†]measurements performed in a (SECCM) droplet cell setup. [#]Detection by measuring change in the open-circuit potential.

The formation by electrodeposition of a metal shell on a NP upon impact has also

been reported: for impacting Ag NPs, current peaks were measured at potentials below the Ag oxidation potential, in the presence of ionic thallium[340] or cadmium.[341] The integrated charge passed during each spike could be related to the amount of monolayers of metal deposited on the NP. Depending on the applied potential and the depositing metal, both the underpotential deposition (UPD) and the bulk deposition of metals could be achieved. In another report, the oxidation of adsorbed molecular monolayers from metal NPs was shown to be measurable.[344, 346]

The landing of Pt NPs at a Hg-modified Pt UME has also been reported by Stevenson et al.[328] Since Hg is a very inert electrode material for electrocatalysis, it is an interesting candidate to use for the electrocatalytic detection of NP landings, as illustrated earlier in the pioneering studies of Heyrovsky et al. on NP detection.[318–321] First, a thin film of Hg was formed on the Pt UME by electrodeposition. The Pt NP landings were then measured by the oxidation of hydrazine, which appeared as spikes rather than a staircase response. It was argued that the Hg thin film passivating the Pt UME amalgamates with the Pt NPs, thereby deactivating them.

Quantitative analysis of nanoparticle landing measurements

Attempts have been made to correlate the NP landing frequency to diffusion-based mass transport of particles towards the collector electrode, which is assumed to occur when a NP concentration gradient builds up near the electrode which acts as a sink for NPs.[347–350] The landing frequency is then expected to scale with the UME radius, from the diffusion limited flux function for inlaid microdisk geometry (analogous to equation 2.4):

$$f_{NP} = D_{NP} C_{NP} r_{UME} \quad (2.5)$$

where f_{NP} is the landing frequency, D_{NP} and C_{NP} are the NP diffusion coefficient and NP bulk concentration and r_{UME} is the disk UME radius. The NP diffusion coefficient can be estimated from the Stokes-Einstein equation:

$$D = \frac{k_B T}{6\pi\eta r_{NP}} \quad (2.6)$$

where η is the dynamic viscosity of the solution ($\eta \sim 8.90 \times 10^{-4}$ Pa s for dilute aqueous solutions), r_{NP} is the NP radius, k_B is the Boltzmann constant ($k_B = 1.381 \times 10^{-23}$ J K⁻¹), and T is the temperature. However, landing frequencies predicted from the simple diffusion model of equation 2.5, consistently overestimate the landing frequency when compared to experimental data in Table 1.

Experimentally, the landing frequency has been shown to correlate with the radius of the electrode,[347] the concentration of NPs,[325, 328, 338, 347] and the viscosity of the solution.[347] However, the NP size should also influence the landing frequency as the diffusion coefficient depends reciprocally on the NP radius, r_{NP} , through equation 2.6. Therefore, as the NP size is increased, the NP diffusion rate and consequentially the NP-UME collision frequency should decrease. For the NP sizes reported in the literature, with radii in the range 2 to 25 nm (as summarized in Table 1), an order of magnitude difference in the diffusion coefficient is expected. However, such a correlation is not evident even though many different NP sizes have been studied to determine the influence of the NP radius on the magnitude of the current response.[325, 328, 338]

The apparent overestimation of landing frequency when using equation 2.5 suggests that this equation does not model real NP landings particularly well, and that a more detailed model should be formulated. Attempts at modifying the original model have been made, for instance by the introduction of a factor that takes into account that not every collision results in NP sticking, and not every sticking NP might yield a measurable response.[347] Another possible explanation for the diminished collision frequency could be due to NP collisions on the insulating sheath surrounding the in-laid metal electrode. The area of the sheath is typically several orders of magnitude larger than that of the collector electrode, and if the sticking probability of NPs onto the sheath was finite, it could act as a NP sink and effectively shield the collector electrode.

Another issue in the quantitative description of NP collisions is that the shape of the current response measured does not always match the expected behavior. For instance, for the HER on Ag[338] or Pt[306] NPs on GC UMEs, current spikes are detected rather than the staircase expected of NPs at which the electrocatalytic reaction is continuous. On other carbon substrates (HOPG and TEM grid C foil),[293] a staircase-type current increase has been reported for the hydrazine oxidation and ORR, indicating cumulative sticking of NPs on the electrode surface. Moreover, for the oxidation of NaBH_4 on Au NPs[335] and oxygen evolution on IrO_x NPs[336] at passivated Pt electrodes, current spikes are detected instead of a staircase response. Also, the detection of Pt and Au NPs on boron-doped diamond UMEs via the hydrazine oxidation reaction showed a staircase response for Au NPs, and current spikes for Pt NPs.[351]

Interestingly, landing frequencies obtained with the different characteristic current responses (i.e. spike or the staircase characteristic), are very similar, even though it has been suggested that the spike response corresponds to a non-sticking interaction with the electrode. It was reasoned by Bard et al. that the interval in which a non-

sticking NP is in close proximity to the electrode to experience multiple collisions is too short to be resolved using conventional electrochemical techniques.[347] Therefore, the UME-NP interactions are 'bunched' into a common current response. The frequency of the current response is then equivalent to the diffusion of the NPs towards the electrode and the landing frequency is that of sticking particles. Thus, the landing frequency cannot be used to distinguish between different interactions of the NP and the UME.

Based solely on the electrochemical NP landing detection it is difficult to differentiate between sticking followed by deactivation and a transient, 'bouncing' interaction, since the transient electrochemical signal and the landing frequency alone do not contain enough information to make this distinction. The staircase responses measured in electrocatalytic NP sticking experiments also show a decay on a long (i.e. seconds) timescale.[325, 327] The charging time of the double-layer, or the electrical time constant of the measurement system are much smaller than this and do not explain the current decay. Physical effects, such as the contamination of the catalytic surface by trace amounts of poisonous species in the electrolyte could cause the transient effect, by deactivating the NP. In the groups of Koper and Unwin, electron microscopy was used to show that, after landing was detected via a staircase current, NPs remained on the electrode after the detection measurement.[293, 327] The current spikes observed by Bard et al. during the landing of IrO_x NPs were shown to be due to NP deactivation, rather than desorption, by using SECM,[337] although ex situ electron microscopy would provide a more definitive conclusion for such studies.

2.5.4 Measurements at the single nanoparticle-level within nanoparticle ensembles

Recently, there has been a renewed impetus to study NP ensembles at the level of a single NP with the development of novel frontier techniques. One such technique is SECCM, discussed briefly above and shown in more detail in Figure 2.13a. SECCM employs a dual-barrel (theta) pipette as a probe, pulled to a sharp point with a laser puller to the desired dimensions ($\sim 100 \text{ nm} - 50 \mu\text{m}$). Ultimately, the dimensions of the pipette determine the spatial resolution of SECCM. After rendering the outer wall of the pipette hydrophobic, both barrels are filled with an electrolyte solution of interest, and a quasi-reference counter electrode is inserted into each barrel. A small potential bias is applied between the two quasi-reference counter electrodes (QRCEs) to induce an ionic conductance current across the electrolyte meniscus at the end of the tip. The potentials of the QRCEs can be floated with respect to ground, while maintaining the

potential bias between them, to set the effective potential at the substrate, which is held at ground.

To obtain two-dimensional maps of substrate reactivity, the electrolyte meniscus at the end of the pipette is brought into contact with the substrate. This is aided by a small oscillation (typically 10-30 nm) applied to the pipette in the direction perpendicular to the substrate, that causes a periodic deformation of the meniscus and gives rise to an alternating current (ac) component to the ionic conductance current. The ac magnitude is strongly sensitive to the distance between the end of the pipet and the substrate, and can be used as a feedback parameter to maintain a constant separation while scanning across the surface, producing two-dimensional maps of surface activity and surface topography simultaneously.

By employing pipettes of a size smaller than the average interparticle distance, Lai et al. studied electrocatalytic Pt NPs within an ensemble directly with SECCM (Figure 2.13).[111] The Pt NPs were prepared by electrodeposition on a single, isolated carbon nanotube supported on a silicon-silicon oxide wafer. The carbon nanotube not only served as a template for electrodeposition, but also as a nanoscopic wire to electrically connect the NPs (Figure 2.13b). Typical maps of surface activity obtained with SECCM are shown in Figure 2.13c. Comparing the activity maps with the AFM image shows there is an excellent correspondence between the electrocatalytically active regions and the location of the individual NPs. SECCM maps were obtained at various potentials, corresponding to surface oxidation processes as well the ORR and the HER. By measuring the potential-dependent electrocatalytic response of individual NPs and correlating it with the size and structure obtained with AFM and SEM, resulted in several notable findings. First, the reactivity of individual NPs was highly non-uniform, with subtle changes in NP size and shape leading to significant changes in activity. Furthermore, different NPs displayed different current-potential profiles, even though the average current over the total ensemble yielded an 'expected' potential-dependent current profile. In some cases, NPs that were active for the ORR showed no activity towards the HER. Finally, the study also demonstrated the very high sensitivity of this frontier technique, being able to measure currents of ca. 10 fA over a 40 ms measuring time, corresponding to the reduction of ~600 O₂ molecules (assuming a 4-electron transfer process).

A recent report demonstrates the ability of a combined AFM-SECM approach to measure electrochemistry at individual nanoparticles.[352] In their work, Demaille et al. dispersed Au NPs on a substrate covered with an alkanethiol SAM, and modified the NPs with a redox-labeled ferrocene-polyethylene glycole capping agent (Fc-PEG).

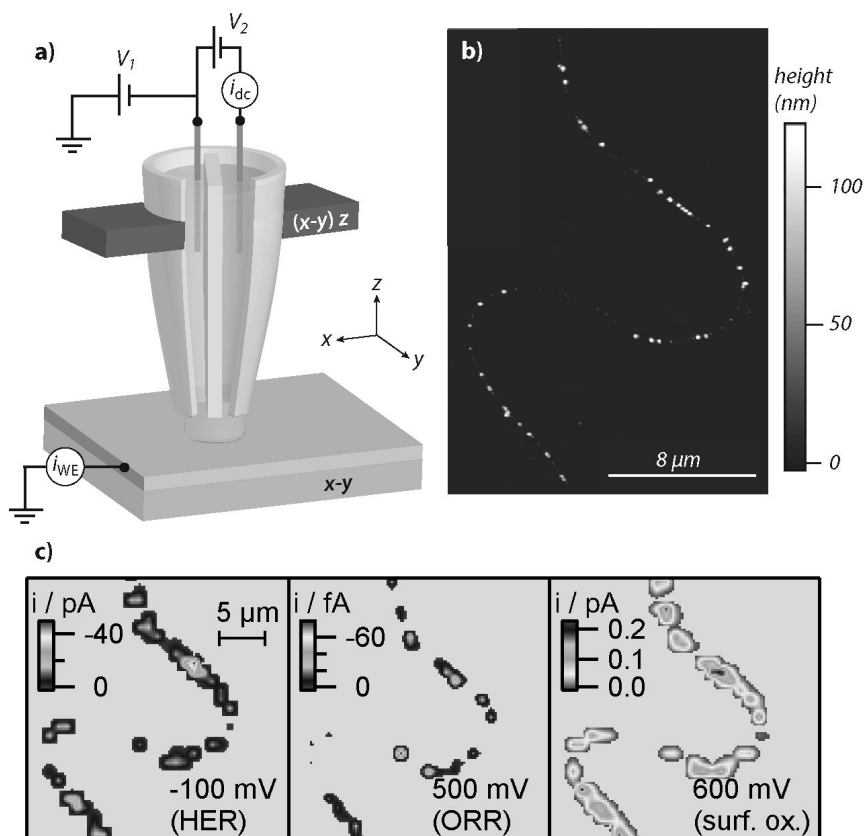


Figure 2.13: (a) Schematic of a scanning electrochemical cell microscopy (SECCM) set-up. Adapted from ref [297]. (b) AFM image of Pt NPs deposited on a single carbon nanotube. (c) SECCM images of the same area as panel (b) at -100 mV (HER), 500 mV (ORR) and 600 mV (surface oxidation) vs Pd-H_2 , respectively. Adapted from reference [111]. ©2011, American Chemical Society.

A conductive AFM tip of ~100 nm radius was used to turn over the redox-strands shrouding the NPs and measure the corresponding current response. A variance in NP activity was detected, as only about 80% of the NPs measured by AFM in topography mode generated a measurable SECM current. Demaille et al. attributed this to the unsuccessful grafting of the Fc-PEG at possibly contaminated NPs, as in a separate conductive AFM experiment they show that approximately 90% of the NPs were in fact electronically coupled to the substrate electrode. It should be noted that the SECM currents were rather small compared to the background signal and significant signal processing and digital filtering was needed to extract the SECM currents (~300 fA).

Another recent technique to study individual NPs within an array employs an optical method based on surface plasmon resonance (SPR).[353] SPR is rather sensitive to refractive index variations near a metal surface,[354] and refractive indexes change when reactants are converted at an electrode surface.[355] This method was applied to detect hydrogen evolution at an array of NPs. A CV was recorded on the entire ensemble while following localized changes in SPR, which could be related to single NPs. Apparent CVs for individual NPs could be reconstructed using the potential-dependent SPR changes of the NPs.[353] For 80 nm diameter Pt NPs, a wide variability from one NP to the next in the HER current was found at a potential of -0.2V vs RHE, which is similar to the changes in activity observed in the studies by Lai et al. highlighted above.[111]

Electrochemical strain microscopy is also emerging as an insightful technique for probing electrocatalytic activity on the nanoscale in certain environments. This technique can be used to detect catalytic effects of individual NPs in a model solid-oxide fuel cell environment.[356] In this study, a platinumized tip of an AFM was placed in contact with a surface that conducted oxygen ions (yttrium-stabilized zirconia; YSZ), in ambient air. A potential bias was then applied that resulted in the ORR/OER reaction at the tip, leading to a diffusion of oxygen vacancies in the YSZ lattice towards the surface. The movement of vacancies resulted in strain that could be detected by the probe as surface deformations on the pm level. When the tip was on or near a catalyst NP, the applied bias also affected the NP, resulting in enhanced ORR/OER. In this way, an electrochemical map was made of Pt nanoislands evaporated onto a YSZ support, using the ORR/OER system, on which the Pt areas had the highest ORR/OER activity. So far, due to the ultralocal nature of the probe (i.e. the tip is much smaller than the nanoparticles), no quantitative information regarding the shape and size dependence of the catalytic activity could be obtained, although these studies further highlight how local probes have considerable prospects for unraveling the activity of complex NP

electrocatalysts.

2.6 Conclusions and Outlook

In this chapter, we have highlighted and discussed recent reports on the electrochemistry of NPs, with particular attention given to electrocatalytic processes which are among the most widely studied. While a wide range of NP configurations has been considered, from extensive ensembles to individual NPs, the focus has been on studies which provide enhanced (quantitative) information on NP activity through investigations characterized by well-defined mass transport and/or making use of NPs of highly defined architecture, or where structure can be measured and related to activity at the single NP level.

Much progress has been made in controlling NP shape and size, particularly in the colloidal synthesis of NPs. Many different shapes can be made reliably and these shape-tailored NPs typically show electrocatalytic responses reminiscent of their dominant exposed surface facets in single crystal measurements. However, a majority of shape-controlled NPs are still very large compared to commercial catalyst NPs and therefore have sub-optimal mass activity. Additionally, the morphological stability has not been demonstrated sufficiently. For the possible application of such promising particles, it will be very interesting to see if the mass activity can be increased by decreasing the NP size, while retaining high NP stability

When NPs are used in electrocatalysis, it is of paramount importance that best practices are followed, with respect to immobilization, cleaning and characterization of the NPs on support electrodes. If these aspects are not properly considered, results obtained in different laboratories and experiments are difficult to compare. Additionally, when real catalysts are studied in model environments, this chapter has highlighted that it is essential to control mass transport and ohmic losses in order to understand the intrinsic behavior. Mass transport is also a very important consideration when studying model NP ensembles in model environments, particularly for reactions that have soluble intermediates that may re-adsorb on adjacent NPs, depending on the prevailing mass-transport rate and the inter-particle separation.

A major aspect of this chapter has been to highlight emerging frontier techniques that hold considerable promise for a breakthrough in understanding the fundamentals of NP electrocatalysis, through the study of individual NPs. This type of approach is particularly effective when the activity and structure can be determined and correlated at an individual NP. The main technical challenges are the spatial isolation of a

single NP and the measurement of the (often) very low electrochemical current generated at individual NPs. Three techniques were distinguished and discussed. First is the immobilization of individual particles on inert and ultrasensitive probes, such as by electrodeposition. The use of this approach to study the ORR revealed how NP size influenced electrocatalytic activity and the outcome (products) of electrochemical processes.

The second approach is the discretized detection of individual NPs using UMEs. In this case the UME and NP couple are chosen such that the UME is inert to the turnover of a reactant in solution, but it occurs when a NP in solution is polarized upon landing on an UME surface. Several UME/NP combinations have been reported based on this approach, indicating that the approach is quite universal. Recently, this approach has been expanded by coupling to other techniques, such as electron microscopy, to allow the direct correlation between structure and activity on a single NP level. Improved quantification and analysis of NP landings are necessary for the further application of this technique, particularly the formulation of more advanced models for NP transport to the support electrode and the interaction of NPs with electrodes.

A final method for elucidating the electrochemistry of individual NPs is the application of probes with a high spatial resolution, such as scanning nanoelectrodes, scanning droplet cells, or advanced optical measurements, to screen two-dimensional NP ensembles. These measurements have shown heterogeneity in the activity of NPs of apparently similar size, suggesting that minute shape changes can significantly affect the catalytic activity of NPs.

Electrochemical measurements of NPs have now reached a critical phase, in which it has become possible to reveal catalytic activity of NPs from complex membrane electrode assemblies to individual NPs in model environments. The breadth of techniques and the information they provide will aid in the rational design of optimal catalysts for many reactions and greatly advance our understanding of electrochemical processes at the nanoscale.

Bibliography

- [1] C. Q. Sun, B. K. Tay, X. T. Zeng, S. Li, T. P. Chen, J. Zhou, H. L. Bai and E. Y. Jiang, *J. Phys.: Condens. Matter*, 2002, **14**, 7781.
- [2] D. Zanchet, H. Tolentino, M. M. Alves, O. Alves and D. Ugarte, *Chem. Phys. Lett.*, 2000, **323**, 167–172.
- [3] A. N. Goldstein, C. M. Echer and A. P. Alivisatos, *Science*, 1992, **256**, 1425–1427.
- [4] M. Haruta, *Chem. Rec.*, 2003, **3**, 75–87.
- [5] M. T. M. Koper, *Nanoscale*, 2011, **3**, 2054–2073.
- [6] Y. Li, E. Boone and M. A. El-Sayed, *Langmuir*, 2002, **18**, 4921–4925.
- [7] S. Link and M. A. El-Sayed, *J. Phys. Chem. B*, 1999, **103**, 4212–4217.
- [8] H.-B. Fu and J.-N. Yao, *J. Am. Chem. Soc.*, 2001, **123**, 1434–1439.
- [9] B. Zhang, L. Fan, H. Zhong, Y. Liu and S. Chen, *J. Am. Chem. Soc.*, 2013, **135**, 10073–10080.
- [10] J. J. Watkins and H. S. White, *Langmuir*, 2004, **20**, 5474–5483.
- [11] C. P. Smith and H. S. White, *Anal. Chem.*, 1993, **65**, 3343–3353.
- [12] R. He, S. Chen, F. Yang and B. Wu, *J. Phys. Chem. B*, 2006, **110**, 3262–3270.
- [13] A. J. Bard, *J. Am. Chem. Soc.*, 2010, **132**, 7559–7567.
- [14] A. J. Arvia, R. C. Salvarezza and W. E. Triaca, *J. New Mater. Electrochem. Syst.*, 2004, **7**, 133–143.
- [15] F. Campbell and R. Compton, *Anal. Bioanal. Chem.*, 2010, **396**, 241–259.
- [16] D. Hernández-Santos, M. B. González-García and A. C. García, *Electroanalysis*, 2002, **14**, 1225–1235.
- [17] J. N. Anker, W. Paige Hall, O. Lyandres, N. C. Shah, J. Zhao and R. P. Van Duyne, *Nat. Mater.*, 2008, **7**, 442–453.
- [18] S. Nie and S. R. Emory, *Science*, 1997, **275**, 1102–1106.
- [19] K. Kneipp, H. Kneipp, I. Itzkan, R. R. Dasari and M. S. Feld, *Chem. Rev.*, 1999, **99**, 2957–2976.
- [20] R. Kitsomboonloha, C. Ngambenjawong, W. Mohammed, M. B. Chaudhari, G. L. Hornyak and J. Dutta, *Micro Nano Lett.*, 2011, **6**, 342–344.
- [21] Q. A. Pankhurst, J. Connolly, S. K. Jones and J. Dobson, *J. Phys. D: Appl. Phys.*, 2003, **36**, R167.
- [22] S. M. Moghimi, A. C. Hunter and J. C. Murray, *Pharmacol. Rev.*, 2001, **53**, 283–318.
- [23] B. D. Chithrani, A. A. Ghazani and W. C. W. Chan, *Nano Lett.*, 2006, **6**, 662–668.
- [24] G. Wertheim, in *Small Particles and Inorganic Clusters*, ed. C. Chapon, M. Gillet and C. Henry, Springer Berlin Heidelberg, 1989, pp. 319–326.
- [25] S. Proch, M. Wirth, H. S. White and S. L. Anderson, *J. Am. Chem. Soc.*, 2013, **135**, 3073–3086.
- [26] G. Somorjai and J. Park, *Top. Catal.*, 2008, **49**, 126–135.
- [27] G. Somorjai and Y. Li, *Introduction to Surface Chemistry and Catalysis*, Wiley & Sons, Hoboken, 2nd edn., 2010.
- [28] J. K. Nørskov, T. Bligaard, J. Rossmeisl and C. H. Christensen, *Nat Chem*, 2009, **1**, 37–46.
- [29] H. A. Gasteiger, S. S. Kocha, B. Sompalli and F. T. Wagner, *Appl. Catal., B*, 2005, **56**, 9–35.
- [30] F. Maillard, S. Pronkin and E. Savinova, *A Surface Science Approach*, Wiley, Hoboken, 2009.

- [31] R. W. Murray, *Chem. Rev.*, 2008, **108**, 2688–2720.
- [32] S. M. Oja, M. Wood and B. Zhang, *Anal. Chem.*, 2013, **85**, 473–486.
- [33] L. Rassaei, P. S. Singh and S. G. Lemay, *Anal. Chem.*, 2011, **83**, 3974–3980.
- [34] H. Zhang, M. Jin and Y. Xia, *Angew. Chem., Int. Ed.*, 2012, **51**, 7656–7673.
- [35] A. Chen and P. Holt-Hindle, *Chem. Rev.*, 2010, **110**, 3767–3804.
- [36] M. Schulze, A. Schneider and E. Gülzow, *J. Power Sources*, 2004, **127**, 213 – 221.
- [37] K. Mayrhofer, M. Arenz, B. Blizanac, V. Stamenkovic, P. Ross and N. Markovic, *Electrochim. Acta*, 2005, **50**, 5144 – 5154.
- [38] S. Chen and A. Kucernak, *J. Phys. Chem. B*, 2003, **107**, 8392–8402.
- [39] M. Debe, *Nature*, 2012, **486**, 43–51.
- [40] G. Girishkumar, B. McCloskey, A. C. Luntz, S. Swanson and W. Wilcke, *J. Phys. Chem. Lett.*, 2010, **1**, 2193–2203.
- [41] M. Armand and J. Tarascon, *Nature*, 2008, **451**, 652–657.
- [42] V. R. Stamenkovic, B. Fowler, B. S. Mun, G. Wang, P. N. Ross, C. A. Lucas and N. M. Markovic, *Science*, 2007, **315**, 493–497.
- [43] J. K. Nørskov, J. Rossmeisl, A. Logadottir, L. Lindqvist, J. R. Kitchin, T. Bligaard and H. Jónsson, *J. Phys. Chem. B*, 2004, **108**, 17886–17892.
- [44] P. N. Markovic, N. M. Ross Jr, *Surf. Sci. Rep.*, 2002, **45**, 117–229.
- [45] A. Kuzume, E. Herrero and J. M. Feliu, *J. Electroanal. Chem.*, 2007, **599**, 333–343.
- [46] I. E. L. Stephens, A. S. Bondarenko, U. Gronbjerg, J. Rossmeisl and I. Chorkendorff, *Energy Environ. Sci.*, 2012, **5**, 6744–6762.
- [47] M. Watanabe, H. Sei and P. Stonehart, *J. Electroanal. Chem. Interfac. Electrochem.*, 1989, **261**, 375–387.
- [48] Y. E. Seidel, A. Schneider, Z. Jusys, B. Wickman, B. Kasemo and R. J. Behm, *Faraday Discuss.*, 2009, **140**, 167–184.
- [49] S. Chen and A. Kucernak, *J. Phys. Chem. B*, 2004, **108**, 13984–13994.
- [50] A. U. Nilekar, K. Sasaki, C. A. Farberow, R. R. Adzic and M. Mavrikakis, *J. Am. Chem. Soc.*, 2011, **133**, 18574–18576.
- [51] S. M. M. Ehteshami and S. H. Chan, *Electrochim. Acta*, 2013, **93**, 334 – 345.
- [52] N. Brandon, S. Skinner and B. Steele, *Annu. Rev. Mater. Res.*, 2003, **33**, 183–213.
- [53] Y. Takasu, Y. Fujii, K. Yasuda, Y. Iwanaga and Y. Matsuda, *Electrochim. Acta*, 1989, **34**, 453 – 458.
- [54] J. Meier, K. A. Friedrich and U. Stimming, *Faraday Discuss.*, 2002, **121**, 365–372.
- [55] V. Rosca and M. T. M. Koper, *Electrochim. Acta*, 2008, **53**, 5199–5205.
- [56] B. Alvarez-Ruiz, R. Gomez, J. M. Orts and J. M. Feliu, *J. Electrochem. Soc.*, 2002, **149**, D35–D45.
- [57] B. E. Hayden, D. Pletcher and J.-P. Suchsland, *Angew. Chem., Int. Ed.*, 2007, **46**, 3530–3532.
- [58] B. E. Hayden, D. Pletcher, J.-P. Suchsland and L. J. Williams, *Phys. Chem. Chem. Phys.*, 2009, **11**, 1564–1570.
- [59] B. E. Hayden, D. Pletcher, J.-P. Suchsland and L. J. Williams, *Phys. Chem. Chem. Phys.*, 2009, **11**, 9141–9148.
- [60] M. Haruta, *Catal. Today*, 1997, **36**, 153 – 166.

- [61] C. T. Campbell, J. C. Sharp, Y. X. Yao, E. M. Karp and T. L. Silbaugh, *Faraday Discuss.*, 2011, **152**, 227–239.
- [62] C. Galeano, R. Güttel, M. Paul, P. Arnal, A.-H. Lu and F. Schüth, *Chem. Eur. J.*, 2011, **17**, 8434–8439.
- [63] A. S. K. Hashmi and G. J. Hutchings, *Angew. Chem., Int. Ed.*, 2006, **45**, 7896–7936.
- [64] R. L. McCreery, *Chem. Rev.*, 2008, **108**, 2646–2687.
- [65] L. M. Roen, C. H. Paik and T. D. Jarvi, *Electrochem. Solid-State Lett.*, 2004, **7**, A19–A22.
- [66] P. Serp, M. Corrias and P. Kalck, *Appl. Catal., A*, 2003, **253**, 337–358.
- [67] R. M. Crooks, M. Zhao, L. Sun, V. Chechik and L. K. Yeung, *Acc. Chem. Res.*, 2000, **34**, 181–190.
- [68] G. R. Salazar-Banda, K. I. Eguiluz and L. A. Avaca, *Electrochem. Commun.*, 2007, **9**, 59–64.
- [69] F. J. Vidal-Iglesias, J. Solla-Gullón, P. Rodríguez, E. Herrero, V. Montiel, J. M. Feliu and A. Aldaz, *Electrochem. Commun.*, 2004, **6**, 1080–1084.
- [70] J. Solla-Gullón, P. Rodríguez, E. Herrero, A. Aldaz and J. M. Feliu, *Phys. Chem. Chem. Phys.*, 2008, **10**, 1359–1373.
- [71] G. Sandmann, H. Dietz and W. Plieth, *J. Electroanal. Chem.*, 2000, **491**, 78–86.
- [72] C. Granqvist and A. Hultåker, *Thin Solid Films*, 2002, **411**, 1–5.
- [73] T. Minami, *Semicond. Sci. Technol.*, 2005, **20**, S35.
- [74] R. M. Penner, *J. Phys. Chem. B*, 2002, **106**, 3339–3353.
- [75] M. Bayati, J. M. Abad, R. J. Nichols and D. J. Schiffrin, *J. Phys. Chem. C*, 2010, **114**, 18439–18448.
- [76] B. Scharifker and G. Hills, *Electrochim. Acta*, 1983, **28**, 879–889.
- [77] J. V. Zoval, J. Lee, S. Gorer and R. M. Penner, *J. Phys. Chem. B*, 1998, **102**, 1166–1175.
- [78] H. V. Patten, E. Ventosa, A. Colina, V. Ruiz, J. López-Palacios, A. J. Wain, S. C. Lai, J. V. Macpherson and P. R. Unwin, *J. Solid State Electrochem.*, 2011, **15**, 2331–2339.
- [79] T. M. Day, P. R. Unwin and J. V. Macpherson, *Nano Lett.*, 2007, **7**, 51–57.
- [80] T. M. Day, P. R. Unwin, N. R. Wilson and J. V. Macpherson, *J. Am. Chem. Soc.*, 2005, **127**, 10639–10647.
- [81] B. M. Quinn, C. Dekker and S. G. Lemay, *J. Am. Chem. Soc.*, 2005, **127**, 6146–6147.
- [82] B. Quinn and S. Lemay, *Adv. Mater.*, 2006, **18**, 855–859.
- [83] C. C. Chen, C. S. C. Bose and K. Rajeshwar, *J. Electroanal. Chem.*, 1993, **350**, 161–176.
- [84] M. T. Giacomini, E. A. Ticianelli, J. McBreen and M. Balasubramanian, *J. Electrochem. Soc.*, 2001, **148**, A323–A329.
- [85] R. Schrebler, M. A. del Valle, H. Gómez, C. Veas and R. Córdova, *J. Electroanal. Chem.*, 1995, **380**, 219–227.
- [86] J.-H. Ye and P. S. Fedkiw, *Electrochim. Acta*, 1996, **41**, 221–231.
- [87] G. Kokkinidis, A. Papoutsis, D. Stoychev and A. Milchev, *J. Electroanal. Chem.*, 2000, **486**, 48–55.
- [88] P. Sun, F. Li, C. Yang, T. Sun, I. Kady, B. Hunt and J. Zhuang, *J. Phys. Chem. C*, 2013, **117**, 6120–6125.
- [89] H. Masuda, K. Yasui and K. Nishio, *Adv. Mater.*, 2000, **12**, 1031–1033.
- [90] A. R. Howells, L. Hung, G. S. Chottiner and D. A. Scherson, *Solid State Ionics*, 2002, **150**, 53–62.
- [91] K. L. Yeung and E. E. Wolf, *J. Vac. Sci. Technol., A*, 1992, **10**, 651–656.

- [92] C. R. Henry, *Surf. Sci. Rep.*, 1998, **31**, 235–325.
- [93] K. Yahikozawa, Y. Fujii, Y. Matsuda, K. Nishimura and Y. Takasu, *Electrochim. Acta*, 1991, **36**, 973–978.
- [94] N. Tian, Z.-Y. Zhou, S.-G. Sun, Y. Ding and Z. L. Wang, *Science*, 2007, **316**, 732–735.
- [95] J. Ustarroz, U. Gupta, A. Hubin, S. Bals and H. Terryn, *Electrochem. Commun.*, 2010, **12**, 1706–1709.
- [96] J. Ustarroz, J. A. Hammons, T. Altantzis, A. Hubin, S. Bals and H. Terryn, *J. Am. Chem. Soc.*, 2013, **Accepted**.
- [97] J. Ustarroz, X. Ke, A. Hubin, S. Bals and H. Terryn, *J. Phys. Chem. C*, 2012, **116**, 2322–2329.
- [98] M. J. Williamson, R. M. Tromp, P. M. Vereecken, R. Hull and F. M. Ross, *Nat. Mater.*, 2003, **2**, 532–536.
- [99] A. Radisic, P. M. Vereecken, J. B. Hannon, P. C. Searson and F. M. Ross, *Nano Lett.*, 2006, **6**, 238–242.
- [100] J. Ustarroz, J. A. Hammons, Y. Van Ingelgem, M. Tzedaki, A. Hubin and H. Terryn, *Electrochem. Commun.*, 2011, **13**, 1320–1323.
- [101] E. García-Pastoriza, J. Mostany and B. Scharifker, *J. Electroanal. Chem.*, 1998, **441**, 13 – 18.
- [102] P. V. Dudin, P. R. Unwin and J. V. Macpherson, *J. Phys. Chem. C*, 2010, **114**, 13241–13248.
- [103] P. L. Redmond, A. J. Hallock and L. E. Brus, *Nano Lett.*, 2005, **5**, 131–135.
- [104] H. Liu and R. M. Penner, *J. Phys. Chem. B*, 2000, **104**, 9131–9139.
- [105] H. Liu, F. Favier, K. Ng, M. P. Zach and R. M. Penner, *Electrochim. Acta*, 2001, **47**, 671–677.
- [106] W. Plieth, H. Dietz, G. Sandmann, A. Meixner, M. Weber, P. Moyer and J. Schmidt, *Electrochim. Acta*, 1999, **44**, 3659–3666.
- [107] M. Bayati, J. M. Abad, C. A. Bridges, M. J. Rosseinsky and D. J. Schiffrin, *J. Electroanal. Chem.*, 2008, **623**, 19–28.
- [108] T. Brülle, A. Denisenko, H. Sternschulte and U. Stimming, *Phys. Chem. Chem. Phys.*, 2011, **13**, 12883–12891.
- [109] T. Brülle, W. Ju, P. Niedermayr, A. Denisenko, O. Paschos, O. Schneider and U. Stimming, *Molecules*, 2011, **16**, 10059–10077.
- [110] M. P. Zach and R. M. Penner, *Adv. Mater.*, 2000, **12**, 878–883.
- [111] S. C. S. Lai, P. V. Dudin, J. V. Macpherson and P. R. Unwin, *J. Am. Chem. Soc.*, 2011, **133**, 10744–10747.
- [112] J. L. Fransaer and R. M. Penner, *J. Phys. Chem. B*, 1999, **103**, 7643–7653.
- [113] J. Dai and M. L. Bruening, *Nano Lett.*, 2002, **2**, 497–501.
- [114] S. Joly, R. Kane, L. Radzilowski, T. Wang, A. Wu, R. E. Cohen, E. L. Thomas and M. F. Rubner, *Langmuir*, 2000, **16**, 1354–1359.
- [115] S. Dante, Z. Hou, S. Risbud and P. Stroeve, *Langmuir*, 1999, **15**, 2176–2182.
- [116] X. Shi, M. Shen and H. Möhwald, *Prog. Polym. Sci.*, 2004, **29**, 987 – 1019.
- [117] X. Zhang and Z. Su, *Adv. Mater.*, 2012, **24**, 4574–4577.
- [118] P. Bertonecello, M. Peruffo and P. R. Unwin, *Chem. Commun.*, 2007, 1597–1599.
- [119] P. Allongue, M. Delamar, B. Desbat, O. Fagebaume, R. Hitmi, J. Pinson and J.-M. Savéant, *J. Am. Chem. Soc.*, 1997, **119**, 201–207.
- [120] M. Delamar, R. Hitmi, J. Pinson and J. M. Saveant, *J. Am. Chem. Soc.*, 1992, **114**, 5883–5884.

- [121] A. J. Downard, *Electroanalysis*, 2000, **12**, 1085–1096.
- [122] J. Pinson and F. Podvorica, *Chem. Soc. Rev.*, 2005, **34**, 429–439.
- [123] S. Mahouche-Chergui, S. Gam-Derouich, C. Mangeney and M. M. Chehimi, *Chem. Soc. Rev.*, 2011, **40**, 4143–4166.
- [124] M. M. Waje, X. Wang, W. Z. Li and Y. S. Yan, *Nanotechnology*, 2005, **16**, S395–S400.
- [125] D.-j. Guo and H.-I. Li, *Electrochem. Commun.*, 2004, **6**, 999–1003.
- [126] D. J. Guo and H. L. Li, *Carbon*, 2005, **43**, 1259 – 1264.
- [127] J. Turkevich, P. C. Stevenson and J. Hillier, *Discuss. Faraday Soc.*, 1951, **11**, 55–75.
- [128] M. Brust, M. Walker, D. Bethell, D. J. Schiffrin and R. Whyman, *J. Chem. Soc., Chem. Commun.*, 1994, 801–802.
- [129] B. L. Cushing, V. L. Kolesnichenko and C. J. O'Connor, *Chem. Rev.*, 2004, **104**, 3893–3946.
- [130] R. Van Hardeveld and F. Hartog, *Surf. Sci.*, 1969, **15**, 189–230.
- [131] Y. Xia, Y. Xiong, B. Lim and S. E. Skrabalak, *Angew. Chem., Int. Ed.*, 2009, **48**, 60–103.
- [132] T. K. Sau and A. L. Rogach, *Adv. Mater.*, 2009, **22**, 1781–1804.
- [133] K. Zhou and Y. Li, *Angew. Chem., Int. Ed.*, 2012, **51**, 602–613.
- [134] Y. Niu and R. M. Crooks, *C. R. Chim.*, 2003, **6**, 1049–1059.
- [135] F. Gröhn, B. J. Bauer, Y. A. Akpalu, C. L. Jackson and E. J. Amis, *Macromolecules*, 2000, **33**, 6042–6050.
- [136] K. Esumi, A. Suzuki, A. Yamahira and K. Torigoe, *Langmuir*, 2000, **16**, 2604–2608.
- [137] M. Zhao and R. M. Crooks, *Angew. Chem., Int. Ed.*, 1999, **38**, 364–366.
- [138] R. M. Crooks and M. Zhao, *Adv. Mater.*, 1999, **11**, 217–220.
- [139] M. Zhao, L. Sun and R. M. Crooks, *J. Am. Chem. Soc.*, 1998, **120**, 4877–4878.
- [140] R. W. J. Scott, O. M. Wilson and R. M. Crooks, *J. Phys. Chem. B*, 2005, **109**, 692–704.
- [141] F. Aulenta, W. Hayes and S. Rannard, *Eur. Polym. J.*, 2003, **39**, 1741 – 1771.
- [142] F. Vögtle, G. Richardt and N. Werner, in *Functional Dendrimers*, Wiley-VCH Verlag GmbH & Co. KGaA, 2009, ch. 3, pp. 49–79.
- [143] H. Ye and R. M. Crooks, *J. Am. Chem. Soc.*, 2005, **127**, 4930–4934.
- [144] A. I. Yanson, P. Rodriguez, N. Garcia-Araez, R. V. Mom, F. D. Tichelaar and M. T. M. Koper, *Angew. Chem., Int. Ed.*, 2011, **50**, 6346–6350.
- [145] P. Rodriguez, F. D. Tichelaar, M. T. M. Koper and A. I. Yanson, *J. Am. Chem. Soc.*, 2011, **133**, 17626–17629.
- [146] A. I. Yanson, P. V. Antonov, P. Rodriguez and M. T. M. Koper, *Electrochim. Acta*, 2013, **In press**.
- [147] A. I. Yanson, P. V. Antonov, Y. I. Yanson and M. T. M. Koper, *Electrochim. Acta*, 2013, **In press**.
- [148] R. D. Deegan, O. Bakajin, T. F. Dupont, G. Huber, S. R. Nagel and T. A. Witten, *Nature*, 1997, **389**, 827–829.
- [149] T. A. H. Nguyen, M. A. Hampton and A. V. Nguyen, *J. Phys. Chem. C*, 2013, **117**, 4707–4716.
- [150] M. A. Hampton, T. A. Nguyen, A. V. Nguyen, Z. P. Xu, L. Huang and V. Rudolph, *J. Colloid Interface Sci.*, 2012, **377**, 456 – 462.

- [151] R. G. Freeman, K. C. Grabar, K. J. Allison, R. M. Bright, J. A. Davis, A. P. Guthrie, M. B. Hommer, M. A. Jackson, P. C. Smith, D. G. Walter and M. J. Natan, *Science*, 1995, **267**, 1629–1632.
- [152] W. Cheng, S. Dong and E. Wang, *Angew. Chem., Int. Ed.*, 2003, **42**, 449–452.
- [153] W. Cheng, S. Dong and E. Wang, *J. Phys. Chem. B*, 2004, **108**, 19146–19154.
- [154] Y. Li, J. T. Cox and B. Zhang, *J. Am. Chem. Soc.*, 2010, **132**, 3047–3054.
- [155] T. Zhu, X. Fu, T. Mu, J. Wang and Z. Liu, *Langmuir*, 1999, **15**, 5197–5199.
- [156] C. A. Goss, D. H. Charych and M. Majda, *Anal. Chem.*, 1991, **63**, 85–88.
- [157] Y. Tang and W. Cheng, *Langmuir*, 2013, **29**, 3125–3132.
- [158] K. C. Grabar, K. J. Allison, B. E. Baker, R. M. Bright, K. R. Brown, R. G. Freeman, A. P. Fox, C. D. Keating, M. D. Musick and M. J. Natan, *Langmuir*, 1996, **12**, 2353–2361.
- [159] K. C. Grabar, P. C. Smith, M. D. Musick, J. A. Davis, D. G. Walter, M. A. Jackson, A. P. Guthrie and M. J. Natan, *J. Am. Chem. Soc.*, 1996, **118**, 1148–1153.
- [160] W. Cheng, S. Dong and E. Wang, *Langmuir*, 2002, **18**, 9947–9952.
- [161] S. L. Horswell, I. A. O’Nei and D. J. Schiffrin, *J. Phys. Chem. B*, 2003, **107**, 4844–4854.
- [162] B. K. Jena, S. J. Percival and B. Zhang, *Anal. Chem.*, 2010, **82**, 6737–6743.
- [163] D. Bethell, M. Brust, D. J. Schiffrin and C. Kiely, *J. Electroanal. Chem.*, 1996, **409**, 137–143.
- [164] M. Brust, D. Bethell, C. J. Kiely and D. J. Schiffrin, *Langmuir*, 1998, **14**, 5425–5429.
- [165] C. R. Bradbury, J. Zhao and D. J. Fermín, *J. Phys. Chem. C*, 2008, **112**, 10153–10160.
- [166] J. Zhao, C. R. Bradbury and D. J. Fermín, *J. Phys. Chem. C*, 2008, **112**, 6832–6841.
- [167] J. B. Shein, L. M. H. Lai, P. K. Eggers, M. N. Paddon-Row and J. J. Gooding, *Langmuir*, 2009, **25**, 11121–11128.
- [168] J. Guo, C.-N. Ho and P. Sun, *Electroanal.*, 2011, **23**, 481–486.
- [169] D. K. Schwartz, *Annu. Rev. Phys. Chem.*, 2001, **52**, 107–137.
- [170] J. J. Gooding, F. Mearns, W. Yang and J. Liu, *Electroanalysis*, 2003, **15**, 81–96.
- [171] A. Ulman, *Chem. Rev.*, 1996, **96**, 1533–1554.
- [172] J. C. Love, L. A. Estroff, J. K. Kriebel, R. G. Nuzzo and G. M. Whitesides, *Chem. Rev.*, 2005, **105**, 1103–1170.
- [173] F. Schreiber, *Prog. Surf. Sci.*, 2000, **65**, 151–257.
- [174] G. Le Saux, S. Ciampi, K. Gaus and J. J. Gooding, *ACS Appl. Mater. Interfaces*, 2009, **1**, 2477–2483.
- [175] M.-C. Chuang and J.-a. Ho, *RSC Advances*, 2012, **2**, 4092–4096.
- [176] D. M. Adams, L. Brus, C. E. D. Chidsey, S. Creager, C. Creutz, C. R. Kagan, P. V. Kamat, M. Lieberman, S. Lindsay, R. A. Marcus, R. M. Metzger, M. E. Michel-Beyerle, J. R. Miller, M. D. Newton, D. R. Rolison, O. Sankey, K. S. Schanze, J. Yardley and X. Zhu, *J. Phys. Chem. B*, 2003, **107**, 6668–6697.
- [177] A. Chou, P. K. Eggers, M. N. Paddon-Row and J. J. Gooding, *J. Phys. Chem. C*, 2009, **113**, 3203–3211.
- [178] M. N. Paddon-Row, *Acc. Chem. Res.*, 1994, **27**, 18–25.
- [179] D. J. Wold and C. D. Frisbie, *J. Am. Chem. Soc.*, 2001, **123**, 5549–5556.
- [180] A. Barfidokht, S. Ciampi, E. Luis, N. Darwish and J. J. Gooding, *Anal. Chem.*, 2012, **85**, 1073–1080.
- [181] W. Cheng, S. Dong and E. Wang, *Anal. Chem.*, 2002, **74**, 3599–3604.

- [182] J. Zhao, M. Wasem, C. R. Bradbury and D. J. Fermín, *J. Phys. Chem. C*, 2008, **112**, 7284–7289.
- [183] J. N. Chazalviel and P. Allongue, *J. Am. Chem. Soc.*, 2011, **133**, 762–4.
- [184] J. N. Kuhn, C.-K. Tsung, W. Huang and G. A. Somorjai, *J. Catal.*, 2009, **265**, 209–215.
- [185] J. Solla-Gullón, V. Montiel, A. Aldaz and J. Clavilier, *J. Electroanal. Chem.*, 2000, **491**, 69–77.
- [186] H.-X. Zhang, H. Wang, Y.-S. Re and W.-B. Cai, *Chem. Commun.*, 2012, **48**, 8362–8364.
- [187] J. Monzo, M. T. M. Koper and P. Rodriguez, *ChemPhysChem*, 2012, **13**, 709–715.
- [188] F. J. Vidal-Iglesias, J. Solla-Gullón, E. Herrero, V. Montiel, A. Aldaz and J. M. Feliu, *Electrochem. Commun.*, 2011, **13**, 502–505.
- [189] C. Aliaga, J. Y. Park, Y. Yamada, H. S. Lee, C.-K. Tsung, P. Yang and G. A. Somorjai, *J. Phys. Chem. C*, 2009, **113**, 6150–6155.
- [190] J. Clavilier, R. Faure, G. Guinet and R. Durand, *J. Electroanal. Chem. Interfac. Electrochem.*, 1979, **107**, 205–209.
- [191] J. Clavilier and D. Armand, *J. Electroanal. Chem. Interfac. Electrochem.*, 1986, **199**, 187–200.
- [192] S. Trasatti and O. Petrii, *Pure Appl. Chem.*, 1991, **63**, 711–734.
- [193] F. J. Vidal-Iglesias, R. M. Aran-Ais, J. Solla-Gullon, E. Herrero and J. M. Feliu, *ACS Catal.*, 2012, **2**, 901–910.
- [194] J. Hernández, J. Solla-Gullón, E. Herrero, A. Aldaz and J. M. Feliu, *J. Phys. Chem. C*, 2007, **111**, 14078–14083.
- [195] C. L. Green and A. Kucernak, *J. Phys. Chem. B*, 2002, **106**, 1036–1047.
- [196] K. J. J. Mayrhofer, D. Strmcnik, B. B. Blizanac, V. Stamenkovic, M. Arenz and N. M. Markovic, *Electrochim. Acta*, 2008, **53**, 3181–3188.
- [197] P. Ochal, J. L. G. de la Fuente, M. Tsypkin, F. Seland, S. Sunde, N. Muthuswamy, M. Rønning, D. Chen, S. Garcia, S. Alayoglu and B. Eichhorn, *J. Electroanal. Chem.*, 2011, **655**, 140 – 146.
- [198] T. Vidaković, M. Christov and K. Sundmacher, *Electrochim. Acta*, 2007, **52**, 5606 – 5613.
- [199] T. Housmans, J. Feliu and M. Koper, *J. Electroanal. Chem.*, 2004, **572**, 79 – 91.
- [200] J. Grobely, F. W. DelRio, N. Pradeep, D.-I. Kim, V. A. Hackley and R. F. Cook, in *Methods in Molecular Biology*, ed. J. Walker, Springer, Heidelberg, 2009, vol. 697, pp. 71–82.
- [201] H. Borchert, E. V. Shevchenko, A. Robert, I. Mekis, A. Kornowski, G. Gruebel and H. Weller, *Langmuir*, 2005, **21**, 1931–1936.
- [202] X. Liu, Q. Dai, L. Austin, J. Coutts, G. Knowles, J. Zou, H. Chen and Q. A. Huo, *J. Am. Chem. Soc.*, 2008, **130**, 2780–2782.
- [203] V. Filipe, A. Hawe and W. Jiskoot, *Pharm. Res.*, 2010, **27**, 796–810.
- [204] M. Kerker, *The Scattering of Light and other electromagnetic radiation*, Academic Press, London, 1969.
- [205] V. Amendola, S. Polizzi and M. Meneghetti, *Langmuir*, 2007, **23**, 6766–6770.
- [206] V. Amendola and M. Meneghetti, *J. Mater. Chem.*, 2007, **17**, 4705–4710.
- [207] Z. L. Wang, *J. Phys. Chem. B*, 2000, **104**, 1153–1175.
- [208] Y. E. Seidel, Z. Jusys, B. Wickman, B. Kasemo and R. J. Behm, *ECS Trans.*, 2010, **25**, 91–102.
- [209] M. C. Henstridge and R. G. Compton, *Chem. Rec.*, 2012, **12**, 63–71.
- [210] J. Guo and E. Lindner, *Anal. Chem.*, 2009, **81**, 130–138.

- [211] N. C. Rudd, S. Cannan, E. Bitziou, I. Ciani, A. L. Whitworth and P. R. Unwin, *Anal. Chem.*, 2005, **77**, 6205–6217.
- [212] M. Gustavsson, H. Fredriksson, B. Kasemo, Z. Jusys, J. Kaiser, C. Jun and R. J. Behm, *J. Electroanal. Chem.*, 2004, **568**, 371–377.
- [213] R. G. Compton and P. R. Unwin, *J. Electroanal. Chem. Interfac. Electrochem.*, 1986, **205**, 1 – 20.
- [214] Y. E. Seidel, A. Schneider, Z. Jusys, B. Wickman, B. Kasemo and R. J. Behm, *Langmuir*, 2009, **26**, 3569–3578.
- [215] I. Dumitrescu, D. F. Yancey and R. M. Crooks, *Lab Chip*, 2012, **12**, 986–993.
- [216] I. Dumitrescu and R. M. Crooks, *Proc. Natl. Acad. Sci. U.S.A.*, 2012, **109**, 11493–11497.
- [217] S. Amemiya, A. J. Bard, F.-R. F. Fan, M. V. Mirkin and P. R. Unwin, *Annu. Rev. Anal. Chem.*, 2008, **1**, 95–131.
- [218] S. C. Lai, J. V. Macpherson and P. R. Unwin, *MRS Bull.*, 2012, **37**, 668–674.
- [219] J. L. Fernández, D. A. Walsh and A. J. Bard, *J. Am. Chem. Soc.*, 2004, **127**, 357–365.
- [220] S. Jayaraman and A. C. Hillier, *J. Phys. Chem. B*, 2003, **107**, 5221–5230.
- [221] A. Minguzzi, M. A. Alpuche-Aviles, J. R. López, S. Rondinini and A. J. Bard, *Anal. Chem.*, 2008, **80**, 4055–4064.
- [222] C. M. Sánchez-Sánchez and A. J. Bard, *Anal. Chem.*, 2009, **81**, 8094–8100.
- [223] G. Lu, J. S. Cooper and P. J. McGinn, *J. Power Sources*, 2006, **161**, 106 – 114.
- [224] M. V. Mirkin, W. Nogala, J. Velmurugan and Y. Wang, *Phys. Chem. Chem. Phys.*, 2011, **13**, 21196–21212.
- [225] J. Zhang, R. M. Lahtinen, K. Kontturi, P. R. Unwin and D. J. Schiffrin, *Chem. Commun.*, 2001, 1818–1819.
- [226] F. Li, I. Ciani, P. Bertoncello, P. R. Unwin, J. Zhao, C. R. Bradbury and D. J. Fermin, *J. Phys. Chem. C*, 2008, **112**, 9686–9694.
- [227] B. E. Hayden, *Acc. Chem. Res.*, 2013.
- [228] S. Guerin and B. E. Hayden, *J. Comb. Chem.*, 2006, **8**, 66–73.
- [229] S. Guerin, B. E. Hayden, D. Pletcher, M. E. Rendall, J.-P. Suchsland and L. J. Williams, *J. Comb. Chem.*, 2006, **8**, 791–798.
- [230] J. C. Meier, I. Katsounaros, C. Galeano, H. J. Bongard, A. A. Topalov, A. Kostka, A. Karschin, F. Schuth and K. J. J. Mayrhofer, *Energy Environ. Sci.*, 2012, **5**, 9319–9330.
- [231] K. J. Mayrhofer, J. C. Meier, S. J. Ashton, G. K. Wiberg, F. Kraus, M. Hanzlik and M. Arenz, *Electrochem. Commun.*, 2008, **10**, 1144 – 1147.
- [232] H. L. Xin, J. A. Mundy, Z. Liu, R. Cabezas, R. Hovden, L. F. Kourkoutis, J. Zhang, N. P. Subramanian, R. Makharia, F. T. Wagner and D. A. Muller, *Nano Lett.*, 2012, **12**, 490–497.
- [233] Y. Yu, H. L. Xin, R. Hovden, D. Wang, E. D. Rus, J. A. Mundy, D. A. Muller and H. D. Abruña, *Nano Lett.*, 2012, **12**, 4417–4423.
- [234] E. Endoh, S. Terazono, H. Widjaja and Y. Takimoto, *Electrochem. Solid-State Lett.*, 2004, **7**, A209–A211.
- [235] A. Taniguchi, T. Akita, K. Yasuda and Y. Miyazaki, *J. Power Sources*, 2004, **130**, 42 – 49.
- [236] T. S. Ahmadi, Z. L. Wang, T. C. Green, A. Henglein and M. A. El-Sayed, *Science*, 1996, **272**, 1924–1926.
- [237] T. S. Ahmadi, Z. L. Wang, A. Henglein and M. A. El-Sayed, *Chem. Mater.*, 1996, **8**, 1161.
- [238] M. Chen, B. Wu, J. Yang and N. Zheng, *Adv. Mater.*, 2012, **24**, 862–879.

- [239] C. Burda, X. Chen, R. Narayanan and M. A. El-Sayed, *Chem. Rev.*, 2005, **105**, 1025–1102.
- [240] R. Narayanan and M. A. El-Sayed, *J. Phys. Chem. B*, 2005, **109**, 12663–12676.
- [241] M. Grzelczak, J. Perez-Juste, P. Mulvaney and L. M. Liz-Marzan, *Chem. Soc. Rev.*, 2008, **37**, 1783–1791.
- [242] S. Guo and E. Wang, *Nano Today*, 2011, **6**, 240–264.
- [243] A. R. Tao, S. Habas and P. D. Yang, *Small*, 2008, **4**, 310–325.
- [244] Z. M. Peng and H. Yang, *Nano Today*, 2009, **4**, 143–164.
- [245] F. J. Vidal-Iglesias, N. Garcia-Ar ez, V. Montiel, J. M. Feliu and A. Aldaz, *Electrochem. Commun.*, 2003, **5**, 22–26.
- [246] F. J. Vidal-Iglesias, R. M. Aran-Ais, J. Solla-Gullon, E. Garnier, E. Herrero, A. Aldaz and J. M. Feliu, *Phys. Chem. Chem. Phys.*, 2012, **14**, 10258–10265.
- [247] V. Grozovski, J. Solla-Gullon, V. Climent, E. Herrero and J. M. Feliu, *J. Phys. Chem. C*, 2010, **114**, 13802–13812.
- [248] C. Wang, H. Daimon, Y. Lee, J. Kim and S. Sun, *J. Am. Chem. Soc.*, 2007, **129**, 6974–6975.
- [249] Y. Kang, M. Li, Y. Cai, M. Cargnello, R. E. Diaz, T. R. Gordon, N. L. Wieder, R. R. Adzic, R. J. Gorte, E. A. Stach and C. B. Murray, *J. Am. Chem. Soc.*, 2013, **135**, 2741–2747.
- [250] L. Lu, G. Yin, Z. Wang and Y. Gao, *Electrochem. Commun.*, 2009, **11**, 1596–1598.
- [251] C. Wang, H. Daimon, T. Onodera, T. Koda and S. Sun, *Angew. Chem., Int. Ed.*, 2008, **47**, 3588–3591.
- [252] M. Rodr guez-L pez, J. Solla-Gull n, E. Herrero, P. Tu n n, J. M. Feliu, A. Aldaz and A. Carrasquillo, *J. Am. Chem. Soc.*, 2010, **132**, 2233–2242.
- [253] C. M. S nchez-S nchez, F. J. Vidal-Iglesias, J. Solla-Gull n, V. Montiel, A. Aldaz, J. M. Feliu and E. Herrero, *Electrochim. Acta*, 2010, **55**, 8252–8257.
- [254] V. Bansal, V. Li, A. P. O'Mullane and S. K. Bhargava, *CrystEngComm*, 2010, **12**, 4280–4286.
- [255] M. Duca, P. Rodriguez, A. I. Yanson and M. T. M. Koper, *Top. Catal.*, 2013, **Accepted**.
- [256] Z.-Y. Zhou, N. Tian, J.-T. Li, I. Broadwell and S.-G. Sun, *Chem. Soc. Rev.*, 2011, **40**, 4167–4185.
- [257] Y. Ding, Y. Gao, Z. L. Wang, N. Tian, Z. Y. Zhou and S. G. Sun, *Appl. Phys. Lett.*, 2007, **91**, 121901.
- [258] Z.-Y. Zhou, Z.-Z. Huang, D.-J. Chen, Q. Wang, N. Tian and S.-G. Sun, *Angew. Chem., Int. Ed.*, 2010, **49**, 411–414.
- [259] Y.-J. Deng, N. Tian, Z.-Y. Zhou, R. Huang, Z.-L. Liu, J. Xiao and S.-G. Sun, *Chem. Sci.*, 2012, **3**, 1157–1161.
- [260] N. Tian, Z.-Y. Zhou, N.-F. Yu, L.-Y. Wang and S.-G. Sun, *J. Am. Chem. Soc.*, 2010, **132**, 7580–7581.
- [261] Z.-Y. Zhou, S.-J. Shang, N. Tian, B.-H. Wu, N.-F. Zheng, B.-B. Xu, C. Chen, H.-H. Wang, D.-M. Xiang and S.-G. Sun, *Electrochem. Commun.*, 2012, **22**, 61–64.
- [262] N. Tian, J. Xiao, Z.-Y. Zhou, H.-X. Liu, Y.-J. Deng, L. Huang, B.-B. Xu and S.-G. Sun, *Faraday Discuss.*, 2013, **162**, 77–89.
- [263] Z. Y. Zhou, N. Tian, Z. Z. Huang, D. J. Chen and S. G. Sun, *Faraday Discuss.*, 2008, **140**, 81–92.
- [264] N. Tian, Z.-Y. Zhou and S.-G. Sun, *Chem. Commun.*, 2009, **0**, 1502–1504.
- [265] Q. Cheng, Y.-X. Jiang, N. Tian, Z.-Y. Zhou and S.-G. Sun, *Electrochim. Acta*, 2010, **55**, 8273–8279.
- [266] Y.-X. Chen, S.-P. Chen, Z.-Y. Zhou, N. Tian, Y.-X. Jiang, S.-G. Sun, Y. Ding and Z. L. Wang, *J. Am. Chem. Soc.*, 2009, **131**, 10860.

- [267] Q.-S. Chen, Z.-Y. Zhou, F. J. Vidal-Iglesias, J. Solla-Gullón, J. M. Feliu and S.-G. Sun, *J. Am. Chem. Soc.*, 2011, **133**, 12930–12933.
- [268] H.-X. Liu, N. Tian, M. P. Brandon, J. Pei, Z.-C. Huangfu, C. Zhan, Z.-Y. Zhou, C. Hardacre, W.-F. Lin and S.-G. Sun, *Phys. Chem. Chem. Phys.*, 2012, **14**, 16415–16423.
- [269] H.-X. Liu, N. Tian, M. P. Brandon, Z.-Y. Zhou, J.-L. Lin, C. Hardacre, W.-F. Lin and S.-G. Sun, *ACS Catal.*, 2012, **2**, 708–715.
- [270] R. Huang, Y.-H. Wen, Z.-Z. Zhu and S.-G. Sun, *J. Mater. Chem.*, 2011, **21**, 11578–11584.
- [271] Y. Wen, H. Fang, Z. Zhu and S. Sun, *Phys. Lett. A*, 2009, **373**, 272–276.
- [272] Y.-H. Wen, H. Fang, Z.-Z. Zhu and S.-G. Sun, *Chem. Phys. Lett.*, 2009, **471**, 295–299.
- [273] S. Cherevko, A. A. Topalov, I. Katsounaros and K. J. Mayrhofer, *Electrochem. Commun.*, 2013, **28**, 44–46.
- [274] A. A. Topalov, I. Katsounaros, M. Auinger, S. Cherevko, J. C. Meier, S. O. Klemm and K. J. J. Mayrhofer, *Angew. Chem., Int. Ed.*, 2012, **51**, 12613–12615.
- [275] J. T. Cox and B. Zhang, *Annual Review of Analytical Chemistry*, 2012, **5**, 253–272.
- [276] C. J. Slevin, N. J. Gray, J. V. Macpherson, M. A. Webb and P. R. Unwin, *Electrochem. Commun.*, 1999, **1**, 282–288.
- [277] J. L. Conyers and H. S. White, *Anal. Chem.*, 2000, **72**, 4441–4446.
- [278] P. Sun and M. V. Mirkin, *Anal. Chem.*, 2006, **78**, 6526–6534.
- [279] R. M. Penner, M. J. Heben, T. L. Longin and N. S. Lewis, *Science*, 1990, **250**, 1118–1121.
- [280] G. P. Kittlesen, H. S. White and M. S. Wrighton, *J. Am. Chem. Soc.*, 1984, **106**, 7389–7396.
- [281] O. Ordeig, C. E. Banks, T. J. Davies, J. del Campo, R. Mas, F. X. Munoz and R. G. Compton, *Analyst*, 2006, **131**, 440–445.
- [282] S. E. F. Kleijn, A. I. Yanson and M. T. M. Koper, *J. Electroanal. Chem.*, 2012, **666**, 19–24.
- [283] F. J. M. Hoebein, F. S. Meijer, C. Dekker, S. P. J. Albracht, H. A. Heering and S. G. Lemay, *ACS Nano*, 2008, **2**, 2497–2504.
- [284] D. Krapf, M.-Y. Wu, R. M. M. Smeets, H. W. Zandbergen, C. Dekker and S. G. Lemay, *Nano Lett.*, 2005, **6**, 105–109.
- [285] G. Mészáros, C. Li, I. Pobelov and T. Wandlowski, *Nanotechnology*, 2007, **18**, 424004.
- [286] G. Mészáros, S. Kronholz, S. Karthäuser, D. Mayer and T. Wandlowski, *Appl. Phys. A: Mater. Sci. Process.*, 2007, **87**, 569–575.
- [287] N. Ebejer, M. Schnippering, A. W. Colburn, M. A. Edwards and P. R. Unwin, *Anal. Chem.*, 2010, **82**, 9141–9145.
- [288] M. E. Snowden, A. G. Güell, S. C. S. Lai, K. McKelvey, N. Ebejer, M. A. O'Connell, A. W. Colburn and P. R. Unwin, *Anal. Chem.*, 2012, **84**, 2483–2491.
- [289] A. G. Güell, N. Ebejer, M. E. Snowden, K. McKelvey, J. V. Macpherson and P. R. Unwin, *Proc. Natl. Acad. Sci. USA*, 2012.
- [290] A. G. Güell, N. Ebejer, M. E. Snowden, J. V. Macpherson and P. R. Unwin, *J. Am. Chem. Soc.*, 2012, **134**, 7258–7261.
- [291] S. C. S. Lai, A. N. Patel, K. McKelvey and P. R. Unwin, *Angew. Chem., Int. Ed.*, 2012, **51**, 5405–5408.
- [292] H. V. Patten, S. C. S. Lai, J. V. Macpherson and P. R. Unwin, *Anal. Chem.*, 2012, **84**, 5427–5432.
- [293] S. E. F. Kleijn, S. C. S. Lai, T. S. Miller, A. I. Yanson, M. T. M. Koper and P. R. Unwin, *J. Am. Chem. Soc.*, 2012, **134**, 18558–18561.

- [294] A. N. Patel, K. McKelvey and P. R. Unwin, *J. Am. Chem. Soc.*, 2012, **134**, 20246–20249.
- [295] A. N. Patel, M. G. Collignon, M. A. O’Connell, W. O. Y. Hung, K. McKelvey, J. V. Macpherson and P. R. Unwin, *J. Am. Chem. Soc.*, 2012, **134**, 20117–20130.
- [296] B. D. B. Aaronson, C.-H. Chen, H. Li, M. T. M. Koper, S. C. S. Lai and P. R. Unwin, *J. Am. Chem. Soc.*, 2013, **135**, 3873–3880.
- [297] N. Ebejer, A. G. Güell, S. C. Lai, K. McKelvey, M. E. Snowden and P. R. Unwin, *Annual Review of Analytical Chemistry*, 2013, **6**, 329–351.
- [298] M. Lohrengel, A. Moehring and M. Pilaski, *Electrochim. Acta*, 2001, **47**, 137 – 141.
- [299] C. G. Williams, M. A. Edwards, A. L. Colley, J. V. Macpherson and P. R. Unwin, *Anal. Chem.*, 2009, **81**, 2486–2495.
- [300] T. Suter and H. Böhni, *Electrochim. Acta*, 1997, **42**, 3275 – 3280.
- [301] J. W. Schultze, M. Pilaski, M. M. Lohrengel and U. König, *Faraday Discuss.*, 2002, **121**, 211–227.
- [302] F. Cortes-Salazar, A. Lesch, D. Momotenko, J.-M. Busnel, G. Wittstock and H. H. Girault, *Anal. Methods*, 2010, **2**, 817–823.
- [303] M. Carminati, G. Ferrari, D. Bianchi and M. Sampietro, *Electrochim. Acta*, 2013.
- [304] J. J. Watkins, J. Chen, H. S. White, H. D. Abruña, E. Maisonhaute and C. Amatore, *Anal. Chem.*, 2003, **75**, 3962–3971.
- [305] A. J. Bard and L. R. Faulkner, *Electrochemical Methods, Fundamentals and Applications*, John Wiley & Sons, New York, 2nd edn., 2001.
- [306] X. Xiao and A. J. Bard, *J. Am. Chem. Soc.*, 2007, **129**, 9610.
- [307] S. Chen and A. Kucernak, *Electrochem. Commun.*, 2002, **4**, 80–85.
- [308] S. Chen and A. Kucernak, *J. Phys. Chem. B*, 2004, **108**, 3262–3276.
- [309] R. Tel-Vered and A. J. Bard, *J. Phys. Chem. B*, 2006, **110**, 25279–25287.
- [310] J. Lakubub, A. Pouliwe, A. Kamasah, C. Yang and P. Sun, *Electroanalysis*, 2011, **23**, 2270–2274.
- [311] N. Nioradze, R. Chen, J. Kim, M. Shen, P. Santhosh and S. Amemiya, *Anal. Chem.*, 2013, **85**, 6198–6202.
- [312] R. A. Lazenby, K. McKelvey and P. R. Unwin, *Anal. Chem.*, 2013, **85**, 2937–2944.
- [313] W. Nogala, J. Velmurugan and M. V. Mirkin, *Anal. Chem.*, 2012, **84**, 5192–5197.
- [314] K. McKelvey, B. P. Nadappuram, P. Actis, Y. Takahashi, Y. E. Korchev, T. Matsue, C. Robinson and P. R. Unwin, *Anal. Chem.*, 2013, **85**, 7519–7526.
- [315] B. Zhang, J. Galusha, P. G. Shiozawa, G. Wang, A. J. Bergren, R. M. Jones, R. J. White, E. N. Ervin, C. C. Cauley and H. S. White, *Anal. Chem.*, 2007, **79**, 4778–4787.
- [316] J. Meier, J. Schiotz, P. Liu, J. K. Nørskov and U. Stimming, *Chem. Phys. Lett.*, 2004, **390**, 440–444.
- [317] General-Discussion, *Faraday Discuss.*, 2002, **121**, 97–127.
- [318] M. Heyrovsky, J. Jirkovsky and M. Struplova-Bartackova, *Langmuir*, 1995, **11**, 4300–4308.
- [319] M. Heyrovsky, J. Jirkovsky and M. Struplova-Bartackova, *Langmuir*, 1995, **11**, 4309–4312.
- [320] M. Heyrovsky, J. Jirkovsky and B. R. Mueller, *Langmuir*, 1995, **11**, 4293–4299.
- [321] M. Heyrovsky and J. Jirkovsky, *Langmuir*, 1995, **11**, 4288–4292.
- [322] A. V. Korshunov and M. Heyrovský, *Electroanalysis*, 2006, **18**, 423–426.
- [323] B. M. Quinn, P. G. van ’t Ho and S. G. Lemay, *J. Am. Chem. Soc.*, 2004, **126**, 8360–8361.

- [324] S. E. Fosdick, M. J. Anderson, E. G. Nettleton and R. M. Crooks, *J. Am. Chem. Soc.*, 2013, **135**, 5994–5997.
- [325] X. Xiao, F.-R. F. Fan, J. Zhou and A. J. Bard, *J. Am. Chem. Soc.*, 2008, **130**, 16669–16677.
- [326] X. Xiao, S. Pan, J. S. Jang, F.-R. F. Fan and A. J. Bard, *J. Phys. Chem. C*, 2009, **113**, 14978–14982.
- [327] S. E. F. Kleijn, B. Serrano-Bou, A. I. Yanson and M. T. M. Koper, *Langmuir*, 2013, **29**, 2054–2064.
- [328] R. Dasari, D. A. Robinson and K. J. Stevenson, *J. Am. Chem. Soc.*, 2013, **135**, 570–573.
- [329] P. V. Dudin, P. R. Unwin and J. V. Macpherson, *Phys. Chem. Chem. Phys.*, 2011, **13**, 17146–17152.
- [330] L. Aldous and R. G. Compton, *Phys. Chem. Chem. Phys.*, 2011, **13**, 5279–5287.
- [331] M. M. Ardakani, M. Karimi, Z. M.M. and S. Mirdehghan, *Int. J. Electrochem. Sci.*, 2008, **3**, 246 – 258.
- [332] H. R. Zare and N. Nasirizadeh, *Electroanalysis*, 2006, **18**, 507–512.
- [333] J. Kunze, I. Burgess, R. Nichols, C. Buess-Herman and J. Lipkowski, *J. Electroanal. Chem.*, 2007, **599**, 147–159.
- [334] G. A. Attard, J.-Y. Ye, P. Jenkins, F. J. Vidal-Iglesias, E. Herrero and S.-G. Sun, *J. Electroanal. Chem.*, 2013, **688**, 249 – 256.
- [335] H. Zhou, F.-R. F. Fan and A. J. Bard, *J. Phys. Chem. Lett.*, 2010, **1**, 2671–2674.
- [336] S. J. Kwon, F.-R. F. Fan and A. J. Bard, *J. Am. Chem. Soc.*, 2010, **132**, 13165–13167.
- [337] S. J. Kwon and A. J. Bard, *J. Am. Chem. Soc.*, 2012, **134**, 7102–7108.
- [338] Y.-G. Zhou, N. V. Rees and R. G. Compton, *Angew. Chem., Int. Ed.*, 2011, **50**, 4219–4221.
- [339] N. V. Rees, Y.-G. Zhou and R. G. Compton, *ChemPhysChem*, 2011, **12**, 1645–1647.
- [340] Y.-G. Zhou, N. V. Rees and R. G. Compton, *ChemPhysChem*, 2011, **12**, 2085–2087.
- [341] Y.-G. Zhou, N. V. Rees and R. G. Compton, *Chem. Phys. Lett.*, 2011, **511**, 183–186.
- [342] Y.-G. Zhou, N. V. Rees and R. G. Compton, *Chem. Phys. Lett.*, 2011, **514**, 291–293.
- [343] E. J. E. Stuart, N. V. Rees and R. G. Compton, *Chem. Phys. Lett.*, 2012, **531**, 94–97.
- [344] Y.-G. Zhou, N. V. Rees and R. G. Compton, *Chem. Commun.*, 2012, **48**, 2510–2512.
- [345] H. Zhou, J. H. Park, F.-R. F. Fan and A. J. Bard, *J. Am. Chem. Soc.*, 2012, **134**, 13212–13215.
- [346] N. V. Rees, Y.-G. Zhou and R. G. Compton, *Chem. Phys. Lett.*, 2012, **525-26**, 69–71.
- [347] S. J. Kwon, H. Zhou, F.-R. F. Fan, V. Vorobyev, B. Zhang and A. J. Bard, *Phys. Chem. Chem. Phys.*, 2011, **13**, 5394–5402.
- [348] E. O. Barnes and R. G. Compton, *J. Electroanal. Chem.*, 2013, **693**, 73–78.
- [349] E. J. F. Dickinson, N. V. Rees and R. G. Compton, *Chem. Phys. Lett.*, 2012, **528**, 44–48.
- [350] E. J. E. Stuart, Y.-G. Zhou, N. V. Rees and R. G. Compton, *RSC Advances*, 2012, **2**, 12702–12705.
- [351] J. V. Macpherson, D. Wakerley, A. Guell, L. Hutton, T. Miller and A. Bard, *Chem. Commun.*, 2013.
- [352] K. Huang, A. Anne, M. A. Bahri and C. Demaille, *ACS Nano*, 2013.
- [353] X. Shan, I. Diez-Perez, L. Wang, P. Wiktor, Y. Gu, L. Zhang, W. Wang, J. Lu, S. Wang, Q. Gong, J. Li and N. Tao, *Nature Nano*, 2012, **7**, 668–672.
- [354] X. Shan, X. Huang, K. J. Foley, P. Zhang, K. Chen, S. Wang and N. Tao, *Anal. Chem.*, 2009, **82**, 234–240.
- [355] X. Shan, U. Patel, S. Wang, R. Iglesias and N. Tao, *Science*, 2010, **327**, 1363–1366.
- [356] A. Kumar, F. Ciucci, A. N. Morozovska, S. V. Kalinin and S. Jesse, *Nat Chem*, 2011, **3**, 707–713.

3

Electrochemical characterization of nano-sized gold electrodes fabricated by nano-lithography

Abstract

We report the lithographical fabrication of Au nanoelectrodes, with a geometrical surface area down to $160 \text{ nm} \times 1 \text{ }\mu\text{m}$. The geometrical surface area of the electrodes is verified using electron microscopy and by electrochemistry through the diffusion limited current of reversible redox couples. Moreover, the electrochemically active surface area of the electrodes is determined from the charges transferred in blank voltammetry. We believe these reproducible nanoelectrodes are well suited for use as probes in nano-electrochemistry research.

3.1 Introduction

Ultrasensitive electrochemical probes are made available through the fabrication of electrodes with nanosized dimensions. Their characteristics, such as fast mass-transport of reactants toward the electrode surface, sensitivity to extremely small currents and nanoscale dimensions have allowed the characterization of fast electron transfer reactions[1], single molecule detection[2] and individual enzyme immobilization.[3] In the field of electrocatalysis, ultrasmall amounts of platinum metal have been electrodeposited and studied as nanoelectrodes.[4, 5]

Several methods have been explored and used to fabricate such nano-sized electrodes. The currently most commonly used methods involve stretching a glass capillary containing a Pt wire of micrometer diameter, until a desired outer diameter is reached for the glass,[6–9] or etching a wire down to an ultrafine tip and coating all but the apex of the metal with an insulating polymer[10, 11]. Lithographical fabrication was introduced by preparing interdigitated arrays of electrodes[12, 13] and allows the design of individual nanoelectrodes patterned on top of a silicon oxide surface.[3, 14, 15] While the microelectrodes based on sealed wires are being produced with very small surface areas, there is no accurate, in-situ control over the actual electrode surface area during manufacture and it has to be determined after fabrication. Moreover, the success rate of such a delicate process is quite low[1, 6, 7, 16]. On the other hand, lithographically produced electrodes require fabrication expertise and electrochemical measurements on them have been troubled by parasitic capacitance.[3, 14, 15]

In this chapter we introduce a nanolithographic method for the reproducible fabrication of nanosized electrodes. Our aim is to demonstrate that these nano-electrodes can be fabricated reliably and reproducibly, and can be characterized by conventional electrochemical methods with low parasitic capacitance allowing measurement of both the real electrochemically active surface area and the geometric surface area of Au nanoelectrodes. To measure the electrochemically active surface area we use a technique commonly applied on macroscopic (single-crystal) electrodes, namely quantifying the charge transferred when stripping a monolayer of oxygen atoms from a Au surface in a blank voltammogram in acidic electrolyte[17]. Few blank voltammograms have been published of nanoelectrodes,[5, 8, 9, 11, 14–16] but they have not been used for accurate determination of the electrode surface area, presumably because they may be hard to generate reproducibly for such nano-sized electrodes. The electrochemically active surface area of the electrode measured can also be compared to geometric surface area as calculated from the diffusion limited current of reversible

redox couples,[18] and moreover, to the geometric surface area using electron microscopy. This leads to an electrochemical characterization of nano-sized electrodes to an extent that has not been achieved previously in the nano-electrochemistry literature.

3.2 Experimental

3.2.1 Chip Design

The design of the electrode assembly, schematically displayed in figure 3.1, has eight metal nanoelectrodes of 1 μm length and 1 μm , 500 nm, 250 nm and 100 nm width as the critical dimension. These electrodes are complimented with a microelectrode of 20 x 100 μm^2 that is used for calibration measurements. The electrodes are connected to leads that end as 1 x 1 mm^2 contact pads to connect to measurement apparatus. As a large part of the chip will be covered in (acidic) liquid electrolyte, the leads are covered by a thin film of silicon nitride that is chemically inert and non-conductive. The surface area of the electrodes that is exposed to the electrolyte is determined by the dimensions of a “window” opening the nitride film.

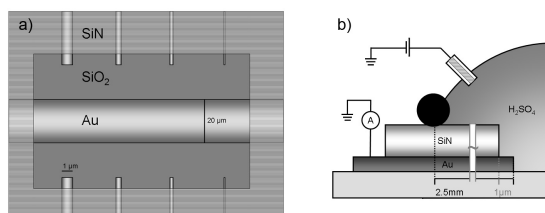


Figure 3.1: a) a top view schematic of the electrode assembly as designed, the microelectrodes are magnified 5 \times for visibility, a silicon nitride passivation layer ensures that only a designated part of the Au film is in contact with the aqueous phase. b) side view: Potential is applied between a reference electrode and the Au film at a contact pad, the current through the working electrode is measured using a low-noise current to voltage amplifier. The black circle represents the O-ring that contains the electrolyte. A scale bar indicates the average lead length covered by electrolyte.

3.2.2 Fabrication

Silicon wafers (4 inch diameter) with a 250 nm thermal SiO_2 layer were cleaned in fuming nitric acid, rinsed in water and dried with N_2 . The wafers are coated with a bilayer of positive e-beam resists: PGMI (PolydiethylGlutarimide 7% in cyclopentanone, spun for 1 minute at 2500 RPM prebaked for 300 s at 200 $^\circ\text{C}$) and PMMA (poly-

methyl methacrylate 2% in anisole, spun for 1 minute at 6000 RPM, prebaked for 300 s at 175 °C). After coating, the design for conductive leads and electrodes was patterned in the resist film using electron beam lithography. The subsequent two-stage resist development consisted of immersion in MIBK/IPA (Methyl isobutyl ketone / iso-propanol; ratio 1:3 for 60 seconds) and iso-propanol (30s, to dilute the MIBK and stop development of the resist layers) for the PMMA top-layer, and in Microposit MF321 developer (10 seconds, followed by H₂O stopper for 15s) for the PGMI layer underneath. Onto the pattern, a film of Au (70nm thickness, 0.1 Å/s) on top of Ti (2nm, 0.5 Å/s) was deposited by means of electron beam evaporation, after which the resist was stripped off in hot Baker PRS3000 photoresist stripper (70 °C). After lift-off, the wafer was cleaned in nitric acid, followed by oxygen plasma treatment to remove any residual resist. The wafer was subsequently coated with a passivation layer of 400nm SiN in a plasma-enhanced chemical vapor deposition (PCVD) chamber at 300 °C. To pattern openings in the silicon nitride layer, in order to allow access of the electrolyte only to the electrode area and to open the contact pads for conductive contact, vinyl tape was applied to the area above the macroscopic contact pads before spincoating a layer of PMMA (950K, 8% in anisole, 1 minute at 1500 RPM) that was subsequently patterned using e-beam lithography and developed in MIBK/IPA (1:3, 120s) and IPA (30 s). Openings in the passivation layer could afterwards be made using dry etching in a fluor plasma (CHF₃ 50 cm³/min and O₂ 2.5 cm³/min, 50 W). All the nanofabrication preparations were carried out at the Van Leeuwenhoek cleanroom laboratory at the Delft University of Technology, additional fabrication details are provided in Appendix A.

3.2.3 Materials

Sulfuric acid (99.999%), ferrocenedimethanol (98%) and copper (II) sulfate pentahydrate (99.995%) were purchased from sigma-aldrich and used without further purification. Solutions were prepared using ultrapure water (18 M cm Milli-Q, Millipore.)

3.2.4 Electrochemistry

Cyclic Voltammograms were measured in a two-electrode setup, using a National Instruments analog-to-digital converter to both supply potential to the electrodes and read out the current that is amplified and converted by a Stanford SR570 low-noise current to voltage amplifier. To this end, labview software was prepared that averages the current measured in each potential step to further reduce the effect of interference

on the signal. The electrochemical chip was isolated in a home-built Faradaic cage, to which the electronic components were external. Inside the Faradaic cage, liquid electrolyte was supplied to the chip surface using a flow-cell setup that consists of a volume of electrolyte connected via Halar tubing to a polyether ether ketone (PEEK) nozzle with a viton O-ring surrounding its orifice that was firmly pressed onto the micro-chip. The PEEK nozzle outputs electrolyte to a drain vessel, and liquid flow is obtained by applying Ar overpressure in the electrolyte source volume.

3.2.5 Numerical Calculations

The rates of mass transfer towards the nanoelectrodes were derived numerically using finite element calculations in COMSOL multiphysics 4.2. The geometry consisted of a $100\ \mu\text{m} \times 20\ \mu\text{m}$ box, on the bottom of which rest a nanoelectrode with length $11.3\ \mu\text{m}$, height 70nm and variable width ('swept' from $50\ \text{nm}$ to $1150\ \text{nm}$ in width in steps of $100\ \text{nm}$), and another cuboid (representing the SiN passivation layer) of width $100\ \mu\text{m}$, length $10\ \mu\text{m}$ and height $400\ \text{nm}$, covering all except $1.3\ \mu\text{m}$ of the box that represents the nanoelectrode. A mesh is generated that is finest near the electrode surface with the mesh cell size growing with distance from the 'electrode' surface. A solution is sought for the gradient in concentration of a diffusive species ('Ferrocenedimethanol'; $D = 6.4 \times 10^{-6}\text{cm}^2/\text{s}$ [19]) that has bulk concentration set to the values used in experiments described below ($C = 0.4\ \text{mM}$). To this end the section of the surface of the electrode that is not blocked by the passivation layer has concentration of 0, corresponding to the steady state condition for an electrode performing a diffusion-limited outer-sphere electrochemical reaction, while the rest of the surfaces are set to bulk concentration. Disregarding effects of convection or migration, the value of the diffusive flux of reagent species towards the electrode yields the diffusion limited current directly when divided by the Faraday constant times the amount of electrons transferred (one for ferrocenemethanol).

3.3 Results

3.3.1 SEM

Figure 3.2a shows an electron micrograph of the area etched in the SiN insulation film to expose 8 nanoelectrodes and one microelectrode, the latter used for calibration purposes as well as counter/reference electrode. The thus exposed Au surface areas range from 0.2 to $1.3\ \mu\text{m}^2$, which is a slight increase over the designed area

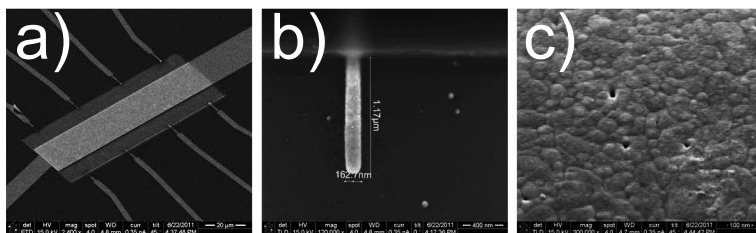


Figure 3.2: a: overview showing the Au nano electrodes of different sizes and the calibration electrode in the center. A rectangular window in the SiN passivation layer exposes the Au and SiO₂ below it to the aqueous electrolyte. b: Close up of a 100nm Au electrode, of which the voltammogram is displayed in figure 3.3b. c: Close up of Au surface roughness, visible with the sample at a 45 degree angle with respect to the electron beam.

as indicated in figure 3.2b. The electrodes patterned in the bi-layer resist are consistently 25nm wider on every side due to metal evaporated into the undercut profile. Moreover, the SiN window is almost 200 nm +/- 50 nm wider than expected, presumably caused by isotropic etching in the dry etch step. Zooming in (figure 3.2c), the electrodes appear slightly rough, consisting of 70 nm crystallites (estimated from SEM measurements) as expected for Au evaporated on a silicon wafer [20].

3.3.2 Blank Cyclic Voltammetry

The gold nano-electrodes shown in figure 3.2 were characterized electrochemically using cyclic voltammetry, the results of which are shown in figure 3.3. These measurements were made after a cleaning procedure that consisted of a 10 minute oxygen plasma treatment followed by boiling and rinsing the chip in milliQ water. Voltammograms shown are as measured directly after insertion and remain stable for at least 30 consecutive cycles. In figure 3.3a, the voltammogram measured at the calibration microelectrode shows features in its blank voltammogram which is comparable to the Au (111) surface.[21] In the positive going scan a series of peaks is observed from 1.3V, that is associated with the formation of a monolayer of oxygen atoms on the Au surface; in particular, the peak at 1.6 V is characteristic for Au(111) domains.[21] In the negative-going return scan, the oxide reduction peak shows a minimum at 1.15V followed by the double layer region. At potentials negative of 0V vs RHE, a reduction current corresponding to the hydrogen evolution reaction is observed.

Figure 3.3b shows the same voltammogram measured on one of the nanoelectro-

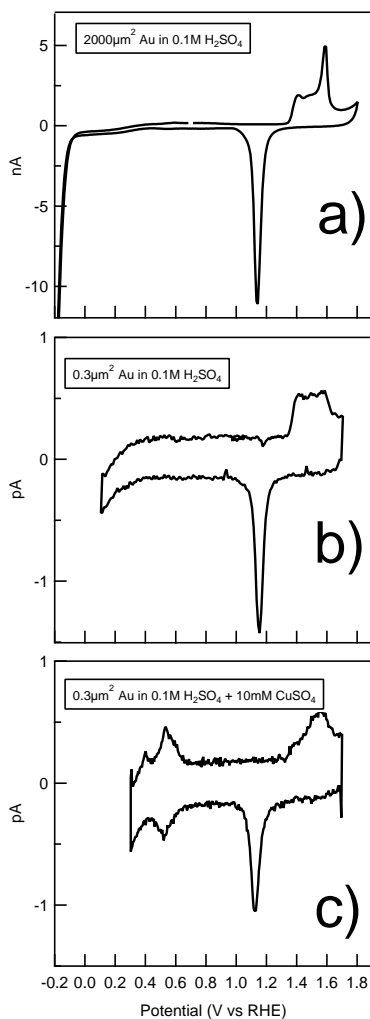


Figure 3.3: blank voltammograms of Au electrodes with designed areas of a) 2000 square micrometer and b) 0.2 square micrometer. Peaks typical for the surface oxide formation and stripping appear at the same potential values while the oxide stripping peak maximum scales four orders of magnitude. The underpotential deposition of Cu is displayed in c).

des with oxidation and reduction features at potentials identical to the calibration electrode. The main difference in the oxide-formation region is the absence of a strong peak at 1.6 V on the nanoelectrode, suggesting that these nanoelectrodes present fewer Au(111) terraces. Below 0.4V a reduction current is observed that we attribute to the reduction of oxygen gas that is permeating through the PEEK nozzle that

contains the electrolyte, followed by the hydrogen evolution current at potentials negative of 0 V. Another noticeable difference is the charging current in the double-layer region which is on average $140\text{fA} \pm 22\text{fA}$ (corresponding to a capacitance of $2.8\text{pF} \pm 0.5\text{pF}$) and larger than expected when considering only the double layer contribution of the nano-electrode surface area, which has a tabulated value between 10 and $50 \mu\text{F}/\text{cm}^2$, [18] or 0.1 - 0.5pF for a square micrometer. A larger capacitance is expected in the case of an electrode-on-silicon assembly, due to the charging interaction between the conductive electrolyte and the Au wiring, separated by the dielectric silicon nitride (as shown in figure 3.1). This contribution can be calculated using the equation for a model parallel plate capacitor:

$$C = \epsilon_r \epsilon_0 \frac{A}{d} \quad (3.1)$$

where ϵ_r is the relative permittivity of the dielectric material and ϵ_0 is the vacuum permittivity, A is the area of the smallest parallel plate and d is the separation of the two plates by the dielectric. Using the surface area of the Au wiring protected from liquid electrolyte ($2.5\text{mm} \times 4 \mu\text{m}$) by the SiN dielectric $\epsilon_r = 7$; [22]) of thickness 400nm yields 1.3pF for the microchip as designed. However, uncertainty in the determination of the area covered by the electrolyte, as well as in the actual thickness of the dielectric film affects the real value of the silicon nitride capacitance.

However, more significant is the capacitance between the Au film and the conductive silicon underneath the SiO_2 layer, which is calculated to amount to 30pF when the entire area of the Au film and the 500nm SiO_2 $\epsilon_r = 4$; [23]) layer thickness is taken into account ($0.42 \times 10^{-6}\text{m}^2$ including the contact pads). Nevertheless, this source of parasitic capacitance can be removed by grounding the silicon in the substrate, allowing the capacitor to discharge into ground. The voltammogram in figure 3.3b is measured while grounding the silicon layer, and (considering the uncertainty in determining SiN capacitance) shows predominantly the SiN charging, with a minor contribution from the double layer charging.

3.3.3 Surface area determination

The real area of a metal surface equals the geometrical area defined by its boundaries only if it is an atomically flat plane, which is not the case for electrodes that are microscopically rough. The rougher a material is, the more surface area is exposed within the same geometrical enclosure. The ratio between the real, electrochemically active area of an electrode and its geometrical area is therefore called the roughness factor

of the electrode.

The electrochemically active surface area or the amount of surface atoms exposed to the electrolyte can be obtained from comparing the charge transferred when exactly one overlayer of gold oxide is reduced from the electrode (i.e. the integral of the cathodic current peak at 1.15V) to the value tabulated for this process on a flat gold surface, $400 \mu\text{C}/\text{cm}^2$. [17] Dividing this electrochemically active surface area by the geometrical area measured using the SEM images gives the roughness factor for the nanoelectrode under consideration. For example, the voltammogram in figure 3.3b shows an oxidation and reduction wave in which $1.4\text{pC} \pm 0.1\text{pC}$ is being transferred, yielding an electrochemically active surface area of $0.35 \mu\text{m}^2 \pm 0.03 \mu\text{m}^2$.

Attempts were also made to calculate the real surface area from the charge transferred when stripping a monolayer of underpotential deposited (UPD) copper off the electrode surface. A cyclic voltammogram describing this procedure is displayed in figure 3.3c, where the Cu UPD signal shows a reduction peak and a shoulder leading to the overpotential deposition. In the oxidative sweep two anodic peaks are observed, corresponding to the removal of a full Cu overlayer on the Au in two steps. The clear separation into two peaks is typical of a Cu UPD on Au(111) surfaces [24]. When the potential sweep is extended beyond the range displayed in fig. 3.3c, the overpotential deposition is observed as an exponential current decrease and, in the positive going return sweep, as a third oxidative peak. Nevertheless, the Cu UPD charges could not be evaluated reproducibly, because a parasitic current caused the voltammogram to slant, at different angles for different electrodes. Possibly the presence of Cu adatoms reduces the overpotential required to reduce dissolved oxygen, presence of which cannot be excluded in our current setup.

The average roughness factor obtained for the nanoelectrodes from the oxide stripping charge is 3.2 ± 0.2 , while the charge transferred at the calibration electrode (figure 3.3a) corresponds to a roughness factor of 1.5. Previous electrochemical estimates of surface roughness on macroscopic evaporated Au thin-film electrodes range between 2 and 2.5 [20, 25]. Since both the calibration electrode and the nanoelectrodes were deposited at the same time, it is not to be expected that their microstructure should change significantly. A previously published blank voltammogram measured on lithographically produced Au nanoelectrodes in the same potential domain, [14] however, exhibits an oxide stripping charge in excess of the geometric area by a factor close to 10, citing electrolyte leakage through the passivation layer as a possible cause for the unexpected surface area increase. Considering that nanoelectrodes have significantly more borderline with the passivating nitride layer per square micron compared

to the calibration electrode, it is to be expected that leakage plays a more important role for the nanoelectrodes. The presence of pinholes in the SiN, that may reveal additional surface area for the nanoelectrodes was tested by electrodepositing large quantities (i.e. 5 μm) of Cu. Analyses by optical microscopy afterwards showed no deposits along the unexposed Au leads.

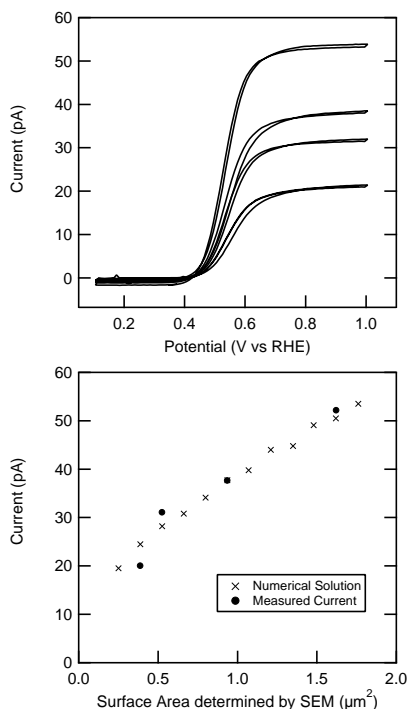


Figure 3.4: A) Cyclic voltammetry of Au nanoelectrodes in a solution containing 0.4mM ferrocenedimethanol and 0.1M sulfuric acid as a supporting electrolyte. B) shows the current plateau value versus the surface area as determined by SEM, for results of experiments and finite-element calculations.

In addition, the geometrical surface area of the electrodes was estimated by measuring the diffusion limited oxidation current of a redox couple with fast kinetics, which depends only on the concentration and the diffusion coefficient of the electroactive species and the electrode surface area. In figure 3.4a, the oxidation of ferrocenedimethanol (in 0.1M H_2SO_4 as supporting electrolyte) during a cyclic voltammogram is shown as a sigmoidal current wave. This CV-shape is expected for a diffusion-limited reaction at ultra-micro electrodes, with the plateau value a function of the electrode

geometrical surface area:[18]

$$I_{diff} = nFDCm_0A \quad (3.2)$$

Here n is the number of electrons transferred in the reaction, F is Faraday's constant, D is the diffusion coefficient of the redox molecule and C is its concentration in the bulk. The constant m_0 is related to the geometry of the electrode and its size; this constant can be provided analytically for shapes such as (hemi)spheres and disks. In the case of complicated shapes as used in this investigation, the value of m_0 can be found numerically.

To compare the measured currents to the values expected from theory, the diffusion-limited current equation was solved numerically, using a geometry model based on SEM measurements (the details of the calculations are explained in the experimental section). These calculated results are plotted in fig 3.4b together with the experimental findings.

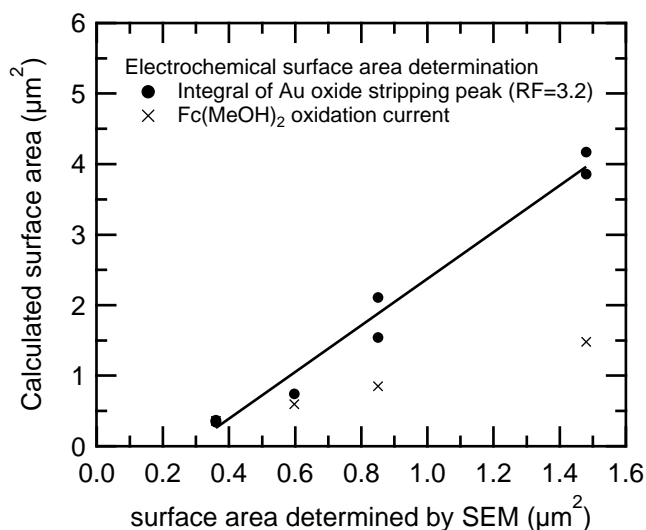


Figure 3.5: electrode surface areas calculated from the charge transferred during the stripping of an oxide monolayer (circles) and the diffusion limited current (crosses). A least squares fit reveals the roughness factor of the calculated area with respect to the geometrical area determined using the SEM.

In figure 3.4b, for the case of electrodes of 550nm and 1050nm in width, good agreement is found for the diffusion-limited current measured and the current derived from calculations, whereas the smaller electrodes show a deviation from the numerical

results of around 10-20%. Since the ferrocenedimethanol oxidation experiments are performed consecutively in the same solution, changes in the value of C and D are not expected. However, a deviation of 10-20% between the actual surface area and the value provided in the calculation for the smaller electrodes is reasonable once it is considered that fabrication errors such as overetching or lift-off errors have more impact on features of small area[3].

Both electrochemical methods used to determine the surface area of the electrodes are plotted against the surface area obtained from the electron microscopy in figure 3.5. The slopes differ since the measurements should theoretically supply the electrochemically active surface area (oxide monolayer stripping), and the geometrical surface area (diffusion limited current), respectively. The trends agree well with the designed surface area ratios of the electrodes and indicate a satisfactory control over the electrode surface area using this fabrication technique.

3.4 Conclusion

Using lithographic techniques, individually addressable gold electrodes were reproducibly fabricated with electrochemically active surface areas down to $0.3 \mu\text{m}^2$. We succeeded in obtaining comparable calculated surface areas by measuring the oxide monolayer stripping integral and the diffusion limited ferrocenedimethanol oxidation current in comparison to the surface areas estimated from scanning electrode microscopy. These results demonstrate that we have developed a suitable and reliable technology for fabricating clean gold nanoelectrodes reproducibly. We will employ these electrodes in future nano-electrochemistry research.

Bibliography

- [1] Penner, R. M.; Heben, M. J.; Longin, T. L.; Lewis, N. S. *Science* 1990, 250(4984), 1118–1121.
- [2] Zevenbergen, M. A. G.; Wolfrum, B. L.; Goluch, E. D.; Singh, P. S.; Lemay, S. G. *J. Am. Chem. Soc.* 2009, 131(32), 11471–11477.
- [3] Hoeben, F. J. M.; Meijer, F. S.; Dekker, C.; Albracht, S. P. J.; Heering, H. A.; Lemay, S. G. *ACS Nano* 2008, 2(12), 2497–2504.
- [4] Chen, S.; Kucernak, A. *J. Phys. Chem. B* 2004, 108(37), 13984–13994.
- [5] Chen, S.; Kucernak, A. *J. Phys. Chem. B* 2004, 108(10), 3262–3276.
- [6] Shao, Y.; Mirkin, M. V.; Fish, G.; Kokotov, S.; Palanker, D.; Lewis, A. *Anal. Chem.* 1997, 69(8), 1627–1634.
- [7] Pendley, B. D.; Abruña, H. D. *Anal. Chem.* 1990, 62(7), 782–784.
- [8] Jena, B. K.; Percival, S. J.; Zhang, B. *Anal. Chem.* 2010, 82(15), 6737–6743.
- [9] Guo, J.; Ho, C.-N.; Sun, P. *Electroanalysis* 2010, 23(2), 481–486.
- [10] Slevin, C. J.; Gray, N. J.; Macpherson, J. V.; Webb, M. A.; Unwin, P. R. *Electrochem. Commun.* 1999, 1(7), 282–288.
- [11] Mészáros, G.; Li, C.; Pobelov, I.; Wandlowski, T. *Nanotechnology* 2007, 18(42), 424004.
- [12] Kittlesen, G. P.; White, H. S.; Wrighton, M. S. *J. Am. Chem. Soc.* 1984, 106(24), 7389–7396.
- [13] Bard, A. J.; Crayston, J. A.; Kittlesen, G. P.; Varco Shea, T.; Wrighton, M. S. *Anal. Chem.* 1986, 58(11), 2321–2331.
- [14] Mészáros, G.; Kronholz, S.; Karthäuser, S.; Mayer, D.; Wandlowski, T. *Appl. Phys. A: Mater. Sci. Process.* 2007, 87(3), 569–575.
- [15] Kronholz, S.; Karthäuser, S.; Mészáros, G.; Wandlowski, T.; van der Hart, A.; Waser, R. *Microelectron. Eng.* 2006, 83(4-9), 1702–1705.
- [16] Zuliani, C.; Walsh, D. A.; Keyes, T. E.; Forster, R. J. *Anal. Chem.* 2010, 82(17), 7135–7140.
- [17] Trasatti, S. O. P. *Pure Appl. Chem.* 1991, 63(5), 711–734.
- [18] Bard, A. J.; Faulkner, L. R. *Electrochemical Methods: fundamentals and applications*; Wiley, 2001.
- [19] Zhang, W.; Gaberman, I.; Ciszowska, M. *Electroanalysis* 2003, 15(5-6), 409–413.
- [20] Miyake, H.; Ye, S.; Osawa, M. *Electrochem. Commun.* 2002, 4(12), 973–977.
- [21] Angerstein-Kozłowska, H.; Conway, B. E.; Hamelin, A.; Stoicoviciu, L. *J. Electroanal. Chem. Interfac. Electrochem.* 1987, 228(1-2), 429–453.
- [22] Piccirillo, A.; Gobbi, A. L. *J. Electrochem. Soc.* 1990, 137(12), 3910–3917.
- [23] Gray, P. R.; Hurst, P. J.; Lewis, S. H.; Meyer, R. G. *Analysis and Design of Analog Integrated Circuits*; Wiley, 5 ed., 2009.
- [24] Hachiya, T.; Honbo, H.; Itaya, K. *J. Electroanal. Chem. Interfac. Electrochem.* 1991, 315(1-2), 275–291.
- [25] Golan, Y.; Margulis, L.; Rubinstein, I. *Surf. Sci.* 1992, 264(3), 312–326.

4

Influence of hydrazine-induced aggregation on the electrochemical detection of platinum nanoparticles

Abstract

To study the catalytic activity of single nanoparticles (NPs) electrochemically, we investigated the applicability of a novel method for nanoparticle detection as a means to immobilize individual NPs. This method consists of analyzing the current steps that can be measured at an ultramicroelectrode (UME) when a colloid of NPs is injected into an electrolyte containing an electroactive species, that is turned over at the NP but not the UME surface. We have measured these current steps for the hydrazine oxidation at Pt NPs landing on a lithographically fabricated Au UME, showing a mean step size comparable to theory and prior measurements. We found a reduced landing frequency with respect to values reported in the literature and those predicted from theory, while the current step distribution showed a long tail of large current steps. This could be explained by the particle aggregation, which would lower the effective NP concentration and therefore lower the landing frequency and would result in higher current steps when aggregates reach the electrode. Cyclic voltammetry (CV) measurements of the Pt-modified Au UME showed a signal characteristic of the presence of Pt, while electron microscopy revealed aggregated NPs, after landings were performed in the presence of hydrazine or hydrogen gas. Conversely, no aggregates were found after particles were injected in absence of such reducing agents, while CV still suggested the presence of Pt, indicating individual particles. The finding, that landing nanopar-

ticles in the presence of hydrazine yields NP aggregates on the surface, means that this particular method is currently not suited for the preparation of individually immobilized particles to facilitate catalysis studies at individual nanoparticles.

4.1 Introduction

Metal nanoparticles (NPs) are employed in a wide variety of scientific subjects and technical applications.[1, 2] In applications such as catalysis such particles present, above all, a large surface-to-weight ratio that is instrumental to cost abatement when using expensive metals. Moreover, the exact shape and size of a metal particle can influence its characteristics. For instance, surface plasmons of gold particles change in energy with the particle dimension,[3] and in heterogeneous catalysis there is an ongoing debate about the dependence of catalytic activity on particle size and shape.[4–6] In catalysis, it is assumed that for every reaction there exists an optimal particle size that is presently determined through analysis of large particle populations in macroscopic screening experiments.[7, 8] The results of these measurements are compared to the particle size distribution that is determined through e.g. TEM imaging. The ability to measure the activity of individual particles would circumvent the statistics involved in ensemble studies and point out exactly which part of the size distribution is most active. In other areas of catalysis, great advances have been made to study the activity of individual catalyst particles. The interactions inside individual zeolite particles have been elucidated in heterogeneous catalysis,[9] while the biocatalytic properties of individual enzymes have also been revealed using confocal microscopy.[10] Electrocatalytic measurements are very promising in this respect, because very small electrochemical currents can be detected. Measurements on individual catalyst particles in electrochemistry have been performed on a single Pt nanoparticle electrodeposited on the tip of thin carbon fibre UME,[11, 12] on nanoparticles attached to the side walls of carbon nanotubes,[13] and on an extremely small number of enzymes immobilized on a Au UME.[14] These measurements open up a path to the study of single particles with size distributions found in applied catalysis.

Recently, a new electrochemical method has been introduced to monitor individual nanoparticles by detecting their arrival at the conducting surface of an ultramicroelectrode (UME). The idea of the method is illustrated schematically in figure 4.1. The UME is placed in a solution containing some electroactive species as well as catalytic nanoparticles (NP), and held at a potential at which the electrochemical reaction does not occur at the UME surface, but does occur at the surface of the nanoparticles if they

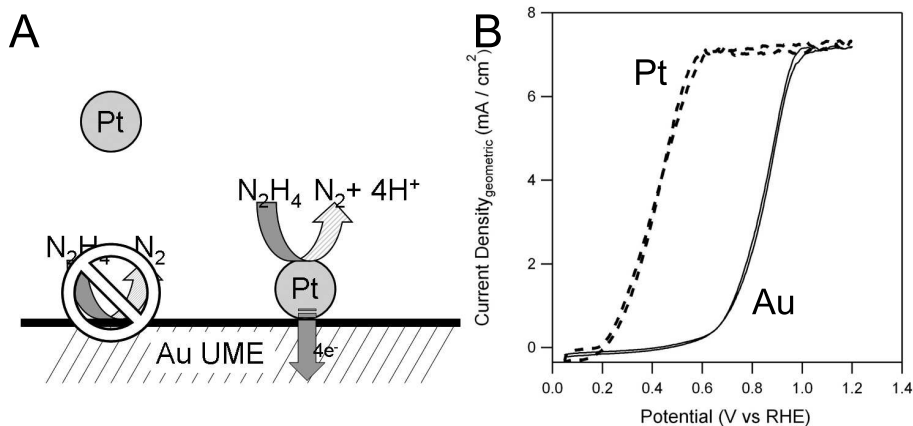


Figure 4.1: (A) The principle of nanoparticle detection mediated by the oxidation of hydrazine is schematically displayed: At a given potential, hydrazine will not be oxidized at a Au surface, while a Pt particle attached to gold will catalyze this reaction. (B), Current-Voltage plots of the hydrazine oxidation measured at Pt and Au rotating disk electrodes, depicting the difference in the onset potential of hydrazine oxidation on Pt (dashed) and Au (full) electrodes. These measurements were performed at 700 RPM and 50 $mV s^{-1}$ in a 50 mM phosphate buffer of pH 8, containing 5 mM hydrazine.

make contact with the UME electrode surface at random. An appropriate combination of electrode material, nanoparticle material and electrochemical reaction ensures that the UME surface gives no electrochemical signal, so that all the electrochemical activity must come from colliding nanoparticles. After being introduced to the system, the nanoparticles will randomly approach the electrode surface and so far two types of UME-NP interactions have been observed: a current step[15–18], and a current spike that decays to background level.[19–27] A staircase response is indicative of a cumulative immobilization of active particles on the UME surface. This type of response was observed for the first time in the Bard group, upon adding a dilute solution of Pt NPs to a neutral electrolyte containing a low concentration of hydrazine (N_2H_4) and a Au UME held at a potential where hydrazine is oxidized at Pt but not at Au. [16]

A spike-type response, on the other hand, signifies a fleeting interaction, either because the particle is oxidized completely, or because it briefly performs a reaction before departing from the surface. In the Compton group, current spikes were measured for the direct oxidation of Ag NPs at a carbon UME.[21] In these spikes a charge was passed corresponding to the ionization of nanoparticles when the electrode was held at a potential above the oxidation of the silver metal. In another measurement,[19]

a Pt UME was passivated by oxidizing its surface at a high potential, and subsequently iridium oxide particles were added that catalyze the oxygen evolution reaction. Current spikes were observed suggesting that the nanoparticles were only briefly contacting the surface.

The frequency at which these landings occur has been reported to depend linearly on NP concentration with average molar collision frequencies of $1.5 \times 10^4 - 2.5 \times 10^4 \text{ s}^{-1} \mu\text{M}^{-1} \text{cm}^{-2}$ [16] and $3.9 \times 10^4 \text{ s}^{-1} \mu\text{M}^{-1} \text{cm}^{-2}$. [21]

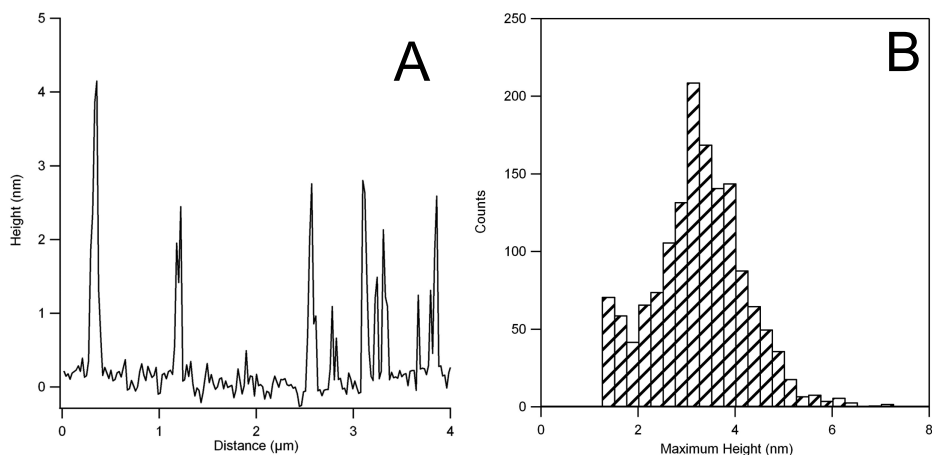


Figure 4.2: A) Linescan of a typical AFM measurement of Pt nanoparticles freeze-dried on silicon. B) Pt NP- height distribution measured using AFM, revealing the mean particle size.

This method for detecting nanoparticles could very well be applied to the study of the catalytic activity of individual particles. In order to realize this, it is necessary to verify that substrates, after showing a specific number of ‘landing events’ during electrochemical detection, have an equivalent number of homogeneously distributed nanoparticles stuck to the electrode surface. If so, one could aim to control the number of landings so as to study the electrocatalysis of a controlled number of nanoparticles.

Therefore, in this chapter we show ex-situ measurements after landing experiments in order to ascertain what is present on the metal surface. We report the detection of Pt nanoparticles using a Au ultramicroelectrode (UME); subsequently we show electron micrographs and cyclic voltammograms to characterize the composition of the electrode surface before and after measuring landing events. These measurements suggest that a landing event detected by hydrazine oxidation does not necessarily correspond to the arrival of an individual nanoparticle. In fact, we present evidence that

the presence of a strong reducing agent, such as hydrazine and hydrogen, may induce aggregation of ligand-capped nanoparticles in solution.

4.2 Experimental

4.2.1 Materials

Sulfuric acid (UltraPur), sodium di-hydrogen phosphate and di-sodium hydrogen phosphate (both, pro analysi) salts and tri-sodium citrate dihydrate (pro analysi) were purchased from Merck, hydrazine hydrate (98%), chloroplatinic acid hydrate (99.9%) was purchased from Sigma-Aldrich. Sodium Borohydride (98+%) was purchased from Acros Chemicals. Before starting a measurement, argon gas with a purity grade of 6.0 was bubbled through the electrolyte (prepared using MilliQ water of 18 M cm resistivity) to remove the majority of atmospheric oxygen. In measurements using hydrogen gas, hydrogen of 5.0 purity grade (BIP Grade, AirProducts) was bubbled through the electrolyte solution.

4.2.2 Lithographical fabrication of microelectrodes

The electrodes used in this experiment were lithographically produced Au UMEs on a chip, the fabrication of which has been detailed in Appendix A. In summary, we pattern electrodes and their electronic leads in a bi-stack of PMGI and PMMA using an electron beam pattern generator at 100 kV (EBPG5000+, Vistec). The pattern is filled with 2 nm of an adhesive Ti layer and a Au layer of 70 nm by electron beam evaporation. To protect all but a controlled electrode surface area from the electrolyte, we first cover the entire chip with a thick (400nm) SiN passivation film by Plasma Enhanced Vapor Deposition. In a subsequent electron beam lithography step, the 100 x 50 μm^2 area containing the electrodes is de-protected by Reactive Ion Etching of the SiN in a plasma of CHF_3 and O_2 . This last step exposes eight nanoelectrodes (varying in size from 50x500 nm^2 to 1000x500 nm^2) and one microelectrode of 100 x 20 μm^2 . The successful outcome of the microchip fabrication was verified by Scanning Electron Microscopy (SEM, FEI Nova 200 NanoSEM) and cyclic voltammetry.

Electrolyte is provided in a flow-cell setup from a 200 mL volume containing the electrolyte and a reference electrode. By applying slight argon overpressure to the electrolyte, it flows through 30 cm of Halar or Teflon tubing into a PEEK cell that is firmly depressed onto the chip with a Viton O-ring. During measurements, the electrolyte is flowing (typical flow-rate ~1 ml/min) for the first two minutes after injection, to

ensure that the nanoparticle concentration near the chip is equal to that in the solution, afterwards the argon pressure is released to stagnate the electrolyte flow.

4.2.3 Electrochemical Measurements

The current flowing through the electrode is measured using a Stanford SR570 I-V amplifier, the output of which is read by the same analog-to-digital converter (NI USB-6251) that is used to apply a potential between the UME and a reference electrode that also functions as the counter electrode. In most experiments the reference electrode was a mercury-mercurous sulfate electrode (MSE; Radiometer Analytical XR230), while in some cases a Pt flag ($\sim 4.5 \text{ cm}^2$) was used as a reference electrode. Data collection is performed using LabView. The measurement was performed inside a Faraday cage to minimize interference to the signal. Landing measurements were performed in a phosphate buffer at pH 8, with a concentration of 10 mM. These conditions are close to those reported in earlier, similar experiments[16] and were chosen because extreme pH values and high buffer salt concentrations tend to aggregate nanoparticles in solution. When going through a range of buffer concentrations (from 1 mM to 100 mM phosphate) and pH values (pH 6 and pH 8), we have not found a significant change in experimental behaviour and therefore measurements at only one value (10 mM) are shown herein.

For comparison with the literature, measurements were also performed using a commercial Au UME with a diameter of 25 μm (CHI106, CH Instruments), in a glass cell with 100 mL of electrolyte. Measurements were performed using the same instrumentation as mentioned above, in a two-electrode setup with a commercial MSE reference electrode as the second electrode.

Rotating Disk Electrode (RDE) measurements were performed using a Pine Instruments (AFMSRXE) system, employing 5 mm Au and Pt disk electrodes supplied by Pine Instruments, and coiled Au and Pt wires respectively as counter electrodes whilst using the MSE as a reference.

4.2.4 Nanoparticle Synthesis

Nanoparticles were synthesized according to a recipe from the literature:[16, 28] to a stirred mixture of H_2PtCl_6 and $\text{Na}_3\text{Citrate}$, NaBH_4 was added dropwise. We used the following molar concentrations: 1 mmol :1 mmol :10mmol (Pt: Citrate: Borohydride) in 20 mL of water. The resulting colloid does not show precipitation within several months.

The NP concentration was evaluated with AFM,[29] by freeze-drying a known volume of Pt colloid onto a known surface area of Si wafer. AFM measurements were performed on a Veeco/Bruker Multimode AFM microscope with a Nanoscope IIIa controller using Olympus AC 160TS Micro Cantilevers (tip radius <10nm). Data analysis on the images was performed using the WSxM software[30] to flatten the images (i.e. remove baseline contributions) and count the amount of particles and their height. An example of one of the linescans that constitute an AFM image is shown in Figure 4.2A. The 2D density of particles obtained in this way was then calculated back to the initial concentration to yield $1.4 \pm 0.5 \mu\text{M}$, which is a factor $7.1 \pm 2.6 \times 10^2$ lower than the initial atomic concentration and therefore corresponds to a nanoparticle diameter between 2.6 and 3.3 nm.[31] To appreciate this value we may compare it with the particle height distribution determined by AFM which has a mean of 3.3 ± 1.0 nm, shown in Figure 4.2B. In addition to this, particle size measurements were also performed using XRD on a Philips PAnalytical X'Pert system. The Scherrer formula[32] was used to estimate the crystallite size of the Pt NPs, resulting in a value of 3.8 nm for the average particle size, both for a freshly prepared solution and an aged solution. It should be noted that these sizes agree closely to those reported in the recipe that we have followed.[16, 28]

4.3 Results

In order to detect the landing events of the platinum nanoparticles on the gold electrode, we choose an electrochemical reaction that, at the selected potential, occurs only on the surface of the Pt nanoparticles and not at the gold electrode, in this case hydrazine oxidation. The difference in reactivity between Pt and Au can be appreciated from the different onset potentials for the oxidation of hydrazine in the CVs displayed in figure 4.1B. This reaction is catalyzed by platinum at potentials above 0.2 V vs. RHE,[33, 34] and a current response is expected when a Pt NP contacts the gold electrode if the gold electrode is polarized at a value higher than 0.2 V vs. RHE. In the landing measurements to be described below we have chosen values of 0.35, 0.45 and 0.55 V vs. RHE, where the background current is low because the onset of the hydrazine oxidation on the Au UME was found in our setup to start at 0.6 vs RHE. These values are comparable to those reported in the literature.[16, 35, 36]

Figure 4.3 shows a current-time measurement after adding 200 μL of citrate-capped Pt NPs (corresponding to 1.4 ± 0.5 nmol/liter) to a solution of 10 mM hydrazine, and we observe changes in the current (in steps) presumably caused by the Pt nanoparticles

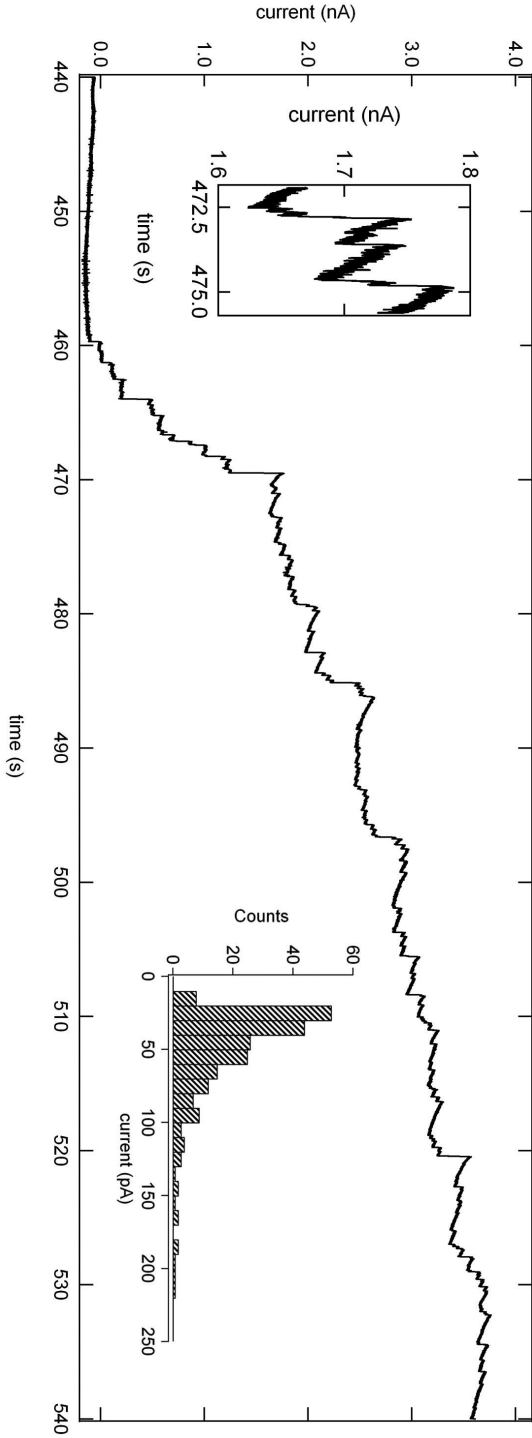


Figure 4.3: Discrete current increments caused by the oxidation of 10mM hydrazine at Pt NPs impacting onto the surface of a $2000 \mu\text{m}^2$ Au UME, held at 0.35 V vs RHE, in 10 mM phosphate buffer of pH = 8. Inset on the right is the histogram of the step height distribution. Inset on the left is a magnification of some current steps.

landing on the surface of the gold electrode. After the initial step a slow decrease in current is observed. The time-constant for this decrease does not agree with those for capacitive discharging or Cottrell-type mass-transport effects. We therefore attribute this current decay to deactivation of the nanoparticles, presumably as a result of contamination, as has been suggested previously. [16] Before landing of the nanoparticles, the current is stable and slightly cathodic, which can be ascribed to the reduction of a trace of oxygen. The cascades of collisions take place with an average landing frequency of ~ 2 landings s^{-1} . This landing frequency is lower than the expected value extrapolated from the literature, [15, 16, 21] even though in our experiments the nanoparticle concentration and the area of the microelectrode used are both higher than values reported in other experiments. It should be noted that no difference in the landing frequency was found between conditions of flowing or stagnant electrolyte. When we perform the same measurement using a glass sealed Au UME, we also obtain a lower landing frequency than expected (~ 0.02 landings s^{-1} at equal concentration, while the electrode surface area is four times smaller than the surface area of the lithographically fabricated UME), as can be seen in Figure 2 of Appendix B. The landing frequency reported by Bard et al. [16] for the hydrazine-mediated detection of Pt NPs, is $0.01 \text{ s}^{-1} \text{ pM}^{-1}$, or 10 landings per second extrapolated to our particle concentration, on an electrode with a surface area that is twenty-five times smaller than the one employed in our study.

The nanoparticle landing frequency may be estimated according to Fick's law, assuming diffusion-limited steady-state conditions: [16, 37]

$$J = \kappa \chi D_{NP} C_{NP} \quad (4.1)$$

where κ is a sticking coefficient ($0 < \kappa < 1$), χ is geometry factor (for a disk, $\chi = 4/\pi a$, with a the UME radius), D_{NP} the nanoparticle diffusion coefficient and C_{NP} their concentration in solution. In our experiment we can accurately determine the surface area of the UME, and the diffusion coefficient is a constant, that can be calculated from the Stokes-Einstein equation

$$D = \frac{k_b T}{6\pi\eta r} \quad (4.2)$$

depending only on the particle radius r and the solution viscosity η as variables. The viscosity for water is a known constant, and the particle radius as well, albeit with a some uncertainty. However, this uncertainty does not explain the observed deviation in the landing frequency. The geometry factor χ of our system is quite complicated

and requires numerical calculations to be determined exactly, but it is constant. We have previously simulated the diffusion of species to similar UMEs[38] and the resulting flux is comparable to the theoretical flux to similar sized, disk-shaped electrodes. Therefore we do not expect the particular geometry of our system to account for a large change in the landing frequency. The sticking coefficient κ , a factor indicative of the probability that a particle attaches to the surface upon colliding with it, was introduced by Bard et al.[18] to accommodate for a deviation between the experimentally observed and theoretically predicted landing frequency (when $\kappa = 1$). We however have no adequate means to estimate the value for κ . Finally, the nanoparticle concentration is calculated from the estimated nanoparticle size. This value can however change greatly if the particles aggregate in solution, prior to landing. Large particle clusters can form during aggregation in solution, lowering significantly the concentration of non-aggregated nanoparticles in solution. Further results below indicate that aggregation indeed seems to occur during our measurements.

The inset on the left in Figure 4.3 shows a detail of the current step, where the initial spike amplitude was used as the current step height value in order to establish the distribution of current step heights from the landing events (shown on the right in Figure 4.3). A broad distribution of peak heights is observed, ranging between 20–200 pA, while the modal current values are between 20 and 50pA. The mean current step height will include the the higher values in the tail of the distribution and is therefore higher. Theoretically, the current step amplitude should be related to the radius of the incoming nanoparticle, as well as to the concentration of hydrazine (see equation 3 below), and therefore this amplitude distribution in one experiment should reflect the nanoparticle size distribution. Size measurements on colloiddally synthesized nanoparticles generally show a normal distribution of the particle diameter and we have observed the same in our AFM measurements, but the peak height distribution we measure shows a much broader tailing distribution, that should however still be linked to the size distribution of the colliding nanoparticles.

The observed distribution in Figure 4.3 can be fitted with a convolution of Gaussian curves, as has been performed for other nanoparticle landing experiments.[27] In their experiments, Rees et al. showed that the data presented several normal distributions with a mean value related to a function of a multiple of the initial NP radius, suggesting nanoparticle aggregation.

Returning to the idea that the current steps correspond to the landing of an individual nanoparticle, the nanoparticle radius can be related to the measured current step, if we assume that the particle oxidizes hydrazine at the diffusion limited current,

according to the following equation for the theoretical diffusion limited current at spherical particles suspended on a plane: [16]

$$I = 4\pi(\ln 2)nFD_{HZ}C_{HZ}r_{NP} \quad (4.3)$$

where n is the electron transfer (4 electrons in this reaction), F is Faraday's constant, C_{HZ} is the concentration of hydrazine ($10 \mu\text{mol cm}^{-3}$) and r_{NP} is the nanoparticle radius. A wide range of diffusion coefficients for hydrazine (D_{HZ}) has been reported in the literature, ranging from $3.2 \times 10^{-6} \text{ cm}^2 \text{ s}^{-1}$ [39] to $2.37 \times 10^{-5} \text{ cm}^2 \text{ s}^{-1}$. [40] Moreover, values for D_{HZ} can be derived from publications in which they are not mentioned explicitly, yielding $1 \times 10^{-6} \text{ cm}^2 \text{ s}^{-1}$, [36] $2 \times 10^{-6} \text{ cm}^2 \text{ s}^{-1}$, [33] and $1 \times 10^{-5} \text{ cm}^2 \text{ s}^{-1}$, [35] whereas from the UME measurements reported by Bard et al. [16] a diffusion coefficient of $6.3 \times 10^{-6} \text{ cm}^2 \text{ s}^{-1}$ is estimated. From the diffusion-limited current value in figure 4.1B, using the Levich equation, we obtain a diffusion coefficient of $6.4 \times 10^{-6} \text{ cm}^2 \text{ s}^{-1}$. This variance in D_{HZ} suggests that the diffusion limited current for hydrazine is very much dependent on measurement conditions, as otherwise a more unambiguous number would have arisen. Choosing the value measured in the RDE experiment we expect a current step of ca. $36 \pm 11 \text{ pA}$ for a particle of $3.3 \pm 1.0 \text{ nm}$ diameter in a solution with 10 mM of hydrazine. We emphasize here that equation 3 applies specifically to spheres on infinite planes. If a NP would land on another NP already sticking to the surface, the flux of electrocatalytic substrate to the ensemble would be smaller and a lower current step would be expected. This should hold especially for the case of a particle impacting on an aggregate of particles at the surface.

Particle aggregates should yield a higher value than the current for a single particle, however, this factor is influenced heavily by the geometry and density of the aggregate since a catalytic reaction must be performed at the constituent surface of the NP aggregate. Nevertheless, we suppose that the very high landing currents (of around 200 pA) should be ascribed to aggregated particles sticking to the surface.

Figure 4.4 shows the current step distributions at three electrode potentials, i.e. 0.35 , 0.45 , 0.55 V vs RHE. For all potentials, most current steps are reasonably close to the theoretical estimate of 36 pA , which appears to confirm the model suggested by Eq.3 for the selected diffusion coefficient. The lack of increase in current at higher potentials suggests that the reaction is in a diffusion-limited regime. This does not correspond well to the CV for a Pt RDE, shown in figure 4.1B, and implies that at a Pt nanoparticle the current-voltage characteristics are not the same as at a macroscopic disk. The current steps are also very similar to those observed in the literature, [16] though, as mentioned, our landing frequency is always considerably lower.

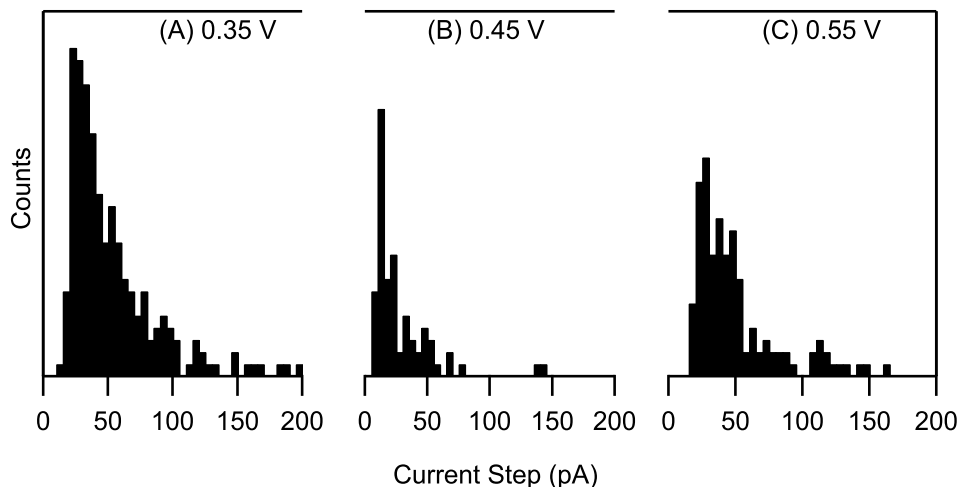


Figure 4.4: Current step height distributions measured at three UME potentials.

In order to verify the presence of the Pt NPs on the Au UME, cyclic voltammograms of the Au UME are measured in sulfuric acid before and after the landing experiment. Figure 4.5 shows the two CVs, with the dashed line corresponding to the gold electrode before the addition of Pt NPs and the black curve to the gold electrode after landing Pt NPs. The dotted curve agrees well with the blank CV of gold in sulfuric acid.[41] In the CV measured after landing Pt NPs, by comparison with the clean Au CV, we conclude that most of the underlying gold is still in contact with the solution, judging from the charge passed during surface oxidation and reduction between 1.0 and 1.6 V. However, the presence of Pt on the Au UME is also evidenced. A major difference in hydrogen evolution current is seen at 0 V, a reaction for which platinum is a far more active catalyst than gold. Also features indicative of the adsorption and desorption of underpotential deposited hydrogen on the Pt surface are observable between 0.1 and 0.3 V, while the small anodic and cathodic features near 0.7 and 0.6 V, resp. correspond to the surface oxide formation and subsequent reductive stripping on a Pt electrode.

After having deposited the nanoparticles on the Au UME, Scanning Electron Microscopy (SEM) is used to inspect the electrode surface, and Figure 4.5B shows a micrograph overview of the UME surface. Rather than single particles, we observe large aggregates of nanoparticles (in bright white) uniformly dispersed over the sur-

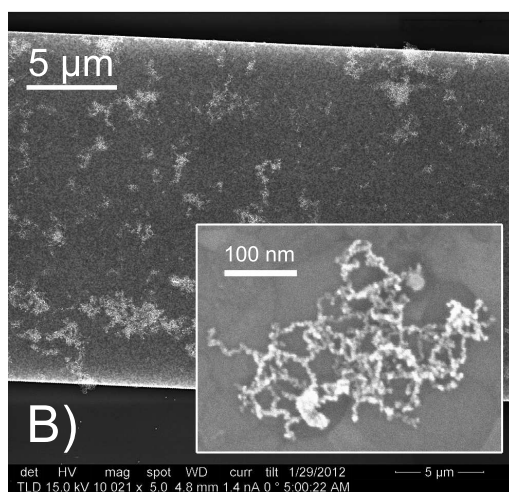
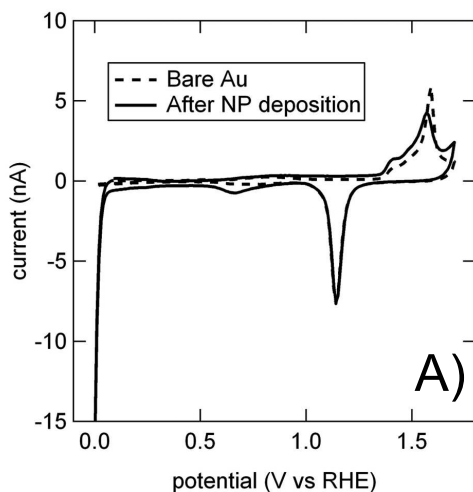


Figure 4.5: (A) Cyclic voltammograms of the gold UME in 0.1M H₂SO₄ before (dotted line) and after (black line) landing events using hydrazine oxidation as a detection reaction at 0.35 V vs. RHE. In the gold CV after landing events (black line) electrochemical signals due to the presence of platinum can be clearly observed: Pt surface oxidation and reduction between 0.6 and 0.85 V, and hydrogen evolution around 0 V. (B) SEM image of the same Au UME after landing Pt NPs on the electrode using hydrazine oxidation as electrochemical detection reaction, with an inset magnification showing a Pt NP aggregate.

face of the gold electrode. A magnification of Figure 4.5B shows in more detail the chain-like two-dimensional structure of the NP aggregate, which suggests diffusion

limited aggregation of the nanoparticles as will be discussed below. The question now arises whether these aggregates form in solution, or upon landing on the Au electrode.

To test the influence of the various parameters in our system on the formation of nanoparticle aggregates, we perform the NP landing experiment at the same potential and for the same length of time, but in absence of hydrazine. In the absence of electrocatalytic substrate, discrete current events were not detected.

To show the presence of Pt on the Au UME, cyclic voltammetry was performed before and after addition of Pt NPs. The dashed curve in Figure 4.6 corresponds to the surface of the gold electrode before the experiment, while the black curve is for the same surface after addition of nanoparticles. The Au UME has been clearly modified by the presence of Pt on its surface. Again the hydrogen evolution indicative of the presence of platinum is observed and a cathodic current wave corresponding to the oxygen reduction reaction on platinum is observed negative of ~ 0.6 V (as we were unable to remove this small trace of oxygen in our experiment). SEM measurements performed after the Au UME had been in contact with the nanoparticle solution show no visible aggregates on the electrode surface, as shown in Figure 4.6B and the inset magnification. We do not expect to be able to see individual particles as their diameter approaches the resolution of the scanning electron microscope. Therefore, we conclude that in the absence of hydrazine in this experiment, Pt NPs still land on the Au UME but they do not form aggregates. This experiment strongly suggests that hydrazine in fact causes the aggregation of nanoparticles in solution.

As we found that hydrazine favors the formation of aggregates of nanoparticles we have attempted to use another reducing agent that oxidizes selectively on Pt surfaces to detect landings in chronoamperometry. To this purpose, we saturated the electrolyte solution (10 mM phosphate buffer at pH 8) with hydrogen gas that would be oxidized on Pt but not on Au and repeated the experiment under the same conditions. However, we were unable to detect discrete landing events in the presence of hydrogen gas, but rather a continuous increase in anodic current, as shown in Figure 3 of Appendix B.

In Figure 4.7A three voltammograms are displayed, measured in sulfuric acid before and after addition of NPs in presence of hydrogen gas. We compare the oxidation of hydrogen on Pt NPs that were landed in presence of hydrazine (dashed) and in the presence of hydrogen (solid). The clean Au surface hardly shows any anodic current for the oxidation of hydrogen gas, while this is clearly amplified after landing Pt NPs onto the surface.

Figure 4.7B is a SEM image taken after measurements with dissolved hydrogen gas as electrocatalytic substrate. Aggregates of Pt NPs are observed, but in compar-

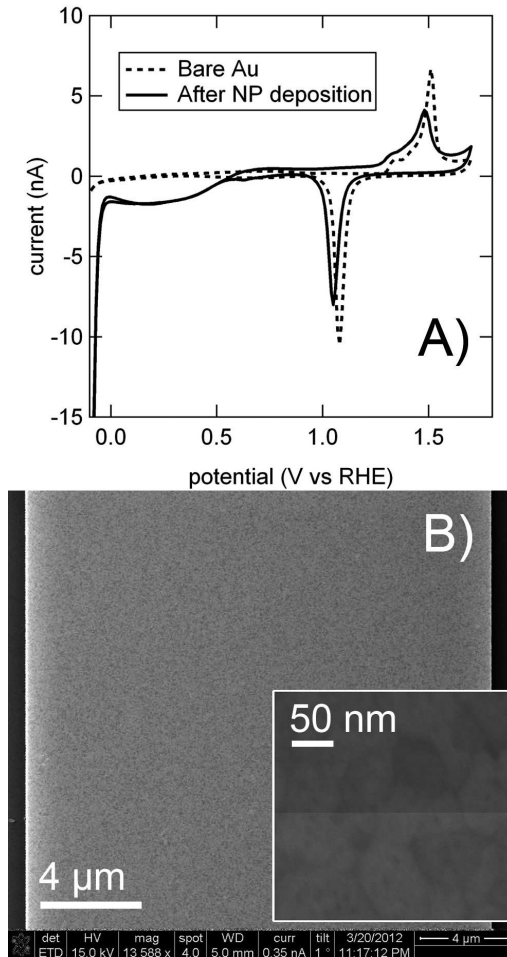


Figure 4.6: (A) Cyclic voltammety of the gold before (dotted line) and after (black line) adding Pt nanoparticles in absence of hydrazine (in this measurement a Pt flag was used as a reference and counter electrode). In the gold CV after landing events (black line) electrochemical signals due to the presence of platinum can be clearly observed: Pt catalyzed hydrogen evolution around 0 V and an amplified oxygen reduction current below 0.6 V vs RHE. (B) SEM image after landing of Pt NPs on the Au electrode in the absence of hydrazine. No aggregates of Pt nanoparticles can be observed on the electrode surface.

ison with Figure 4.6B, a much smaller amount of aggregates exists on the electrode surface. This indicates that fewer particles are aggregated when using hydrogen gas to detect particles.

While hydrogen gas also acts as a reducing agent, and would also appear to facilitate the aggregation of NPs, much fewer aggregates are found after detecting landing events with hydrogen gas than in a comparable experiment using hydrazine. However, considering we use 1 bar of hydrogen gas to saturate the solution, the hydrogen concentration will be approximately 1 mM, which is an order of magnitude lower than the hydrazine concentration used in the other landing experiments. Combined with the question of the current step amplitude, we have therefore also studied nanoparticle landings with varying hydrazine concentration.

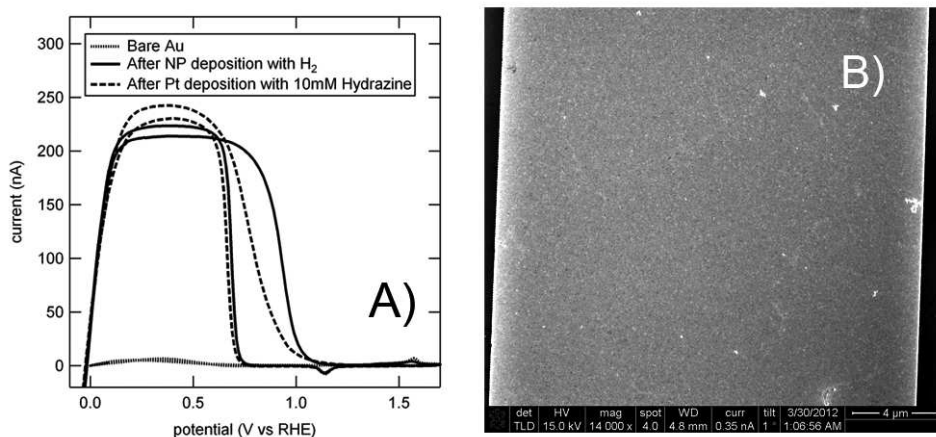


Figure 4.7: (A). Cyclic Voltammetry for the Au UME before (dotted line) and after Pt NP landing in presence of H₂ (solid line) or hydrazine (dashed line). The solution is 0.1 M H₂SO₄ saturated with H₂. (B) SEM image of the Au UME after injecting Pt NPs in the presence of H₂.

4.3.1 Influence of Hydrazine Concentration

The results of three Pt NP landing measurements performed at 0.1 mM, 1 mM and 50 mM of hydrazine are shown in Figure 4.8 and the results of 10 experiments are summarized in table 4.1. Chronoamperometric data of these experiments are shown in Figure 4 of Appendix B. Specifically, in table 4.1 the modal and mean current step heights are reported; the former should reflect the average individual particle size while the latter indicates the influence of higher current steps on the average, i.e. the amount of aggregates landing. Additionally, for clarity, the current step expected from theory for the landing of a Pt nanoparticle 3.3 nm in diameter is provided in the table as well.

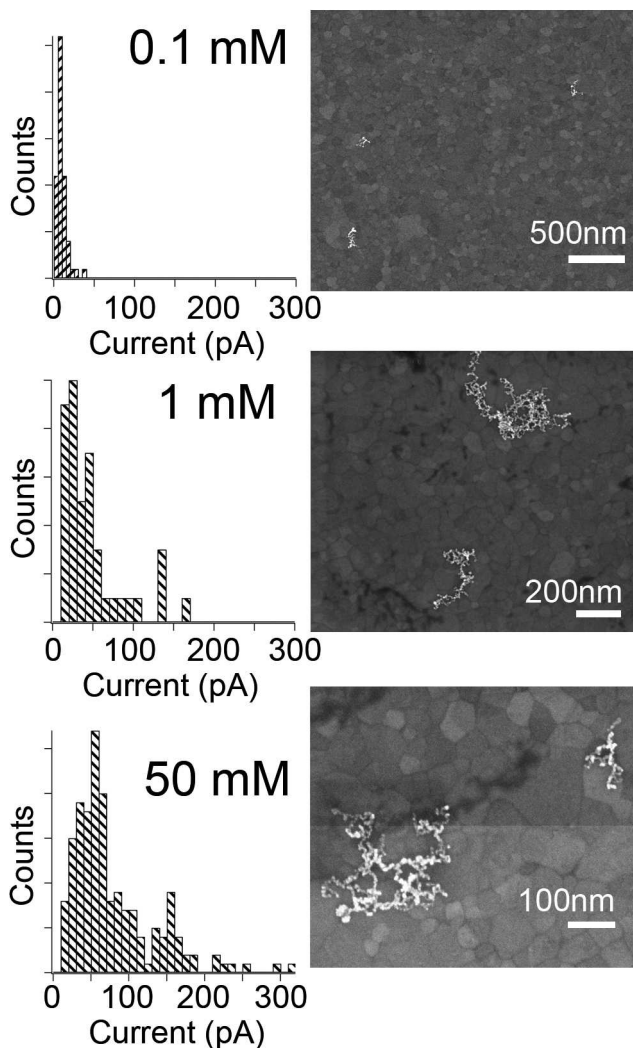


Figure 4.8: Histogram of the step height distribution, for various hydrazine concentrations, measurements were made at 0.35 V vs RHE. An increase in the mean current step height is observed with increasing hydrazine concentration.

These results do not display an obvious linear correspondence between the modes of the current step size distributions, the landing frequency, and the hydrazine concentration. Moreover, we did not find a clear trend in the relation between the mode and mean of the current step height distribution, suggesting that the degree of aggregation is not readily reproduced. Typically, we find that under seemingly identical conditions,

both the current step height and the landing frequency can vary widely. It is expected that the current steps would increase linearly with the hydrazine concentration, following equation 3 with values shown in the table. Although the results in Table 4.1 may suggest an increase in current step height with hydrazine concentration, the spread in the data is significant. When comparing the modes of the current step distribution to the expected value, the experimental values are always rather low, except in the case of very low hydrazine concentrations, when higher currents are measured. In the lower hydrazine concentration regimes, we may only detect the arrival of aggregates due to resolution limits, since landing events of individual particles would result in a near imperceptible current step on the picoampere level. Nevertheless, for the higher hydrazine concentrations currents remain lower than expected, which could be due to poisoning of the particle surface. Bard et al. [16] have reported a linear dependence of the peak current on the hydrazine concentration, but their reported experiments included only three data points over a limited hydrazine concentration (10-15 mM).

In all experiments, the SEM images show aggregated particles on the electrode surface after detecting the landings. Comparing the two extremes, after landing particles in 50 mM hydrazine there appear to be more aggregates on the surface of the electrode than in the case of 0.1 mM hydrazine. Notably, there are more large aggregates present after landing particles with a higher hydrazine concentration. To ascertain the real difference in aggregate size, however, a detailed microscopy study has yet to be performed. Increasing aggregate size would suggest a decreasing landing frequency, but this is not evident from the data in table 4.1.

Hydrazine Concentration	Modal Current Step Height	Mean Current Step Height	Landing Frequency	Expected Current Step
0.1 mM	6 pA	9 pA	0.06 Hz	0.357 pA
1 mM	23 pA	44 pA	0.06 Hz	3.57 pA
5 mM	15 pA	25 pA	0.06 Hz	17.9 pA
10 mM	25 pA	58 pA	2 Hz	35.7 pA
10 mM	12 pA	27 pA	0.46 Hz	35.7 pA
10 mM	15 pA	59 pA	0.17 Hz	35.7 pA
10 mM	18 pA	25 pA	0.25 Hz	35.7 pA
20 mM	25 pA	30 pA	0.02 Hz	71.5 pA
20 mM	35 pA	82 pA	0.05 Hz	71.5 pA
50 mM	55 pA	86 pA	0.2 Hz	179 pA

Table 4.1: Observed landing frequencies and means of the current step height distributions for various concentration of hydrazine (corresponding current-time plots are shown in Appendix B).

To evaluate the influence of the surface potential of the electrode upon the formation of aggregates, we performed the experiment in the same conditions, in absence and presence of hydrazine, at various potentials. Potentials selected were the hydrogen evolution potential, the open-circuit potential and large overpotentials where hydrazine would oxidize on Au. In all these cases we could not reproducibly measure landing events. Here we have found systematically that only when hydrazine was present in the system, nanoparticle aggregates were found after a landing experiment.

As there was a trace of oxygen in our experiments, we tested the influence of the presence of oxygen gas on the aggregation of nanoparticles. In a separate experiment, an aliquot of $100\times$ diluted NPs (10 nM) in deaerated water containing 10 mM hydrazine was freeze dried in absence of air (inside a 'glovebag' filled with Ar gas) on a piece of silicon wafer. As shown in Figure 4.9, many more and larger aggregates are visible on the silicon when hydrazine was injected when compared to samples with nanoparticles but without hydrazine (though isolated aggregates are observable in the absence of hydrogen (see Figure 4.9C)). This result indicates that also outside the electrochemical cell, in the strict absence of oxygen, the presence of hydrazine will induce the aggregation of Pt NPs.

Finally, the addition of 10 mM of hydrazine to a five-times diluted solution (~ 300 nM) of Pt NPs resulted in complete precipitation of the NPs overnight.

4.4 Discussion

In agreement with the pioneering experiments of Bard et al., injection of Pt nanoparticles into an electrochemical cell that contains hydrazine in phosphate buffer and a Au UME, discrete current steps are observed that indicate the arrival of nanoparticles that stick to the electrode surface. Although we observe a lower landing frequency than expected from theory and prior experiment, the amplitude of the current steps is in agreement with the previous experiments and with the expectations based on the model that the current peaks correspond to the diffusion-limited oxidation of hydrazine on the freshly landed Pt nanoparticle.

The reduced landing frequency could be related to a reduced effective nanoparticle concentration, related to the hydrazine-induced aggregation of particles in solution. This reasoning is corroborated by the outcome of additional experiments performed on the system. Using SEM, we observe aggregates on the surface of electrodes after Pt NP landing experiments in presence of hydrazine. We believe these aggregates are Pt because blank voltammetry on the electrode after landing experiments shows

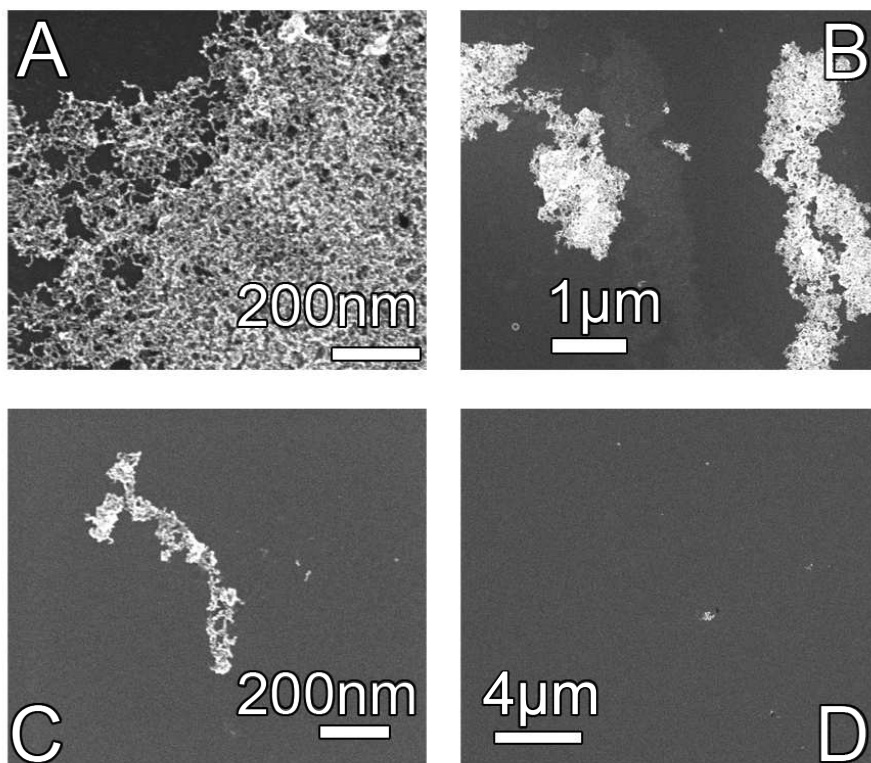


Figure 4.9: SEM images of nanoparticle aggregation observed after freeze drying 200 μL of 100x diluted Pt NPs in presence (A and B) and absence (C and D) of 10 mM hydrazine on a piece of Si in the absence of air.

Pt features. Moreover, very large aggregates are observed after drying in particles in the presence of hydrazine. The applied potential during landing experiments does not appear to influence the level of aggregation, suggesting that aggregation does not occur due to electrostatic interactions with the electrode. Instead, landing measurements in the absence of hydrazine, which are not observable electrochemically, lead to no aggregates visible under SEM. The electrode after this procedure does show a marked change in its voltammogram as visible in Figure 4.6A, indicative of Pt presence. This suggests that Pt is present in a form that we do not detect with the SEM, of which individual NPs would be the most likely candidate.

While hydrazine and hydrogen both appear to aggregate Pt NPs, the mechanism that governs this behavior is not completely clear. As oxygen gas does not play a role

in the mechanism of aggregation, this would exclude an 'electroless' reaction (i.e. oxidation of hydrazine, reduction of oxygen) on the surface of the Pt NPs as the cause of aggregation. We have examined the equilibrium potential of a flame-annealed platinum electrode in a phosphate buffer solution in the presence and absence of the reactants that surround the Pt NPs during landing experiments. As is known,[42] when Pt is in an electrolyte containing oxygen gas, it will maintain a potential of 0.9 V vs RHE, or the onset potential of the oxygen reduction reaction on Pt. If the oxygen is removed, the potential will eventually reach a value close to 0.1 V vs RHE. When hydrazine is injected to this solution the potential shifts negative to 0 V and after again adding oxygen to the system this potential is raised slightly to about 0.1 V. The presence of citrate does not influence these potentials. That is, when repeating the experiment in the presence of citrate, the potentials remain close to those found on a bare Pt electrode. This suggests that the interactions between Pt and citrate are rather weak. It has been reported previously,[43] that the tendency of dissolved citrate to replace hydrogen in the H_{UPD} of the Pt blank cyclic voltammogram is low, which means that hydrogen atoms adsorb stronger on Pt than citrate. Also, Lipkowski et al.[44] have performed chronocoulometric measurements on a Au (111) surface in presence of citrate. From the change in the surface charge they concluded that the citrate ions attach to the surface in deprotonated form, forming an overlayer on the surface that is similar to that of adsorbed sulfate from 0.2 V vs RHE.

Alternatively, hydrazine or hydrogen may displace the citrate ions, by having a stronger affinity to attach to the surface atoms. It has been noted before that Pt particles aggregate when hydrogen gas is added,[45] while it was found in early SERS studies that pyridine acts to aggregate Au particles.[46] It was suggested by Weitz et al.[47] that pyridine attaches stronger to the surface than the citrate ions do and displaces the citrate upon adsorption, as the citrate SERS signal is diminished in intensity with the onset of the signal for adsorbed pyridine. Moreover, amine groups attach to Au surface,[48, 49] similarly to the Au-thiol interaction (although the interaction is weaker). These reports in the literature focus mainly on Au, which is the more inert noble metal, but hydrazine must interact with a Pt surface in some way. Since only nitrogen gas has been found as the oxidation product of hydrazine on Pt,[33] hydrazine must adsorb or interact in undissociated form prior to oxidation on the platinum surface, and this interaction dislodges citrate from the Pt surface. In general, it seems that we must consider that the citrate shell around Pt nanoparticles is rather weakly adsorbed. We believe that a similar mechanism, as reported in our recent report,[50] utilizing H_2O_2 to remove the PVP capping-agent from Pt NPs may be operable between N_2H_4 and

Pt NPs.

The shape of the Pt NP aggregates suggests diffusion-limited aggregation, rather than reaction-limited aggregation.[51] The observed anisotropy means that nanoparticles attach with high probability when they meet. Hydrazine is a factor of ten million more concentrated in our electrolyte than the Pt NPs, so that the hydrazine-platinum interaction is not expected to be the rate limiting factor. Regarding the linear shape of the aggregates, it has been suggested by Turkevich[52] that when nanoparticle doublets are formed due to aggregation, the combined repulsive field is weakest at the ends, so that additional particles would feel lowest repulsion in a linear arrangement. This was based on the finding of two-dimensional Au NP chains formed under conditions of 'slow coagulation', namely diluted nanoparticle colloids in various concentrations of sodium perchlorate. These might be considered comparable to the conditions in our system.

If Pt NPs aggregate in the presence of hydrazine, the landing events detected in the chronoamperometry are due to the landing of both single NPs, but now at a (much) lower concentration than nominal, as well as of (large) aggregates of Pt NPs. This would explain both the lower landing frequency of the single NPs (as compared to theory) and the tailing observed in the size distributions. We cannot distinguish whether the current peaks are due to the landing of Pt NPs on the Au UME rather than on the Pt NP aggregate, as we cannot see the individual NPs in our SEM. Moreover, we do not know (how to recognize) the chronoamperometric response of the large aggregates that are observed in the SEM. Nevertheless, on the basis of our results, we must conclude that under present experimental circumstances, this experiment does not appear suited for the controlled attachment of a well-defined number of single nanoparticles on an ultramicroelectrode.

4.5 Conclusions

A recently developed method for the detection of nanoparticles[15–27] was investigated as a potential method to immobilize individual particles for the electrochemical study of their catalytic properties. This method consists of analyzing the current steps that can be measured at a Au UME when a colloid of Pt NPs is injected into an electrolyte containing hydrazine, because Pt is a better catalyst for N_2H_4 than Au. We have measured current steps attributed to the electrocatalytically amplified landing of Pt NPs on a lithographically fabricated Au UME and the modal step size is comparable to theory and prior measurements. [16] In our measurements, the landing frequency was

lower than values reported in the literature and those predicted from theory. Moreover, the current step distribution showed a long tail of large current steps. Both these findings suggest the presence of aggregated particles in solution, which lower the landing frequency by reducing the effective NP concentration and provide a higher current step upon reaching the electrode. Cyclic voltammetry measured after the landings showed a signal characteristic for Pt presence, while electron microscopy revealed that the NPs were in fact present as aggregates, after landings were performed in the presence of hydrazine or hydrogen gas. Only when particles were landed on the surface in absence of such reducing agents did we find no aggregates on the electrode surface, while CV still indicated the presence of Pt, suggesting the presence of individual particles.

We have also found that the absence of dissolved oxygen gas does not prevent the aggregation. Therefore we discard the idea that the aggregation is due to a change in the particles' surface potential when performing a catalytic oxidation in solution enabled by oxygen reduction. We tentatively ascribe the mechanism of aggregation to the interaction of these reducing agents with the NP surface that is possible owing to the weak interaction between citrate and Pt.

The finding, that landing nanoparticles in the presence of hydrazine yields NP aggregates on the surface, means that this particular method is currently not suited for the preparation of individually immobilized particles to facilitate catalysis studies at individual nanoparticles.

Bibliography

- [1] Raimondi, F.; Scherer, G. G.; Kötz, R.; Wokaun, A. *Angewandte Chemie International Edition* 2005, **44**(15), 2190–2209.
- [2] Kreibig, U.; Vollmer, M. *Optical Properties of Metal Clusters*; Springer, Heidelberg: Berlin, 1995.
- [3] Zijlstra, P.; Orrit, M. *Rep. Prog. Phys.* 2011, **74**(10), 106401.
- [4] Maillard, F.; Eikerling, M.; Cherstiouk, O. V.; Schreier, S.; Savinova, E.; Stimming, U. *Faraday Discuss.* 2004, **125**, 357–377.
- [5] Koper, M. T. M. *Nanoscale* 2011, **3**(5), 2054–2073.
- [6] Van Santen, R. A. *Acc. Chem. Res.* 2008, **42**(1), 57–66.
- [7] Somorjai, G.; Park, J. *Top. Catal.* 2008, **49**(3), 126–135.
- [8] Haruta, M. *Catal. Today* 1997, **36**(1), 153–166.
- [9] Buurmans, I. L. C.; Ruiz-Martínez, J.; Knowles, W. V.; van der Beek, D.; Bergwerff, J. A.; Vogt, E. T. C.; Weckhuysen, B. M. *Nat Chem* 2011, **3**(11), 862–867.
- [10] Claessen, V. I.; Engelkamp, H.; Christianen, P. C.; Maan, J. C.; Nolte, R. J.; Blank, K.; Rowan, A. E. *Annu. Rev. Anal. Chem.* 2010, **3**(1), 319–340.
- [11] Chen, S.; Kucernak, A. *J. Phys. Chem. B* 2004, **108**(10), 3262–3276.
- [12] Chen, S.; Kucernak, A. *J. Phys. Chem. B* 2004, **108**(37), 13984–13994.
- [13] Lai, S. C. S.; Dudin, P. V.; Macpherson, J. V.; Unwin, P. R. *J. Am. Chem. Soc.* 2011, **133**(28), 10744–10747.
- [14] Hoeben, F. J. M.; Meijer, F. S.; Dekker, C.; Albracht, S. P. J.; Heering, H. A.; Lemay, S. G. *ACS Nano* 2008, **2**(12), 2497–2504.
- [15] Xiao, X.; Bard, A. J. *J. Am. Chem. Soc.* 2007, **129**(31), 9610.
- [16] Xiao, X.; Fan, F.-R. F.; Zhou, J.; Bard, A. J. *J. Am. Chem. Soc.* 2008, **130**(49), 16669–16677.
- [17] Xiao, X.; Pan, S.; Jang, J. S.; Fan, F.-R. F.; Bard, A. J. *J. Phys. Chem. C* 2009, **113**(33), 14978–14982.
- [18] Kwon, S. J.; Zhou, H.; Fan, F.-R. F.; Vorobyev, V.; Zhang, B.; Bard, A. J. *Phys. Chem. Chem. Phys.* 2011, **13**(12), 5394–5402.
- [19] Kwon, S. J.; Fan, F.-R. F.; Bard, A. J. *J. Am. Chem. Soc.* 2010, **132**(38), 13165–13167.
- [20] Zhou, H.; Fan, F.-R. F.; Bard, A. J. *J. Phys. Chem. Lett.* 2010, **1**(18), 2671–2674.
- [21] Zhou, Y.-G.; Rees, N. V.; Compton, R. G. *Angewandte Chemie International Edition* 2011, **50**(18), 4219–4221.
- [22] Zhou, Y.-G.; Rees, N. V.; Compton, R. G. *Chem. Phys. Lett.* 2011, **511**(4-6), 183–186.
- [23] Zhou, Y.-G.; Rees, N. V.; Compton, R. G. *ChemPhysChem* 2011, **12**(11), 2085–2087.
- [24] Zhou, Y.-G.; Rees, N. V.; Pillay, J.; Tshikhudo, R.; Vilakazi, S.; Compton, R. G. *Chem. Commun.* 2012, **48**(2), 224–226.
- [25] Zhou, Y.-G.; Rees, N. V.; Compton, R. G. *Chem. Commun.* 2012, **48**(19), 2510–2512.
- [26] Zhou, Y.-G.; Rees, N. V.; Compton, R. G. *Chem. Phys. Lett.* 2011, **514**(4-6), 291–293.
- [27] Rees, N. V.; Zhou, Y.-G.; Compton, R. G. *ChemPhysChem* 2011, **12**(9), 1645–1647.
- [28] Lin, C.-S.; Khan, M. R.; Lin, S. D. *J. Colloid Interface Sci.* 2005, **287**(1), 366–369.

- [29] Grobelny, J.; DelRio, F. W.; Pradeep, N.; Kim, D.-I.; Hackley, V. A.; Cook, R. F. In *Methods in Molecular Biology*; Walker, J., Ed., Vol. 697 of *Methods in Molecular Biology*; Springer, Heidelberg, 2009; pages 71–82.
- [30] Horcas, I.; Fernandez, R.; Gomez-Rodriguez, J.; Colchero, J.; Gomez-Herrero, J.; Baro, A. *Rev. Sci. Instrum.* 2007, *78*, 013705.
- [31] Jentys, A. *Phys. Chem. Chem. Phys.* 1999, *1*(17), 4059–4063.
- [32] Patterson, A. L. *Phys. Rev.* 1939, *56*(10), 978–982.
- [33] Rosca, V.; Koper, M. T. M. *Electrochim. Acta* 2008, *53*(16), 5199–5205.
- [34] Aldous, L.; Compton, R. G. *Phys. Chem. Chem. Phys.* 2011, *13*(12), 5279–5287.
- [35] Dudin, P. V.; Unwin, P. R.; Macpherson, J. V. *Phys. Chem. Chem. Phys.* 2011, *13*(38), 17146–17152.
- [36] Alvarez-Ruiz, B.; Gomez, R.; Orts, J. M.; Feliu, J. M. *J. Electrochem. Soc.* 2002, *149*(3), D35–D45.
- [37] Bard, A. J.; Faulkner, L. R. *Electrochemical Methods, Fundamentals and Applications*; John Wiley & Sons: New York, 2 ed., 2001.
- [38] Kleijn, S. E. F.; Yanson, A. I.; Koper, M. T. M. *J. Electroanal. Chem.* 2012, *666*(0), 19–24.
- [39] Zare, H. R.; Nasirizadeh, N. *Electroanalysis* 2006, *18*(5), 507–512.
- [40] Ardakani, M. M.; Karimi, M.; M.M., Z.; Mirdehghan, S. *Int. J. Electrochem. Sci.* 2008, *3*, 246 – 258.
- [41] Angerstein-Kozłowska, H.; Conway, B. E.; Barnett, B.; Mozota, J. *J. Electroanal. Chem. Interfac. Electrochem.* 1979, *100*, 417–446.
- [42] Wroblowa, H.; Rao, M. L. B.; Damjanovic, A.; Bockris, J. O. *J. Electroanal. Chem. Interfac. Electrochem.* 1967, *15*(0), 139–150.
- [43] González-Peña, O. I.; Chapman, T. W.; Vong, Y. M.; Antaño López, R. *Electrochim. Acta* 2008, *53*(17), 5549–5554.
- [44] Kunze, J.; Burgess, I.; Nichols, R.; Buess-Herman, C.; Lipkowski, J. *J. Electroanal. Chem.* 2007, *599*(2), 147–159.
- [45] Furlong, D. N.; Launikonis, A.; Sasse, W. H. F.; Sanders, J. V. *Journal of the Chemical Society, Faraday Transactions 1: Physical Chemistry in Condensed Phases* 1984, *80*(3), 571–588.
- [46] Creighton, J. A.; Blatchford, C. G.; Albrecht, M. G. *Journal of the Chemical Society, Faraday Transactions 2: Molecular and Chemical Physics* 1979, *75*, 790–798.
- [47] Weitz, D. A.; Lin, M. Y.; Sandroff, C. J. *Surf. Sci.* 1985, *158*, 147–164.
- [48] Venkataraman, L.; Klare, J. E.; Tam, I. W.; Nuckolls, C.; Hybertsen, M. S.; Steigerwald, M. L. *Nano Lett.* 2006, *6*(3), 458–462.
- [49] Leff, D. V.; Brandt, L.; Heath, J. R. *Langmuir* 1996, *12*(20), 4723–4730.
- [50] Monzó, J.; Koper, M. T. M.; Rodriguez, P. *ChemPhysChem* 2012, *13*(3), 709–715.
- [51] Lin, M. Y.; Lindsay, H. M.; Weitz, D. A.; Ball, R. C.; Klein, R.; Meakin, P. *Nature* 1989, *339*(6223), 360–362.
- [52] Enüstün, B. V.; Turkevich, J. *J. Am. Chem. Soc.* 1963, *85*(21), 3317–3328.

5

Landing and Catalytic Characterization of Individual Nanoparticles on Electrode Surfaces

Abstract

We demonstrate a novel and versatile pipet-based approach to study the landing of individual nanoparticles (NPs) on various electrode materials, without any need for encapsulation or fabrication of complex substrate electrode structures, providing great flexibility with respect to electrode materials. Due to the small electrode areas defined by the pipet dimensions, the background current is low, allowing for the detection of minute current signals with good time resolution. This approach was used to characterize the potential-dependent activity of Au NPs and to measure the catalytic activity of a single NP on a TEM grid, combining electrochemical and physical characterization at the single NP level for the first time. Such measurements open up the possibility of studying the relation between size and activity of catalyst particles unambiguously.

5.1 Introduction

Metal nanoparticles (NPs) have been extensively studied as electrocatalysts in numerous fields and applications.[1–3] A key aspect of NPs is their size- and structure-dependent reactivity,[2] which is often inferred from ‘top-down’ studies of ensembles of catalytic NPs. However, due to the inherent variance in NP size and shape, only average reactivity trends may be obtained in this way. Even when one can work with a narrow size distribution, subtle effects may substantially alter reactivity. Indeed, we have shown in a previous study that ostensibly similar NPs can have very different reactivity due to subtle variations in morphology.[4] Therefore, to truly understand NP reactivity on a fundamental level, it is imperative to study single NPs. While such an investigation is demanding, as it requires placing, locating and characterizing a single NP, a few experimental studies have been reported.[4–13] Single NP studies are further challenging due to the need for high accuracy measurement of the small (current) signals with reasonable bandwidth.[13–15]

A recent innovative method to electrochemically detect individual NPs[7–12] focuses on NPs that are dispersed in an electrolyte solution, that can diffuse to, and land on, an electrode surface held at a potential where a reaction occurs on the catalytic NP but not on the inert collector electrode. Consequently, arrival of a NP at the electrode surface results in an increase in current due to the NP reaction, which can be a reaction of a species in solution[7] or the oxidation of the NP itself.[10] In order to limit the number of NPs landing and minimize the background current, a collector electrode of small area is needed. The preparation of such ultra-microelectrodes (UMEs) greatly limits the choices of substrate material, since not every material (particularly material of practical importance) can be shaped to micro- or nanoscale dimension, and even when the material can be encapsulated, electrode preparation requires considerable time and effort.[16–18] A typical UME (~5 μm diameter) often still shows a considerable background signal compared to the electrochemical signal from the NP reaction.[7–12] Consequently, only large current signals (often resulting from mass transport limited reactions)[7, 9] can be detected, and obtaining an entire current-voltage response at an individual NP has so far proved impossible. Furthermore, subsequent characterization of immobilized NPs has proven very challenging.[17]

In this chapter, we demonstrate the study of single NP reactivity by employing scanning electrochemical cell microscopy (SECCM) to select and isolate a small area on a collector electrode, of any kind of material, and to land, detect and characterize individual NPs. The experimental set-up is schematically depicted in Figure 5.1a and

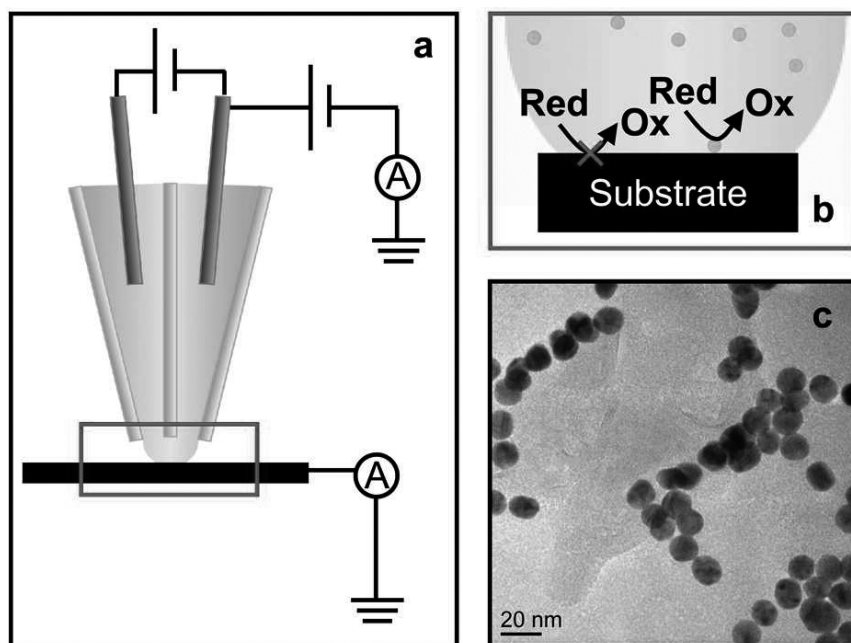


Figure 5.1: (a) Schematic of the experimental setup. (b) Schematic of the liquid meniscus constituting the electrochemical cell. The substrate is held at a potential where a reaction occurs on the catalytic AuNP, but not on the collector electrode. (c) TEM image of the AuNPs used in this study.

b and described in full in the Experimental section. In short, a dual-channel (theta) pipet with a sharp point of approximately $1.5 \mu\text{m}$ diameter was filled with an electrolyte solution of interest (containing $\sim 70 \text{ pM}$ citrate-capped gold NPs (AuNPs), $10\text{-}20 \text{ nm}$ diameter,[19, 20] Figure 5.1c) and two palladium-hydrogen (Pd-H_2 ; $E^0 = 50 \text{ mV}$ vs. reversible hydrogen electrode, RHE)[4] quasi-reference counter electrodes (QRCEs), both held at the same potential. All potentials throughout this study are reported relative to the RHE. The use of a theta pipet allowed us to monitor the size of the liquid meniscus formed at the end of the pipet by measuring the ionic current between the two QRCEs across the meniscus when a small potential bias was applied between them. Furthermore, the migration rate of charged species can be controlled by the bias potential applied between the QRCEs,[21] but this option was not employed in this work. The pipet was mounted on a piezoelectric positioning system and slowly lowered towards the substrate, which was held at ground, while the current flowing through the substrate was monitored continuously. Upon contact of the liquid meniscus at the end

of the pipet with the substrate, a current spike was observed at the substrate due to the formation of the electrical double layer. This was used to automatically halt the approach so that the pipet was held in place for the duration of the experiment. The resulting meniscus between the pipet and substrate constitutes a micro- or nanoscopic electrochemical cell with the wetted area of the substrate as working electrode, which experiences a potential of the same magnitude but opposite sign as the potential applied to the QRCEs. In this approach, we isolate an area on the working electrode by limiting the electrolyte contact (rather than by decreasing the size of the working electrode, as in previous studies[7–12]), which results in at least three main advantages. First, this allows the use of a wide range of electrode materials, size and morphologies, as no traditional UME manufacture is required, instead relying on facile micro- or nanopipet preparation. Second, we can make and break the cell at will on a specific site on the electrode surface (on a millisecond timescale if needed), by simply moving the pipet away from or towards the substrate. This is particularly beneficial if one wishes to land single NPs in a predetermined pattern. Finally, the working electrode area in this pipet-based approach is determined by the size of the pipet,[21, 22] which can be routinely prepared to be smaller than a typical UME (of several micrometers in diameter), down to <200 nm.[23] Such ultra-small surface areas result in a significant decrease in background current (by two orders of magnitude) compared to the UMEs presently used, allowing detection of much smaller currents from the NP reaction itself.

5.2 Experimental

5.2.1 Setup

The experiments were conducted on a scanning electrochemical cell microscopy (SECCM) [24] set-up.[22] The pipet was a dual channel probe pulled from a borosilicate theta glass capillary (TGC150-10, Harvard Apparatus) using a CO₂-laser puller (P-2000, Sutter Instruments) to a sharp taper of approximately 1.5 μm total diameter (ca. 700 nm per channel) at the end. The resulting pipet tip was silanized with dichlorodimethylsilane (Si(CH₃)₂Cl₂, Acros Organics, 99+%) to render the outer wall hydrophobic. Each channel was filled with the electrolyte solution of interest. A palladium-hydrogen (Pd–H₂) quasi-reference counter electrode (QRCE), prepared by evolving hydrogen on a palladium wire (Mateck, 99.9%) in 0.1 M H₂SO₄ (Aldrich, 99.999%) until saturated, was inserted into each channel, and both Pd–H₂ QRCEs were held at the same potential. The pipet was mounted on a high-dynamic z-piezoelectric positioner

(P-753.3CD LISA, PhysikInstrumente), while the sample was mounted on a high-precision xy-piezoelectric stage (P-622.1CL PIHera, PhysikInstrumente or P-622.2CL PIHera, PhysikInstrumente). Rough positioning of the pipet and of the sample was aided by two digital CMOS cameras (PL-B776U and PL-B782U, PixeLINK) and a 3-axis micropositioner (Newport), allowing lateral pipet positioning within ca. 10 μm of the point of interest.[4] The entire assembly was installed in a Faraday cage. The pipet was slowly moved to the substrate surface, and the motion was halted when meniscus contact was established, typically evident from a current spike flowing through the substrate due to double layer charging. Current measurements were performed using high sensitivity home-built current to voltage converters. Tip and sample positioning and data acquisition were performed using a FPGA card (PCI-7830R, National Instruments) with a LabVIEW 9.0 interface. Two electrolyte solutions were employed in this study. For the studies on HOPG (ZYA-grade, NT-MDT), a 10 mM phosphate buffer solution (pH 7.2) was prepared by diluting stock phosphate buffer solution (Aldrich) with ultra-pure water (Purite Select system, resistivity 18.2 $\text{M}\Omega\text{ cm}$ at 25 $^{\circ}\text{C}$), to which ~ 70 pM AuNPs was added. For the studies on the carbon coated Cu TEM grid (carbon film on 400 copper mesh), a 50 mM citrate buffer solution (pH ~ 4.5) was prepared from 25 mM citric acid (Aldrich, $>99.5\%$) and 25 mM trisodium citrate (Aldrich, USP testing standard) and ultra-pure water, to which 2 mM hydrazine sulfate (Sigma Aldrich, ACS reagent, $> 99.0\%$) and ~ 70 pM AuNPs was added. The TEM grids were treated in an oxygen plasma (Emiteck K1050X Plasma Etcher/Asher/Cleaner) at 100 W for 15 seconds before use to increase the hydrophilicity of the carbon film.

For the landing experiments on the carbon coated Cu TEM grid, the pipet was located on a specific section (square region between the mesh) of the grid using the camera positioning system. To aid locating the particle, only one single NP was deposited per section.

TEM images were recorded on Jeol 2000FX Transmission Electron Microscope at 200 keV accelerating voltage.

5.2.2 Gold nanoparticle synthesis

Gold nanoparticles were prepared following a modified method originally introduced by Turkevich.[19, 20] All glassware used in this procedure was cleaned with fresh aqua regia solution (3:1 concentrated hydrochloric acid (Fischer, lab reagent grade)/ concentrated nitric acid (Aldrich, Volumetric standard)) and thoroughly rinsed with ultra-pure water. In a typical synthesis, 8 ml of 1 mM HAuCl_4 (Aldrich, 99.999%) solution was brought to 85 $^{\circ}\text{C}$ and stirred vigorously. 0.8 ml of 38.8 mM trisodium citrate (Aldrich,

USP testing standard) was rapidly added to the vortex of this solution. The solution was held at 85 °C for 10 minutes, then allowed to cool to room temperature with continuous stirring for ~20 minutes. The solution was stored at 4 °C until use. Before use, the nanoparticle solution was stirred in an ultra-sonic bath for at least 30 minutes to obtain a well-dispersed, homogenous solution. TEM measurements show that this results in particles of 10-20 diameter, in agreement with literature values.³

The NP concentration can be estimated as follows: Based on spherical NPs with an average diameter of 16 nm, the mass can be calculated to be 4.14×10^{-17} g/NP, based on a volume of 2.14×10^{-18} cm³/NP and the bulk density of gold (19.3 g cm⁻³). Comparing the average mass of one AuNP with the total mass of Au³⁺ precursor (1.58×10^{-3} g Au³⁺), and assuming full reduction of Au³⁺ to AuNPs, this yields a stock solution 3.81×10^{13} AuNPs in 8.8 ml, or, equivalently, 7.21 nM AuNPs.

5.3 Results

To demonstrate the flexibility of the pipet-based approach, we have landed AuNPs from an aerated 5 mM phosphate buffer solution (pH 7.2) on highly oriented pyrolytic graphite (HOPG) at various potentials. HOPG is an interesting substrate as it serves as a model for novel sp² carbon materials and there has been recent debate on the active sites for electron transfer.^[22] Furthermore, the surface of HOPG is easily refreshed (through cleaving with adhesive tape) and has low background currents, making it an attractive collector electrode for NP landing experiments.

Typical current-time plots obtained for the landing of AuNPs on HOPG at various potentials (Figure 5.2a-d) show a few general trends. Initially, as the pipet is suspended in air, the recorded substrate current is zero. Once the liquid meniscus is brought into contact with the substrate, the electronic circuit is closed, leading to an initial current spike at all potentials (e.g. at ~90 s. in Figure 5.2a). This current spike can be attributed to the formation of the electric double layer on the HOPG substrate, and its direction is indicative of the potential applied to the substrate relative to its potential of zero total charge (pztc). Given the flexibility of this technique, this finding also opens up possibilities to quickly probe the pztc of a material at the nanoscale under various experimental conditions. Once the meniscus is in contact with the substrate, discrete current steps were observed at potentials at which electrochemical reactions occur on Au but not on HOPG, indicating the arrival of distinct AuNPs. Three potential regimes can be distinguished: at potentials above 1 V (such as at 1.2 V, Figure 5.2a), the current steps are positive. At potentials below 0.15 V (Figure 5.2c and d), the current

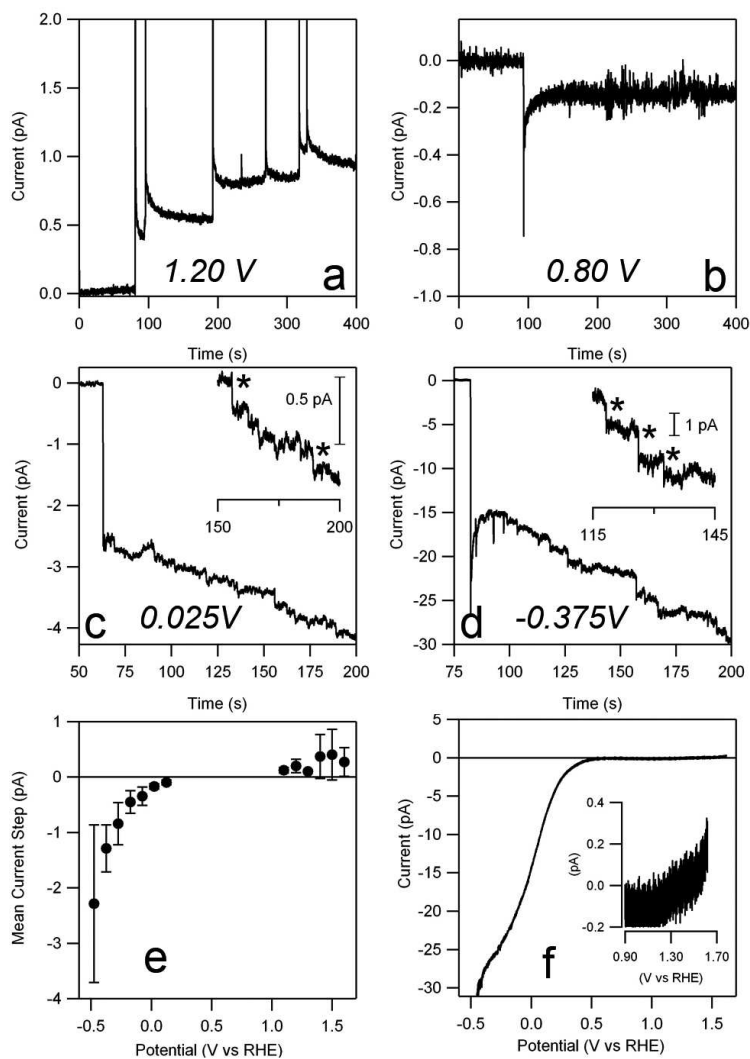


Figure 5.2: (a-d) Current-time plots showing the landing of the pipet meniscus (initial spike) and AuNPs (subsequent steps) at selected potentials. (e) Mean current step height determined as a function of substrate potential. Error bars denote 2σ . (f) Linear sweep voltammogram (50 mV s^{-1}) of Au in 5 mM phosphate buffer, measured using a pipet of $1.5 \mu\text{m}$ diameter.

steps are negative, and the magnitude increases with more cathodic potential. Finally, at intermediate potentials (Figure 5.2b), no current steps are observed; instead the current-time profile shows a constant background. To understand this current-potential behavior in more detail, Figure 5.2e shows the mean values of the current steps as a function of substrate potential. There is a clear and strong potential dependence, similar to that of a bulk polycrystalline Au electrode measured using the same pipet setup (Figure 5.2f), although the current densities on the AuNPs are higher due to the much increased mass transport rate at nanostructures in the SECCM set-up.[23] At low potentials (< 0.15 V), the observed current steps can be ascribed to the oxygen reduction reaction (ORR). The onset potential appears to be at a higher overpotential than on bulk Au (~ 0.4 V), but the apparent difference is likely due to the fact that the current steps at lower overpotential are not sufficiently large to be detected, although we also cannot rule out some kinetic effects at the smaller particle due to the greatly enhanced mass transport rate. At intermediate potentials, in the double layer region of Au, no current steps are observed, as no reaction takes place on the AuNP upon landing. This also indicates that the landing of NPs does not disturb the HOPG double layer significantly, while the charging of the particles themselves was not detected. Finally, at potentials positive of 1.10 V, oxidative current steps are observed. Typically, surface oxide formation takes place in this potential range. However, as this process is limited by the Au surface area, it would lead to current spikes with a finite charge (~ 5 fC for a 20 nm diameter AuNP),[25] rather than current steps. As the oxidation of carbonaceous species is often found to take place in the Au surface oxidation region,[26] we tentatively attribute the oxidative current steps to the oxidation of residual carbonaceous species in solution, as no special effort was taken to purify the solution and reagents.

The excellent signal to noise ratio in these experiments allowed ready analysis of the frequency at which AuNPs land on the HOPG substrate, as a function of the substrate potential (Figure 5.3). These frequency values were obtained by dividing the counted current steps (marked with an asterisk in insets of Figure 5.2c and 5.2d) by the total runtime of the experiment. At the extreme potentials, the experimentally observed frequency is ~ 0.05 s⁻¹, lower than the theoretical value of 0.4 s⁻¹ predicted by diffusion laws: The theoretical landing frequency of AuNPs at the electrode can be estimated based on equations for a purely diffusive NP flux, based on Fick's diffusion laws.[27] The flux of NPs (j_{NP} , expressed in NP s⁻¹) down the pipet to the substrate electrode is ca. 10% of the flux from an infinite solution towards a disc electrode of the same diameter.[21] The diffusive flux to a disc electrode is given by equation 5.1:

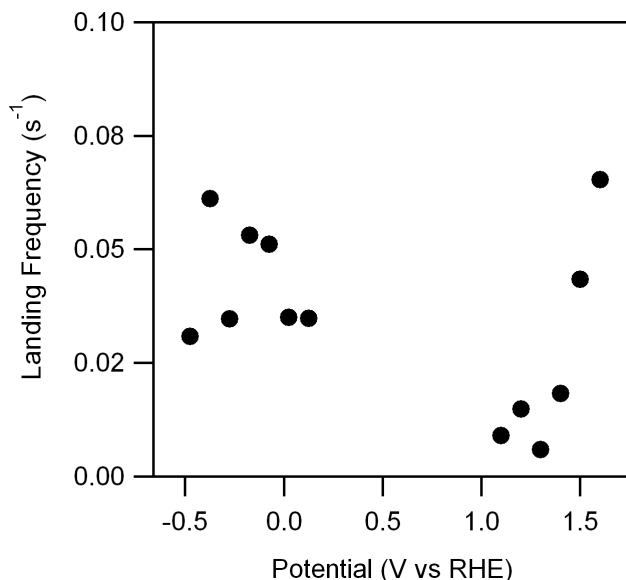


Figure 5.3: Frequency of current steps for landed NPs measured at different potentials.

$$j_{NP} = 4D_{NP}C_{NP}N_A r_{disc} \quad (5.1)$$

In this equation N_A is Avogadro's constant ($N_A = 6.02 \times 10^{23} \text{ mol}^{-1}$), r_{disc} is the radius of the disc, and D_{NP} and C_{NP} are the diffusion coefficient of AuNPs and its concentration in solution, respectively. The diffusion coefficient of NPs with radius r_{NP} can be determined from the Stokes-Einstein relation (equation 5.2):

$$D_{NP} = \frac{k_B T}{6\pi\eta r_{NP}} \quad (5.2)$$

in which k_B is the Boltzmann constant ($k_B = 1.381 \times 10^{-23} \text{ J K}^{-1}$) and η is the dynamic viscosity of water ($\eta = 8.90 \times 10^{-4} \text{ Pa s}$ at $25 \text{ }^\circ\text{C}$). For a 16 nm NP, equation 2 yields a diffusion coefficient of $D_{NP} = 3.1 \times 10^{-7} \text{ cm}^2 \text{ s}^{-1}$. Using this value, we obtain a diffusive flux to a disc with a radius of 750 nm (corresponding to the radius of the pipets employed) of $j_{NP} = 3.8 \text{ NP s}^{-1}$, from which we can estimate the theoretical diffusive flux in pipet-based set-up in this study to be $j_{NP} \approx 0.4 \text{ NP s}^{-1}$. Experimental landing frequencies have been consistently reported to be lower than predicted from theoretical considerations.[8, 10, 28] Although various explanations have been forwarded to account for this discrepancy, the issue is not yet well understood. Finally, it

should be noted that at moderately high potentials (between 1.0 and 1.5 V), the landing frequency lies below the average. As the magnitude of the current steps is very small in this potential region, we ascribe the diminished observed frequency to the fact that only particularly large or active particles show a catalytic response large enough to be detected, and thus the observed landing frequency may not represent the 'true' landing frequency.

A particularly exciting substrate on which to perform NP landing experiments is a transmission electron microscope (TEM) grid, as this allows characterization of the deposited NPs to fully resolve structure-activity relationships at the level of a single NP. To demonstrate this capability, we have landed AuNPs on a carbon coated TEM grid by measuring the oxidation of 2 mM hydrazine in a 50 mM citrate buffer. Although employing hydrazine with citrate-capped NPs gave rise to some complications (*vide infra*), it is a good model system for an electrocatalytic reaction, as it is sufficiently facile to reach mass transport limited conditions. Typical landing events, in which the TEM grid was held at 1.25 V (potential close to the mass transport limited regime), are shown in Figure 5.4a. As can be seen, in these experiments, establishing the contact of the meniscus with the carbon film on the TEM grid typically coincides with the landing of the first AuNP, giving rise to current steps of ~40 – 80 pA. The magnitudes of these steps are in good agreement with the current predicted for the diffusion-limited current based on radial diffusion to a sphere with radius r on a plane, as given by equation 5.3.[7]

$$i_{lim} = 4\pi(\ln 2)nFDCr \quad (5.3)$$

Here n is the number of electrons transferred per hydrazine molecule (4), F is the Faraday constant ($9.649 \times 10^4 \text{ C mol}^{-1}$), C is the hydrazine concentration ($2 \mu\text{mol cm}^{-3}$), and D is the diffusion coefficient of hydrazine. A wide range of diffusion coefficients for hydrazine have been reported, typically $0.5\text{--}1.5 \times 10^{-5} \text{ cm}^2 \text{ s}^{-1}$. [29–31] In this case, we find the best correspondence between the spread in current step magnitudes and AuNP size distribution for $D \approx 1.2 \times 10^{-5} \text{ cm}^2 \text{ s}^{-1}$, a value well within the reported range and typical for small molecules.

The landing frequency was low, with up to tens of seconds between successive landing events, attributable to a much lowered concentration of free AuNPs in solution due to extensive aggregation.[28] This aggregation was observed qualitatively by the color change of a fairly concentrated AuNP solution upon addition of small amounts of hydrazine from pink to gray, followed by AuNP precipitation. Nonetheless, as Figure 5.4 shows, it is still possible to land single AuNPs without interference of aggregates

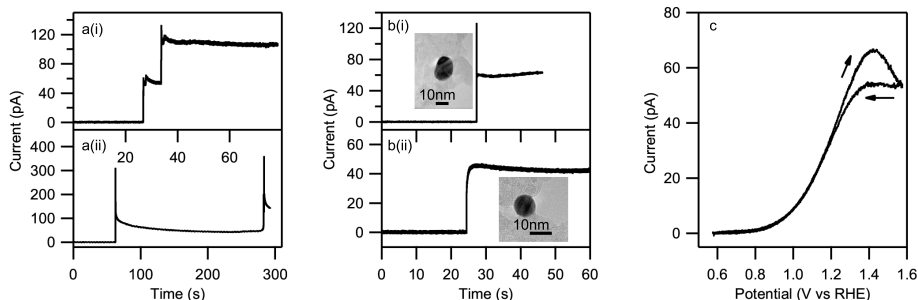


Figure 5.4: (a) AuNPs landing on a carbon coated Cu TEM grid (at 1.25 V) in presence of N_2H_4 . (b) Landing events of individual AuNPs, with the same AuNP imaged by TEM afterwards. (c) CV (200 mV s^{-1}) measured at the individual AuNP shown in (b(i)).

landing. This may be due to the fact that the opening at the end of each barrel of the pipet ($\sim 700 \text{ nm}$) may be too small for aggregates to pass, thus acting as a particle size filter. The long period between events allowed electrochemical characterization of the AuNP and then retraction of the pipet, leaving the initial AuNP on the TEM grid for subsequent visualization without further AuNPs landing. This made it possible to correlate the electrochemical (current) with the physical properties of the AuNP. Examples are shown in Figure 5.4b: two separate landing experiments were performed with current steps of 40 and 60 pA. Visualizing these same particles with TEM, it can be seen that this difference is directly related to the size difference between the two AuNPs: the current step of 40 pA originating from a $\sim 10 \text{ nm}$ NP, while the current of 60 pA originates from a $\sim 15 \text{ nm}$ NP, in good agreement with equation (1). This agreement indicates directly that mass transport controls the reactivity of single AuNPs at this potential, and, moreover, the scaling of the current with particle radius confirms that mass transport to a single particle is predominantly radial in nature.

Finally, we were able to sweep the substrate potential after the initial landing event to record a full CV of a single AuNP before retracting the pipet. A CV of the AuNP in Figure 5.4b(ii) is shown in Figure 5.4c. The recorded CV shows an onset potential of $\sim 0.8 \text{ V}$, in good agreement with those reported for hydrazine oxidation on gold electrodes.[32] The oxidation wave is somewhat drawn out compared to CVs recorded on macroscopic Au electrodes,[32] which can be fully ascribed to the increased mass transport coefficient ($\sim 6 \text{ cm s}^{-1}$, c.f. $\sim 10^{-3} \text{ cm s}^{-1}$ for macroscopic systems) in this configuration.[22]

5.4 Conclusion

In conclusion, we have demonstrated a SECCM-based approach to land and characterize single NPs on electrodes with minimal electrode preparation and the ability to select the measurement location. The results obtained with this approach are consistent with previous NP landing studies on UMEs[7–12] but with enhanced sensitivity due to the lower background signals owing to a smaller contact area. As highlighted herein, this pipet-based approach eliminates the need for UME fabrication, and a wide variety of substrates can be investigated. A particularly exciting application has been to use this pipet-based approach to study NP reactivity on a TEM grid, allowing the complete unambiguous correlation of physical and electrochemical properties at a single NP level for the first time. Apart from studying particle size and shape effects, the wide range of substrates that can be studied also opens up the possibility to study substrate effects on electrocatalytic reactions, an aspect which is not yet well-understood. We believe that these prospects make this pipet-based approach particularly powerful for further understanding and resolving nanoparticle reactivity.

Bibliography

- [1] Somorjai, G. A. *Science* 1985, 227(4689), 902–908.
- [2] Chen, A.; Holt-Hindle, P. *Chem. Rev.* 2010, 110(6), 3767–3804.
- [3] Koper, M. T. M. *Nanoscale* 2011, 3, 2054–2073.
- [4] Lai, S. C.; Dudin, P. V.; Macpherson, J. V.; Unwin, P. R. *J. Am. Chem. Soc.* 2011, 133(28), 10744–10747.
- [5] Meier, J.; Friedrich, K. A.; Stimming, U. *Faraday Discuss.* 2002, 121, 365–372.
- [6] Krapf, D.; Wu, M.-Y.; Smeets, R. M. M.; Zandbergen, H. W.; Dekker, C.; Lemay, S. G. *Nano Lett.* 2006, 6(1), 105–109.
- [7] Xiao, X.; Bard, A. J. *J. Am. Chem. Soc.* 2007, 129(31), 9610–9612.
- [8] Xiao, X.; Fan, F.-R. F.; Zhou, J.; Bard, A. J. *J. Am. Chem. Soc.* 2008, 130(49), 16669–16677.
- [9] Bard, A. J.; Zhou, H.; Kwon, S. J. *Isr. J. Chem.* 2010, 50(3), 267–276.
- [10] Zhou, Y.-G.; Rees, N. V.; Compton, R. G. *Angew. Chem., Int. Ed.* 2011, 50(18), 4219–4221.
- [11] Kwon, S. J.; Bard, A. J. *J. Am. Chem. Soc.* 2012, 134(16), 7102–7108.
- [12] Rees, N. V.; Zhou, Y.-G.; Compton, R. G. *RSC Adv.* 2012, 2, 379–384.
- [13] Chen, S.; Kucernak, A. *J. Phys. Chem. B* 2003, 107(33), 8392–8402.
- [14] Eikerling, M.; Meier, J.; Stimming, U. *Zeitschrift für Physikalische Chemie* 2003, 217(4-2003), 395–414.
- [15] Hoeben, F. J. M.; Meijer, F. S.; Dekker, C.; Albracht, S. P. J.; Heering, H. A.; Lemay, S. G. *ACS Nano* 2008, 2(12), 2497–2504.
- [16] Cox, J. T.; Zhang, B. *Annu. Rev. Anal. Chem.* 2012, 5(1), 253–272.
- [17] Li, Y.; Cox, J. T.; Zhang, B. *J. Am. Chem. Soc.* 2010, 132(9), 3047–3054.
- [18] Kleijn, S. E.; Yanson, A. I.; Koper, M. T. *J. Electroanal. Chem.* 2012, 666(0), 19 – 24.
- [19] Turkevich, J.; Stevenson, P. C.; Hillier, J. *Discuss. Faraday Soc.* 1951, 11, 55–75.
- [20] Frens, G. *Nature Physical Science* 1973, 241, 20–22.
- [21] Snowden, M. E.; Güell, A. G.; Lai, S. C. S.; McKelvey, K.; Ebejer, N.; O'Connell, M. A.; Colburn, A. W.; Unwin, P. R. *Anal. Chem.* 2012, 84(5), 2483–2491.
- [22] Lai, S. C. S.; Patel, A. N.; McKelvey, K.; Unwin, P. R. *Angew. Chem.* 2012, 124(22), 5501–5504.
- [23] Güell, A. G.; Ebejer, N.; Snowden, M. E.; McKelvey, K.; Macpherson, J. V.; Unwin, P. R. *Proc. Natl. Acad. Sci. USA* 2012, 109(29), 11487–11492.
- [24] Ebejer, N.; Schnippering, M.; Colburn, A. W.; Edwards, M. A.; Unwin, P. R. *Anal. Chem.* 2010, 82(22), 9141–9145.
- [25] Angerstein-Kozłowska, H.; Conway, B.; Barnett, B.; Mozota, J. *J. Electroanal. Chem. Interfac. Electrochem.* 1979, 100(1-2), 417 – 446.
- [26] Lai, S. C.; Kleijn, S. E.; Öztürk, F. T.; van Rees Vellinga, V. C.; Koning, J.; Rodriguez, P.; Koper, M. T. *Catal. Today* 2010, 154(1-2), 92 – 104.
- [27] Bard, A. J.; Faulkner, L. R. *Electrochemical Methods: Fundamentals and Applications, 2nd Edition*; Wiley, New York, 2001.
- [28] Kleijn, S. E. F.; Serrano-Bou, B.; Yanson, A. I.; Koper, M. T. M. *Langmuir* 2013, 29(6), 2054–2064.
- [29] Karp, S.; Meites, L. *J. Am. Chem. Soc.* 1962, 84(6), 906–912.
- [30] Zare, H. R.; Nasirizadeh, N. *Electrochim. Acta* 2007, 52(12), 4153 – 4160.
- [31] Raouf, J.; Ojani, R.; Mohammadpour, Z. *Int. J. Electrochem. Sci.* 2010, 5, 177–188.
- [32] Álvarez-Ruiz, B.; Gómez, R.; Orts, J. M.; Feliu, J. M. *J. Electrochem. Soc.* 2002, 149(3), D35–D45.

Appendix A: Fabrication protocol

Chapters 3 and 4 discuss measurements performed on electrodes on microchips, that were specifically designed and fabricated for reproducible measurements of electrochemistry of nanoparticles. The fabrication process is described in detail and additionally design choices, as well as suggestions for future designs, are discussed.

The Fabrication of the on-chip nanoelectrodes was performed in the clean room at the Kavli Institute for Nanotechnology at Delft University of Technology. The process can be separated into two steps: (1) fabrication of Au conductive leads and (2) defining the area of Au nanoelectrodes by selectively etching away a passivation layer that prevents contact between the majority of the patterned Au area and the electrolyte.

Preparation of Au leads

Wafer cleaning

A 10 cm diameter silicon ((100); P-type, 10-30 Ω cm) wafer with a thermally grown oxide layer of 500 nm was purchased at the Van Leeuwenhoek Laboratory in Delft. Prior to processing, the wafer was first sonicated in acetone for 30 seconds and then immersed in fuming HNO_3 for 5 minutes to oxidize any residual contamination on the wafer surface, and rinsed extensively with demineralized water (step 1 on the left-hand side of figure 1).

Application of electron-beam resist

Prior to applying the resist bi-layer for electron beam lithography (EBL) the wafer was baked on a hot plate for 5 minutes, to evaporate water from the wafer surface. After placing the wafer on the spin coater chuck, several milliliters of polymethylglutarimide (PMGI; 7% in cyclopentanone) were spread dropwise on its surface, using a micro-filtered syringe, and it was spun to a thin layer at 2500 RPM and baked on a hot plate at 200 °C for 15 minutes. Immediately afterwards, a second layer of polymethylmethacrylate (PMMA; 950K, 2% in anisole) was spun at 6000 RPM and baked at 175 °C for 15 minutes (step 2).

e-beam exposure and pattern development

Patterns were defined into the resist bi-stack using a Vistec 5000+ electron beam pattern generator (EBPG), operating at 100kV. The pattern was developed in several steps. The PMMA layer was developed by immersing the wafer into a solution of

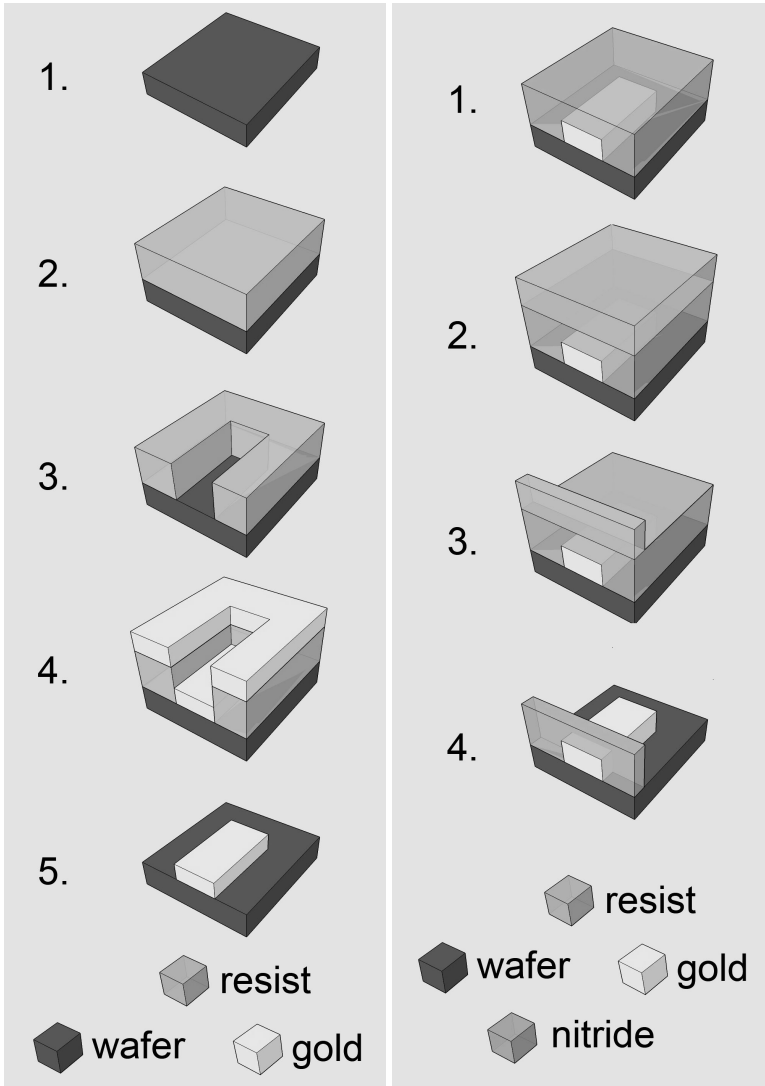


Figure 1: Stepwise formation of Au leads onto the Si wafer (left) and patterning the passivation layer to expose a part of the Au (right)

Methyl isobutyl ketone (MIBK) and isopropanol (IPA), mixed at a volume ratio of 1:3, for 60 seconds, followed by 30 seconds in an IPA bath to stop development. The PMGI layer was developed in Microposit MF-321 (based on Tetramethylammonium hydroxide) for 10 seconds followed by immersion in demineralized water for at least 15 seconds (step 3).

Metal evaporation and lift-off

After inspection of the pattern, the wafer was exposed to an oxygen plasma ($50 \text{ cm}^3 \text{ min}^{-1}$; 100W) for 15 seconds, to remove any residual resist debris ('descumming'). Metal layers were then evaporated onto the wafer at a pressure of 5×10^{-7} mbar using a Temescal FC-2000 electron beam evaporation device. As an adhesion layer, 2 nm of Ti was evaporated at a rate of 1 \AA s^{-1} , followed by 75 nm of Au at 1 \AA s^{-1} (step 4). To lift off the resist-layer, the metallized wafer was immersed in a stirred bath of PRS-3000 (mainly 1-methyl-2-pyrrolidinone) at 85°C for ~ 2 hours (step 5).

Passivation layer

Silicon nitride layer deposition and patterning

To passivate the Au leads, so that only a well-defined area of Au is in contact with the electrolyte, a layer of 400 nm of silicon nitride (Si_3N_4) was deposited using plasma-enhanced chemical vapor deposition (PECVD; Oxford Instruments Plasma Technology Plasmalab 80 Plus; step 1 in on the right-hand side of figure 1). Before a resist layer was spun onto the passivation layer, vinyl tape was applied to prevent resist from covering the macroscopic contact pads, to prevent either a lengthy electron beam patterning step or an additional photolithography step. Afterwards a thick layer of PMMA (950K, 7% in anisole) was spun at 1500 RPM and baked for 15 minutes at 175°C (step 2). Windows were patterned in the resist using e-beam lithography, for which the location was defined using $20 \times 20 \mu\text{m}^2$ markers that were patterned along with the Au leads. The resist was developed in an MIBK and IPA bath (1:3) for 100 seconds, during which ultrasound agitation was applied for 20 seconds, followed by immersion in IPA for at least 30 seconds (step 3).

Dry etching and wafer dicing

The window patterned in the resist layer was transferred into the Si_3N_4 passivation layer by resistive ion etching (RIE; dry etching). Dry etching occurred in a plasma of CHF_3 ($50 \text{ cm}^3 \text{ min}^{-1}$) and O_2 ($2.5 \text{ cm}^3 \text{ min}^{-1}$) at a chamber pressure of 9 μbar and

50W power (step 4). To follow the etching process, the wafer was examined using a Woollam spectroscopic ellipsometer (J.A. Woollam co. inc., M2000XI), at different time intervals, which revealed an etch rate of approximately 40 nm min^{-1} . Before the wafer was diced into 25 microchips, it was cleaned by immersion in fuming HNO_3 and covered with a layer of Shipley S1813 resist (5000 RPM; 15 minutes at 120°C) to prevent excessive Si dust spreading during sawing. After dicing the chip was transferred for measurement to Leiden University.

Discussion

The optimization of lithographically produced devices is a lengthy cycle of prototype preparation, testing and improvement. While the present state of the design is well suited for electrochemical measurements, for lack of time some improvements were not made during the course of the research described in this thesis. Some suggestions are listed here, as well as justifications for several of the fabrication steps from the above.

For the lift-off step, a bi-stack of electron beam resists was applied. Two different resists were used, that both have separate development processes. The bottom, PMGI layer is developed to have a slightly wider pattern than the PMMA on top and is also thicker than the PMMA film. This arrangement prevents the adhesion of metal deposits to the side-walls of the pattern and allows for enhanced solvent access during lift-off. The recipe and the resist stack chosen was the standard protocol provided for lift-off processes by the VLL clean room staff.

The electrodes were patterned in Au because this is the most inert metal that can be conveniently processed in the clean room. Au electrodes are very resistant to chemical cleaning methods, such as immersion in highly oxidative “piranha” mixtures, and can be routinely characterized electrochemically to verify both the cleanliness of the surface and the electrochemically active surface area, as described in chapter 3. The latter is a good verification of a successful fabrication. Au films do not adhere well to the silicon oxide layer on which they are patterned. Typically, an intermediate layer of Cr or Ti is deposited on the SiO_x first, since these metals form strong, chemical bonds with the oxide layer and a metallic interaction with the Au film deposited on top. During measurements of Au nanoelectrodes with Cr as an intermediate layer, parasitic electronic signals were measured that were tentatively attributed to Cr redox chemistry. Upon changing the intermediate layer to Ti, these parasitic signals were lost.

Au electrodes are quite inert, but carbon substrates are known to show even fewer background signals. Particularly for catalytic reactions such as the oxygen reduction

reaction, or the oxidation of hydrazine, carbon electrodes will participate less than Au electrodes. Very interesting measurements using single carbon nanotubes have been demonstrated, although this adds significant additional complexity to fabrication.[1] An alternative, patternable, carbon substrate can be made by pyrolyzing a patterned resist layer after development. This has been demonstrated to reproducibly yield carbon microband electrodes.[2]

The passivation layer is made out of silicon nitride. Initially, vapour deposited silicon oxide films were attempted, but these showed signs of electrolyte leakage to the Au leads. While no further investigation was performed, it was assumed that such SiO_x films are mesoscopically porous and therefore transparent to aqueous solutions.

As described in chapter 3, significant efforts were undertaken to suppress parasitic capacitance from the silicon underneath the SiO_x layer. This capacitance could be prevented by patterning the Au leads on an insulator, for instance by using a glass wafer, as was demonstrated by Ferrari et al..[3] It should be noted that glass wafers charge up during electron beam patterning, significantly reducing the resolution of the process.

The flow cell environment used in the measurements described in chapters 3 and 4 has poor atmospheric control. Therefore, the electrochemical measurements are hindered by the presence of oxygen gas. Significant improvements of atmospheric control have been shown through the construction of specialized measurements cells,[4] and similar setups will be beneficial for future measurements on the microchips described in this thesis.

Bibliography

- [1] Heller, I.; Kong, J.; Heering, H. A.; Williams, K. A.; Lemay, S. G.; Dekker, C. *Nano Letters* 2005, 5(1), 137–142.
- [2] Dumitrescu, I.; Yancey, D. F.; Crooks, R. M. *Lab Chip* 2012, 12(5), 986–993.
- [3] Carminati, M.; Vergani, M.; Ferrari, G.; Caranzi, L.; Caironi, M.; Sampietro, M. *Sens. Actuators, B* 2012, 174(0), 168 – 175.
- [4] Hoeben, F. J. M.; Meijer, F. S.; Dekker, C.; Albracht, S. P. J.; Heering, H. A.; Lemay, S. G. *ACS Nano* 2008, 2(12), 2497–2504.

Appendix B:

Additional experiments for chapter 4

Overview of the Faraday Cage and flow-cell

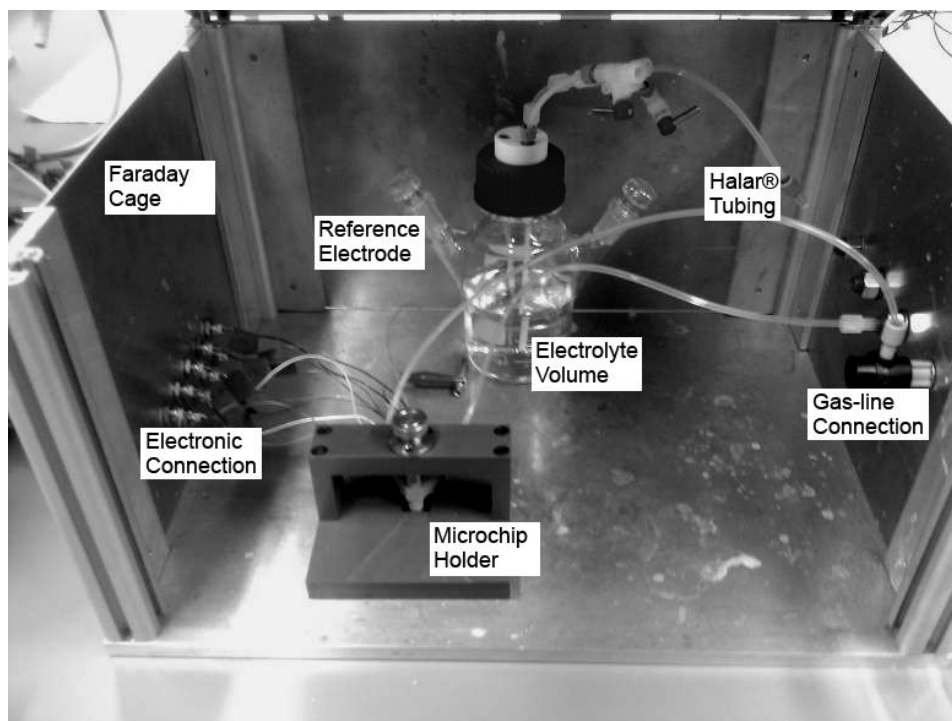


Figure 1: A photograph of the Faraday Cage used throughout the experiments described in chapters 3 and 4. Halar tubing is used to transport electrolyte from the source volume, via the microchip, to the drain volume (consisting of a glass cell not depicted here to maintain clarity). Commercial reference electrodes are inserted in the source volume through the NS15 ground joint.

Landing Pt NPs on a commercial UME

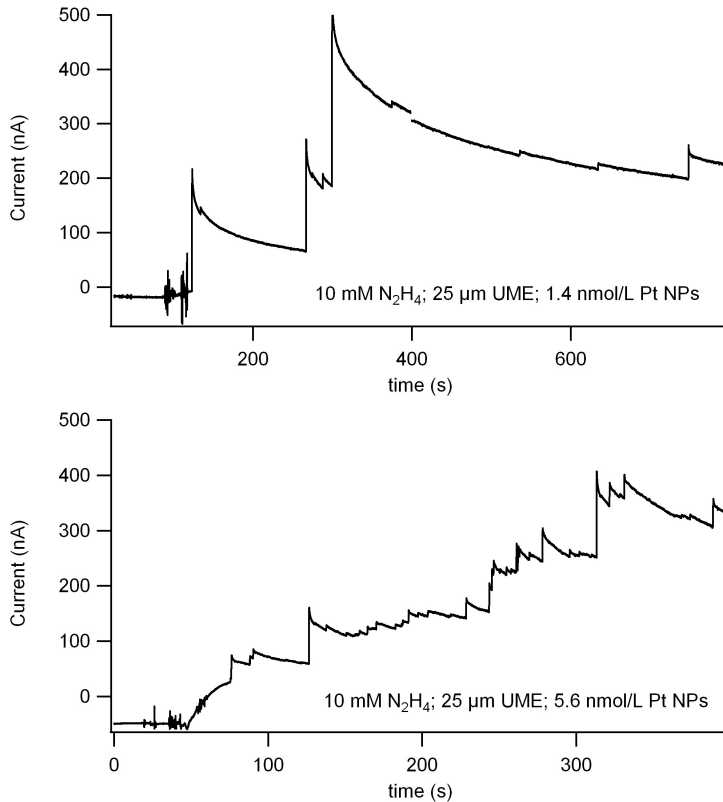


Figure 2: Pt NPs impacting on a 25 μm Au UME in a glass cell containing 100 mL of 10 mM pH 8 phosphate buffer, for two different Pt NP concentrations.

The use of hydrogen as electrocatalytic substrate

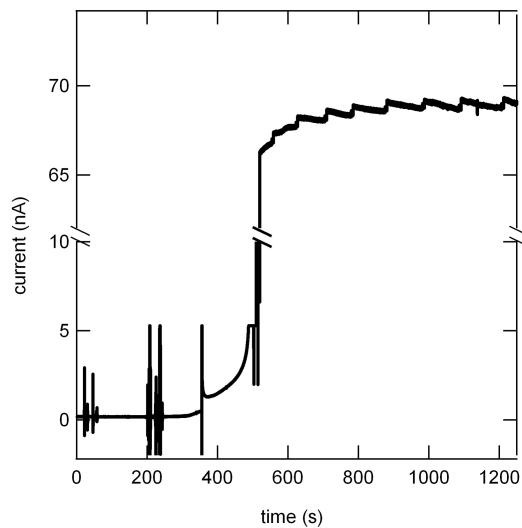
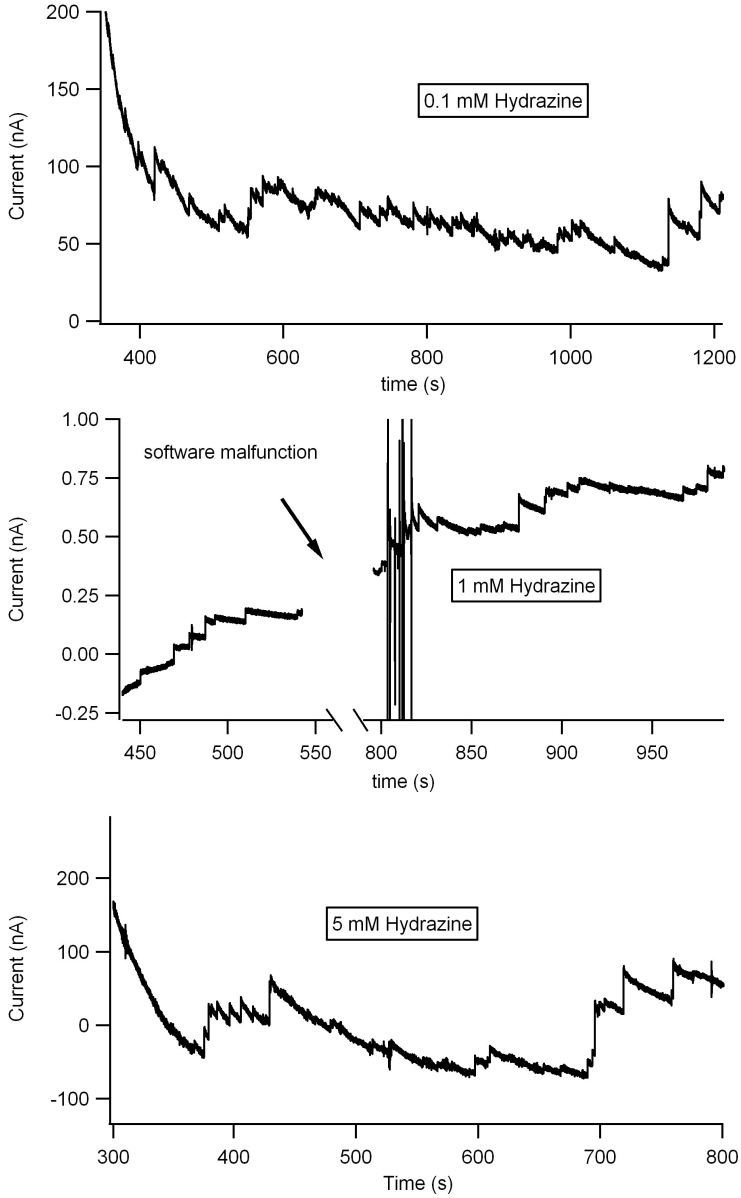
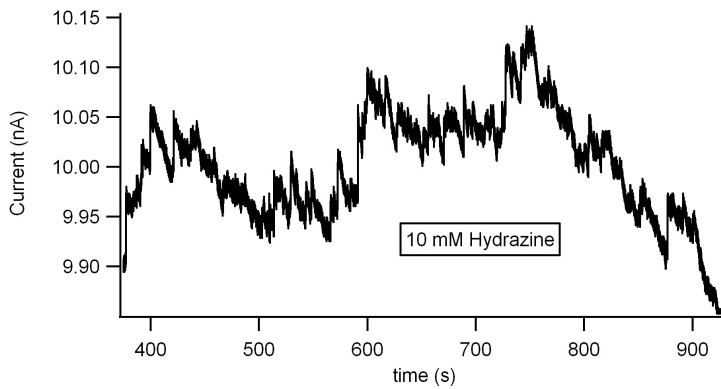
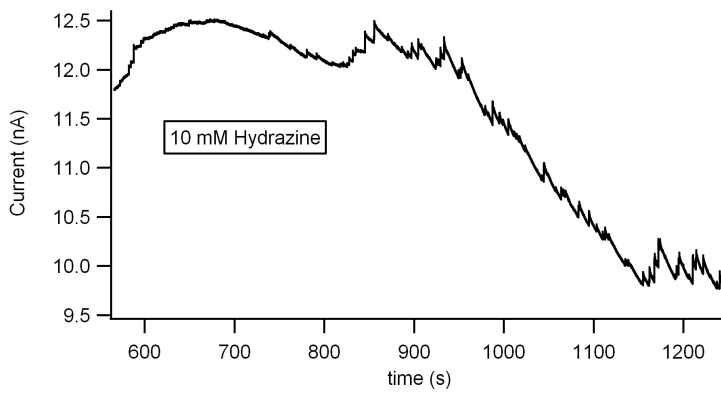
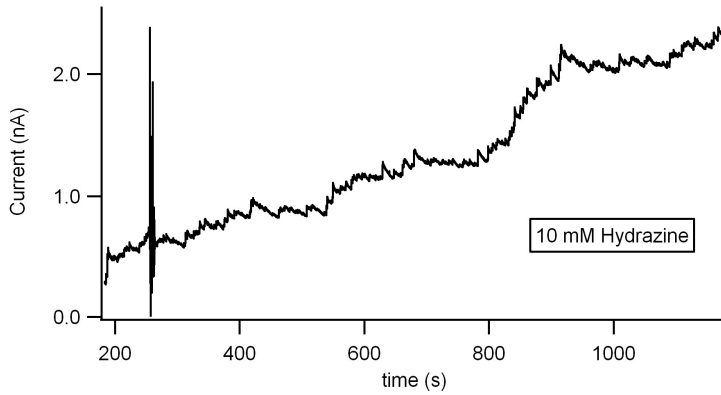


Figure 3: NP detection using $\text{H}_2(\text{g})$ as the electrocatalytic substrate, in 10 mM phosphate buffer at pH 8, with an applied potential of 0.5V.

The influence of the hydrazine concentration





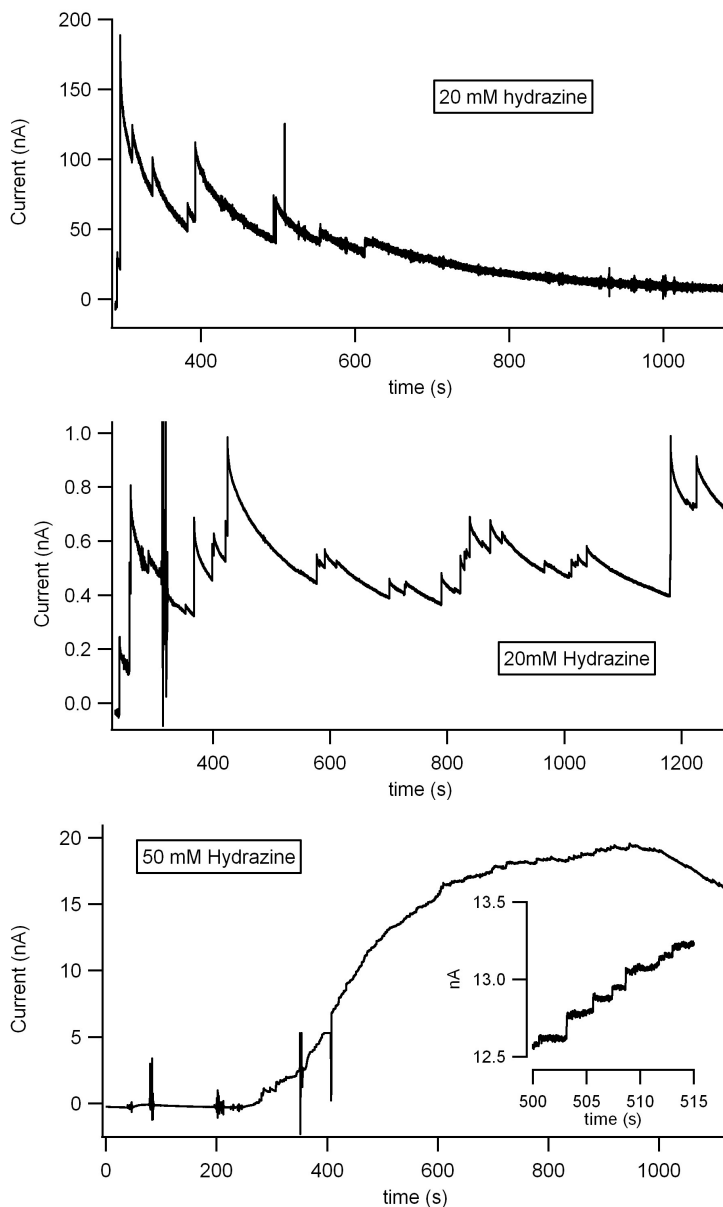


Figure 4: Chronoamperometric measurements of Pt NP impacts on lithographically patterned Au UMEs, using ascending concentrations of hydrazine. The order of data presentation maintains that of table 1 in chapter 4.

Summary

In this thesis catalysis at the nanometer scale is discussed. A catalyst is a substance that can enhance the speed of a chemical reaction, without being consumed in the process. While catalysts can be enzymes or acids, in this thesis only solid metal catalysts are discussed. It has been found that catalysts have a temporary, chemical, interaction with the reactants, and this chemical interaction is highly sensitive to the local shape of the catalyst and the atomic arrangement at the catalyst surface.

Metal catalysts are widely applied in industry, since they greatly increase the rate of chemical reactions in for instance the formation of gasoline from crude oil, or the production of plastics. Additionally, catalytic converters employ metals to reduce emissions from exhausts and are a standard fixture in contemporary automobiles. The metals in catalytic converters catalyse oxidation reactions, completing the combustion of carbon monoxide for instance. Such catalytic combustion can also be used to convert fuels to energy, in *fuel cells*, which have regained interest for application in remote electricity production, to power for instance cars or laptops. Nevertheless, the metals that show the highest efficiency for these reactions are noble metals such as platinum, which are rare and costly, and therefore these catalysts require research to maximize the per weight efficiency. The first step in reducing the mass of platinum required to power a car, is to maximize the surface area, which is done by dispersing the metal into ultrasmall nanoparticles. These characteristics of these nanoparticles have an impact on the catalytic activity, since, as described above, the arrangement of the surface atoms will depend on their size and shape.

The impact on catalytic activity of the size and shape of nanoparticles has been studied by analyzing dispersions of varying mean size. There can still appear size effects that remain hidden in the statistics of the size distribution, if the catalytic activity of a certain particle size or shape is dominant. Therefore it is interesting to attempt the study of individual nanoparticles.

Measuring a single nanoparticle is complicated by two major challenges: first the nanoparticle (with a diameter below 100nm, and more commonly in application, below 10nm) must be isolated in space and second the catalytic activity of the single particle must be accurately determined. The latter challenge can be met for a specific category of catalysis, namely electrocatalysis, which is the field of catalysis concerned with catalytic reactions that involve charge transfer at the interface between a solid catalyst and an electrolyte. The charge transfer as a result of a catalytic reactions can be measured as an electrical current, which is directly equivalent to the catalytic activity. Contemporary electronic amplifiers can amplify signals down to the femtoampère

range, which translates to tenths of thousands of electrons per second.

As discussed in chapter two, several techniques have emerged that combine ultrasensitive electronic measurement with nanometer scale resolution, to measure the chemical reactions at single catalyst nanoparticles. In this chapter various methods of nanoparticle manufacture are discussed, as well as classical methods of measuring the electrocatalytic activity of nanoparticles. Additionally, the current state-of-the-art of measurements on individual catalyst nanoparticles is detailed, with attention to the various methods of nanoparticle isolation.

Two of such methods have been used in the research described in this thesis and the distinguishing quality between them is the nature of the immobilization of the nanoparticles. One way to monitor the signal from a single particle is to create a very tiny 'landing platform' of an electrode, which has as its only function to conduct electrons to or from the catalyst particle, without generating a large signal of its own. Alternatively, the entire measurement system can be made on a scale approaching that of the NP. In electrochemical measurements, the size of the system is dictated by the charge conducting (often liquid) electrolyte. By confining the electrolyte to a droplet of nanoscopic dimensions, electrocatalysis on a very small area can be measured.

In chapter 3 the fabrication of nanoelectrodes small enough to measure single catalyst nanoparticles is presented. This fabrication occurs via the same techniques that are used to prepare transistors on computer processor chips, namely lithography. Using the extremely small tip of an electron beam, it is possible to etch out a nanoscale structure, facilitating the production of ultrasmall electrodes with surface area below a square micrometer. The geometrical surface area of the electrodes is verified using electron microscopy and by electrochemistry through the diffusion limited current of reversible redox couples.

These nanoelectrodes have been used to test the suitability of a specific manner of nanoparticle immobilization, which is the discrete detection of individual nanoparticles onto electrode surfaces. The detection method relies on the enhanced catalytic activity of the nanoparticles with respect to that of the electrode. As nanoparticles randomly move around a liquid electrolyte, that contains a fuel, they will start to oxidize that fuel upon contact with the electrode, which event appears as an electrical current. While it was found possible to detect the arrival of nanoparticles in such a way, through microscopic analysis it was found that the nanoparticles were aggregated into strings of particles. The source of aggregation was found to be the very fuel necessary for the detection of the particles. Therefore, this particular method is currently not suited for the immobilization of individual catalyst particles.

The alternative method used was the landing of particles onto a small electrode area inside an ultras-small electrolyte droplet, as mentioned above. The droplet exists at the end of a capillary, which is tapered to the miniscule diameter of a single micrometer. As the capillary is filled with an electrolyte, the droplet spontaneously forms at the end, the capillary forces being so large that the electrolyte cannot trickle out. The electrolyte contains a nanoparticles and a fuel in solution and the droplet is brought into contact with an inert electrode surface; as the nanoparticles contact that surface, their arrival is detected electronically. When a landing is detected the droplet is removed from the surface and a microscopical analysis of the surface is performed. In this way it was possible to correlate the amount of fuel combustion of a single particle to its size, and to measure the current-voltage diagram of a single NP for the first time.

These delicate measurements give an insight into the nature of analyzing individual catalyst nanoparticles and clearly show that it is feasible to determine their catalytic activity. Future measurements should reveal accurately the dependence of electrocatalysis on shape and size.

Samenvatting

Dit proefschrift gaat over katalyse op de nanoschaal. In aanwezigheid van een katalysator wordt een chemische reactie versneld, zonder dat de katalysator daarbij opgebruikt wordt. Katalysatoren komen in verschillende vormen voor, bijvoorbeeld als enzymen of zuren, maar in dit proefschrift worden alleen katalytische reacties aan metalen behandeld. Het is bekend dat katalysatoren een intermediaire, chemische interactie met de reactanten hebben, waardoor het eindproduct sneller wordt gevormd. Deze interactie is zeer gevoelig voor de vorm van de katalysator op de nanoschaal, dat wil zeggen zowel de rangschikking van de metaal-atomen aan het oppervlak als de lokale structuur van het metaal; deze worden beiden sterk beïnvloed door de grootte van de katalysatordeeltjes. In dit proefschrift wordt onderzoek beschreven, met als doel het toetsen van analytische methodes die de relatie tussen katalytische activiteit en nanodeeltjesgrootte kunnen bepalen.

Metallische katalysatoren vinden brede toepassing in de industrie aangezien zij de snelheid van de chemische reacties in bijvoorbeeld het vormen van benzine uit aardolie, of de productie van plastic, aanzienlijk verhogen. Bovendien is in de uitlaat van elke moderne auto een katalysator gemonteerd, waarin aan metaaldeeltjes de schadelijke rookgassen worden omgevormd. Deze metaaldeeltjes in de uitlaat katalyseren verbrandingsreacties, wanneer ze bijvoorbeeld koolmonoxide omzetten. Een dergelijke verbrandingsreactie kan ook gebruikt worden om een brandstof om te zetten in energie, in zogenaamde *brandstofcellen*, die onlangs hernieuwde aandacht hebben gekregen voor mobiele energietoepassingen, zoals in auto's of laptops. De metalen die in deze toepassing echter de beste prestaties leveren, zijn edelmetalen zoals platina, die zeldzaam en kostbaar zijn. Daarom wordt er onderzoek verricht om de prestaties per gram katalysator zo hoog mogelijk te maken. De eerste stap om het gewicht aan platina dat benodigd is om een auto aan te drijven te verminderen, is het maximaliseren van het metaaloppervlak. Dit gebeurt door het metaal als ultrakleine nanodeeltjes te gebruiken. De eigenschappen van deze nanodeeltjes hebben een sterke invloed op de katalytische activiteit, aangezien de rangschikking van de metaal-atomen aan het oppervlak afhankelijk is van de vorm en de grootte van elk nanodeeltje.

De invloed op de katalytische activiteit van de grootte en de vorm van nanodeeltjes wordt bestudeerd aan de hand van grote groepen deeltjes met verschillende gemiddelde groottes. Het kan echter zo zijn dat er een grootte-afhankelijkheid verborgen blijft in de statistiek van de deeltjesgrootte-verdeling als de katalytische activiteit van een bepaalde deeltjesgrootte of -vorm dominant is. Het is daarom interessant te pogen de

katalytische activiteit van individuele deeltjes te bepalen.

Het meten van de katalytische activiteit van een enkel nanodeeltje is door twee hoofdzaken ingewikkeld: allereerst moet het deeltje (met een diameter van minder dan 100 nanometer, en in de industriële praktijk minder dan 10 nm) op een plaats geïmmobiliseerd worden en ten tweede moet de katalytische activiteit van een enkel deeltje kunnen worden gedetecteerd. Katalytische activiteit kan met zeer hoge nauwkeurigheid worden bepaald voor elektrokatalytische reacties, oftewel katalytische reacties waarin ladingsoverdracht plaatsvindt aan het grensvlak tussen een vaste katalysator en een elektrolyt. Deze ladingsoverdracht wordt gemeten als een elektrische stroom, die direct equivalent is aan de katalytische activiteit. Hedendaagse stroomversterkers kunnen signalen tot femtoampères detecteren, wat neer komt op de detectie van tienduizenden elektronen per seconde.

In de recente wetenschappelijke literatuur zijn verschillende technieken beschreven die gevoelige elektronische meetapparatuur combineren met precisie op de nanometerschaal, waarmee chemische reacties aan enkele katalysatordeeltjes kunnen worden gemeten. In het tweede hoofdstuk van dit proefschrift worden verschillende methodes voor het fabriceren van nanodeeltjes belicht, naast klassieke methodes voor het meten van hun elektrokatalytische activiteit. Bovendien wordt de huidige stand van de techniek van het meten van enkele katalysatordeeltjes behandeld, met aandacht voor verscheidene manieren van het immobiliseren van nanodeeltjes.

Twee van deze methodes zijn gebruikt in het onderzoek dat in het proefschrift wordt beschreven, waarbij de onderscheidende factor bestaat uit de wijze waarop de deeltjes geïsoleerd worden. Één manier om enkele deeltjes te meten is het fabriceren van een ontzettend klein 'landingsplatform' als elektrode die uitsluitend dient om de elektronen te geleiden die van of naar het nanodeeltje stromen als gevolg van een elektrokatalytische reactie, zonder daarbij zelf een signaal te genereren. De andere methode bestaat uit het samenstellen van een meetsysteem dat een vergelijkbare grootte heeft van het nanodeeltje. Bij elektrochemische metingen wordt de grootte van het systeem vaak bepaald door het ladingsgeleidende elektrolyt. Door het elektrolyt tot een klein druppeltje met nanodimensies te verkleinen, kan elektrokatalyse op een extreem klein oppervlak worden gemeten.

Het maken van nanoelektrodes die klein genoeg zijn om een enkel deeltje op te landen wordt uitgelegd in hoofdstuk 3. De fabricage geschiedt volgens eenzelfde procédé dat gebruikt wordt voor het maken van transistoren voor computerchips, namelijk lithografie. Met de extreem kleine stip van een elektronenbundel is het mogelijk om een nanostructuur te etsen, waardoor de productie van elektrodes met een oppervlak

van minder dan een vierkante micrometer mogelijk wordt. De grootte van het oppervlak kan worden geverifieerd met zowel elektronenmicroscopie als elektrochemische redox reacties.

Deze nanoelektrodes zijn gebruikt om een bepaalde manier van nanodeeltjes-immobilisatie te testen, namelijk het detecteren van het landen van individuele nanodeeltjes. Deze detectiemethode berust op de specifieke katalytische activiteit van de nanodeeltjes die veel groter is dan die van de elektrode. Wanneer nanodeeltjes willekeurig door een brandstof-bevattend elektrolyt bewegen, zullen ze die brandstof verbranden op het moment dat ze contact maken met de elektrode, wat een meetbare verhoging van de stroom oplevert. Hoewel het bevestigd kon worden dat deze methode geschikt is om discrete deeltjeslandingen te detecteren, werd door microscopie-analyse aangetoond dat de deeltjes tot ketens aggregeren. Deze aggregatie wordt veroorzaakt door de brandstof die vereist is om de detectie te faciliteren. Daarom is deze methode op dit moment niet geschikt bevonden voor de immobilisatie van individuele deeltjes.

Als alternatief zijn nanodeeltjes geland op een klein elektrode oppervlak binnenin een ultrakleine nanodruppel. Deze druppel van elektrolyt vormt zich aan het einde van een glazen capillairtje, dat uitloopt in een punt met een doorsnede van een micrometer. De capillaire krachten aan het eind van het capillairtje zijn dusdanig groot, dat de vloeistof niet weglekt. In de druppel is een brandstof opgelost, en er zijn metalen nanodeeltjes aan toegevoegd, die willekeurig rond-diffunderen. Wanneer de druppel in contact gebracht wordt met een geleidend elektrodeoppervlak, kan daaraan de landing van een enkel deeltje elektronisch gemeten worden. Hierna wordt de druppel van het oppervlak afgetild en kan middels elektronenmicroscopie het gelande deeltje worden geanalyseerd. Op deze manier was het mogelijk een correlatie te maken tussen de hoeveelheid verbrande brandstof en de grootte van een deeltje, en kon voor het eerst een stroom-spanningsdiagram van een enkel deeltje gemeten worden.

Deze delicate metingen zijn een eerste stap in het analyseren van individuele katalysatordeeltjes en tonen duidelijk aan dat het mogelijk is om hun katalytische activiteit te bepalen. Toekomstige metingen zullen op accurate wijze de relatie tussen deeltjes-grootte en -vorm en elektrokatalytische activiteit aantonen.

List of publications

This thesis is based on the following publications:

Chapter 2

S.E.F. Kleijn, S.C.S. Lai, M.T.M. Koper and P.R. Unwin

Electrochemistry of nanoparticles

Angewandte Chemie, *Accepted*

Chapter 3

S.E.F. Kleijn, A.I. Yanson and M.T.M. Koper

Electrochemical characterization of nano-sized gold electrodes fabricated by nanolithography

Journal of Electroanalytical Chemistry, 2012, **666**, 19 - 24

Chapter 4

S.E.F. Kleijn, B. Serrano-Bou, A.I. Yanson and M.T.M. Koper

Influence of Hydrazine-Induced Aggregation on the Electrochemical Detection of Platinum Nanoparticles

Langmuir, 2013, **29**, 2054-2064

Chapter 5

S.E.F. Kleijn, S.C.S. Lai, T.S. Miller, A.I. Yanson, M.T.M. Koper and P.R. Unwin

Landing and Catalytic Characterization of Individual Nanoparticles on Electrode Surfaces

Journal of the American Chemical Society, 2012, **134**, 18558-18561

Other publications:

Y. Kwon, S. E. F. Kleijn, K. J. P. Schouten and M. T. M. Koper

Cellobiose hydrolysis and decomposition by electrochemical generation of acid and hydroxyl radicals

ChemSusChem, 2012, **5**, 1935 - 1943

V. Aquilanti, K.C. Mundim, M. Elango, S. Kleijn and T. Kasai

Temperature dependence of chemical and biophysical rate processes: Phenomenological approach to deviations from Arrhenius law

Chemical Physics Letters, 2010, **498**, 209 - 213

S.C.S. Lai, S.E.F. Kleijn, F.T.Z. Öztürk, V.C. van Rees Vellinga, J. Koning, P. Rodriguez and M.T.M. Koper

Effects of electrolyte pH and composition on the ethanol electro-oxidation reaction

Catalysis Today, 2010, **154**, 92 - 104

M. Nishiyama, S. Kleijn, V. Aquilanti and T. Kasai

Temperature dependence of respiration rates of leaves, ¹⁸O-experiments and super-Arrhenius kinetics

Chemical Physics Letters, 2009, **482**, 325 - 329

M. Nishiyama, S. Kleijn, V. Aquilanti and T. Kasai

Mass spectrometric study of the kinetics of O₂ consumption and CO₂ production by breathing leaves

Chemical Physics Letters, 2009, **470**, 332 - 336

S.C.S. Lai, S.E.F. Kleyn, V. Rosca and M.T.M. Koper

Mechanism of the Dissociation and Electrooxidation of Ethanol and Acetaldehyde on Platinum As Studied by SERS

Journal of Physical Chemistry C, 2008, **112**, 19080-19087

F Gou, M.A Gleeson, J Villette, S.E.F Kleyn and A.W Kleyn

The surface of 1-euro coins studied by X-ray photoelectron spectroscopy

Applied Surface Science, 2004, **225**, 47 - 53

Curriculum Vitae

Steven Everard Filippus Kleijn was born in Amsterdam, march 8th 1985, before attending the “Barlaeus gymnasium” there and subsequently studying Japanese language at the Kyoto Japanese Language School.

In 2004 he joined the Bachelor of Science program named Molecular Science and Technology between Leiden and Delft Technical University, as part of which he researched the application of commercial pigments as potential photocatalysts for the water-splitting reaction, in the research group of prof. Dr. Roel van de Krol. He also was part of a delegation of chemical engineering students visiting China for three weeks during the summer of 2007. He obtained a Master of Science degree at Leiden University in the Physical and Theoretical Chemistry course, with a thesis entitled “*carbon-carbon bond breaking in ethanol – A spectroscopic and voltammetric study on electrochemical ethanol oxidation*”, under the supervision of Dr. Stanley C.S. Lai and prof. Dr. Marc T.M. Koper. During this period he spent three months at Osaka University in the research group of prof. Dr. Toshio Kasai, to study the respiration rates of Camellia leaves using mass spectrometry. This work has lead to several publications in collaboration with prof. Dr. Vincenzo Aquilanti at Perugia University, in Italy.

The research described in this thesis was carried out principally at Leiden University in the research group of prof. Koper, with significant contributions made at the University of Warwick, in the UK, under the supervision of Dr. Stanley Lai and prof. Dr. Patrick R. Unwin.

In the fall of 2013, Steven has taken up a position at SMART Photonics in Eindhoven, where he will work as a research associate on the fabrication of indium phosphide-based integrated photonics.